Dissertation submitted to the

Combined Faculties for the Natural Sciences and for Mathematics
of the Ruperto-Carola University of Heidelberg, Germany

for the degree of Doctor of Natural Sciences

Put forward by

**Dipl.-Phys. Manuel F. Juette**

born in Siegen, Germany

Oral examination: December 6, 2012

# 3D Submillisecond Tracking Microscopy of Single Fluorescent Particles with Adaptive Optics

Manuel F. Juette

Referees:
Prof. Dr. Joachim Spatz
Prof. Dr. Joerg Bewersdorf

# Abstract

*3D Submillisecond tracking microscopy of single fluorescent particles with adaptive optics.*—Single particle tracking microscopy in combination with fluorescent labeling has opened the door to investigations of nanoscale dynamics in living cells. While conventional instruments feature temporal resolutions of typically 5–30 ms, nanoscale processes happen on a millisecond or submillisecond time scale.

To overcome this limitation, I have developed a single particle tracking microscope with 130 µs temporal resolution and single-fluorophore sensitivity. The instrument acquires 3D trajectories by active tracking of a fluorescent particle with a focused laser beam. This is accomplished by fast beam steering, which is feedback-driven by the detected particle position in the focal volume. For translation of the laser focus along the optical axis, I have implemented a novel vibration-free remote focusing mechanism based on a deformable mirror, an adaptive optics wavefront correction device.

In characterization experiments with fluorescent beads, I have found that the instrument is capable of tracking directed motion up to 150 µm/s and free 3D Brownian motion with diffusion coefficients of more than 2 $\mu m^2/s$. The potential for biological applications is demonstrated by tracking fluorescently labeled viruses on cell membranes and transport vesicles in the cytoplasm of living cells.

## Zusammenfassung

*Mikroskopische Submillisekunden-Messung der 3D Trajektorien einzelner fluoreszierender Objekte mit adaptiver Optik.*—Mit Fluoreszenzmikroskopie kann die Bewegung teilchenartiger Komponenten in lebenden Zellen verfolgt werden. Solche “Single Particle Tracking”-Experimente beleuchten Längenskalen auf der Nanometerskala, haben aber häufig keinen Zugang zu den kürzesten involvierten Zeitskalen. Diese bewgen sich im Bereich von Millisekunden oder sogar darunter, während konventionelle Instrumente Zeitauflösungen von typischerweise 5–30 ms erzielen.

Das Mikroskop, das ich im Rahmen dieser Arbeit entwickelt habe, ermöglicht dreidimensionales Single Particle Tracking mit 130 µs Zeitauflösung und ist empfindlich genug für die Detektion einzelner Fluorophore. Dazu wird ein Laserfokus in Echtzeit dem beobachteten Objekt nachgeführt. Die Fokusposition wird durch ein Feedback-Signal gesteuert, das proportional zur Entfernung des Objekts vom Fokusmittelpunkt ist. Um den Laserfokus entlang der optischen Achse zu bewegen, verwende ich einen verformbaren Spiegel aus der adaptiven Optik. Diese neue Methode erlaubt ein schnelles und vibrationsfreies Einstellen der Fokustiefe.

Das Mikroskop verfolgt gerichtete Bewegungen bis zu 150 µm/s und Brownsche Bewegung in 3D mit Diffusionskonstanten über 2 µm$^{2}$/s. Diese Eigenschaften zeige ich in Experimenten mit fluoreszierenden Mikrokügelchen. Das Instrument eignet sich auch für die Untersuchung lebender Zellen: ich beschreibe Experimente, in denen Viren auf der Zellmembran und Transportvesikel im Cytoplasma verfolgt werden.

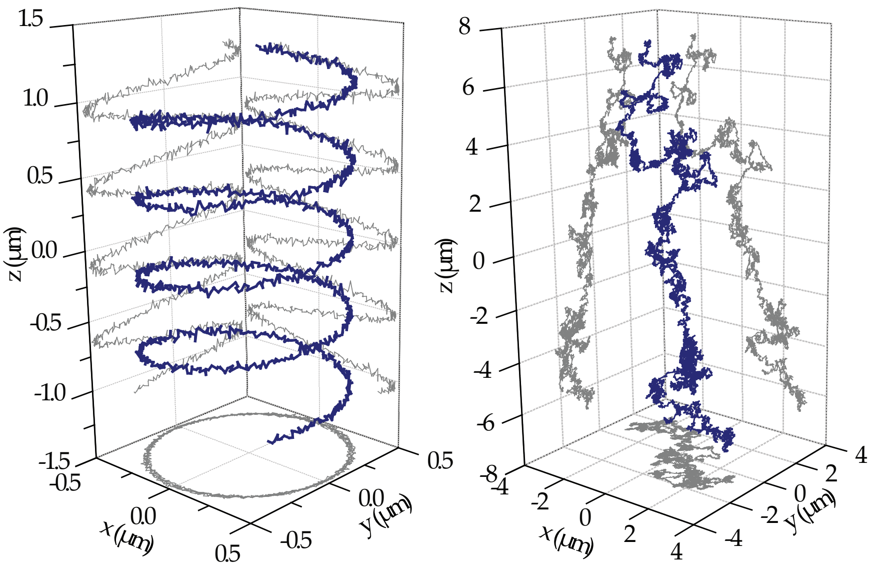

Three-dimensional particle tracking of a 200 nm fluorescent bead undergoing artificial directed motion on a piezo stage (left) and free diffusion in water (right) at 2 ms and 300 µs temporal resolution, respectively. Adapted from Juette and Bewersdorf (2010).

All research presented here was performed at:

Yale University
Department of Cell Biology
New Haven, Connecticut (USA)

Other publications by Manuel Juette:

M. F. Juette, F. E. Rivera-Molina, D. K. Toomre, and J. Bewersdorf (2012). "3D single particle tracking with adaptive optics reveals cellular millisecond dynamics." (in preparation)

E. B. Kromann, T. J. Gould, M. F. Juette, J. E. Wilhjelm, and J. Bewersdorf (June 2012). "Quantitative pupil analysis in stimulated emission depletion microscopy using phase retrieval." *Optics Letters* **37** (11), pp. 1805–1807. DOI: `10.1364/OL.37.001805`

M. F. Juette and J. Bewersdorf (Oct. 2010). "Three-Dimensional Tracking of Single Fluorescent Particles with Submillisecond Temporal Resolution." *Nano Lett.* **10** (11), pp. 4657–4663. DOI: `10.1021/nl1028792`

M. F. Juette, T. J. Gould, and J. Bewersdorf (July 2010). "Superresolution Far-Field Fluorescence Microscopy." *Nanobiophotonics*. 1st ed. McGraw-Hill, pp. 369–402

M. J. Mlodzianoski, M. F. Juette, G. L. Beane, and J. Bewersdorf (May 2009). "Experimental characterization of 3D localization techniques for particle-tracking and super-resolution microscopy." *Optics Express* **17** (10), pp. 8264–8277. DOI: `10.1364/OE.17.008264`

M. F. Juette (Apr. 2009). *3D Fluorescence Photoactivation Localization Microscopy and Particle Tracking with Biplane Detection*. University of Heidelberg: Diplom thesis in physics

M. F. Juette, T. J. Gould, M. D. Lessard, M. J. Mlodzianoski, B. S. Nagpure, B. T. Bennett, S. T. Hess, and J. Bewersdorf (May 2008). "Three-dimensional sub–100 nm resolution fluorescence microscopy of thick samples." *Nature Methods* **5** (6), pp. 527–529. DOI: `10.1038/nmeth.1211`

This dissertation was supported by a graduate student fellowship from the German Academic Exchange Service (DAAD Doktorandenstipendium).

# Contents

**Abstract** v

**Publication List** xi

**Contents** xiii

**List of Figures** xvi

**List of Abbreviations** xviii

**1 Introduction** 1
  1.1 Dynamics at the Nanoscale . . . . . . . . . . . . . . . . . . . . . . . . . 2
  1.2 Thesis Outline . . . . . . . . . . . . . . . . . . . . . . . . . . . . . . . 4

**2 Fundamentals of Single Particle Tracking** 7
  2.1 Single Particle Localization . . . . . . . . . . . . . . . . . . . . . . . . 7
    2.1.1 Image Formation in Fluorescence Microscopy . . . . . . . . . . 8
    2.1.2 Localization in Two Dimensions . . . . . . . . . . . . . . . . . . 10
    2.1.3 Localization in Three Dimensions . . . . . . . . . . . . . . . . . 11
      Related Work: Comparison of 3D Localization with Biplane and Astigmatic Detection . . . . . . . . . . . . . . . . . . . . . 13
    2.1.4 Pointillism Microscopy . . . . . . . . . . . . . . . . . . . . . . . 15
      Related Work: Biplane Fluorescence Photoactivation Localization Microscopy . . . . . . . . . . . . . . . . . . . . . . 15
  2.2 Survey of 3D Single Particle Tracking Methods . . . . . . . . . . . . . 17
    2.2.1 Analysis of Widefield Image Sequences . . . . . . . . . . . . . . 18
    2.2.2 Live Feedback . . . . . . . . . . . . . . . . . . . . . . . . . . . . 18
  2.3 Trajectory Analysis . . . . . . . . . . . . . . . . . . . . . . . . . . . . 20

**3 Elements of Adaptive Optics 23**
3.1 Aberration Theory in the Scalar Approximation . . . . . . . . . . . . . 23
3.2 Wavefront Sensing . . . . . . . . . . . . . . . . . . . . . . . . . . . . . . 26
3.3 Wavefront Shaping . . . . . . . . . . . . . . . . . . . . . . . . . . . . . 26
3.4 Defocus with a Lens Satisfying the Sine Condition . . . . . . . . . . . . 28
3.5 Phase Retrieval . . . . . . . . . . . . . . . . . . . . . . . . . . . . . . . 28
Related Work: Phase Retrieval in Stimulated Emission Depletion Microscopy . . . . . . . . . . . . . . . . . . . . . . . . . . . 29

**4 Setup and Methods 31**
4.1 Optical Setup . . . . . . . . . . . . . . . . . . . . . . . . . . . . . . . . 31
4.2 Beam Steering . . . . . . . . . . . . . . . . . . . . . . . . . . . . . . . . 35
4.2.1 Performance of Piezo Positioners . . . . . . . . . . . . . . . . . 36
4.2.2 Integration of a Micromachined Membrane Deformable Mirror 36
4.3 Read Out of the Fluorescence Signal . . . . . . . . . . . . . . . . . . . . 38
4.4 Position Estimation . . . . . . . . . . . . . . . . . . . . . . . . . . . . . 39
4.5 Feedback Operation . . . . . . . . . . . . . . . . . . . . . . . . . . . . . 40

**5 Experiments and Results 45**
5.1 Instrument Calibration . . . . . . . . . . . . . . . . . . . . . . . . . . . 45
5.1.1 Deformable Mirror Optimization . . . . . . . . . . . . . . . . . . 45
Zernike Mode Optimization . . . . . . . . . . . . . . . . . . . . 45
Correction for Spherical Aberrations . . . . . . . . . . . . . . . 46
5.1.2 Beampath Alignment . . . . . . . . . . . . . . . . . . . . . . . . 48
5.1.3 Positioning Calibration . . . . . . . . . . . . . . . . . . . . . . . 49
5.1.4 Photon Count Calibration . . . . . . . . . . . . . . . . . . . . . . 49
5.2 Instrument Characterization . . . . . . . . . . . . . . . . . . . . . . . . 50
5.2.1 Step Response . . . . . . . . . . . . . . . . . . . . . . . . . . . . 50
5.2.2 Localization Precision . . . . . . . . . . . . . . . . . . . . . . . . 53
5.2.3 Programmed Trajectories . . . . . . . . . . . . . . . . . . . . . . 53
5.3 Applications . . . . . . . . . . . . . . . . . . . . . . . . . . . . . . . . . 54
5.3.1 Finding Particles . . . . . . . . . . . . . . . . . . . . . . . . . . . 54
5.3.2 Diffusing Beads . . . . . . . . . . . . . . . . . . . . . . . . . . . 56
5.3.3 Live-Cell Particle Tracking . . . . . . . . . . . . . . . . . . . . . . 58
Viral Motion . . . . . . . . . . . . . . . . . . . . . . . . . . . . . 58
Transport Vesicles . . . . . . . . . . . . . . . . . . . . . . . . . . 59
5.3.4 Single Proteins . . . . . . . . . . . . . . . . . . . . . . . . . . . . 61

**6 Discussion 65**
6.1 Summary of Results . . . . . . . . . . . . . . . . . . . . . . . . . . . . . 65
6.2 Perspectives in Feedback-Driven Single Particle Tracking . . . . . . . . 66

**Appendices** 72

**A Software Package** 72

**B Spectra** 75

**C Sample Preparation** 76

C.1 Bead Samples . . . . . 76

C.2 Generation of Murine Leukemia Virus particles . . . . . 76

C.3 EA.hy926 starvation and Transferrin-Alexa488 uptake . . . . . 77

**D Electronics** 78

**E Air Vibrations** 79

**Back Matter** 81

**Acknowledgments** 82

**Statement of Authorship** 84

**Bibliography** 85

# List of Figures

---

1.1 Orders of magnitude in nanoscale dynamics . . . . . . . . . . . . . . . . . 3

2.1 Point-spread function and optical transfer function . . . . . . . . . . . . . . 9
2.2 Illustration of three methods for axial particle localization . . . . . . . . . 12
2.3 Experimental comparison of 3D localization methods . . . . . . . . . . . . 14
2.4 Principle of pointillism microscopy . . . . . . . . . . . . . . . . . . . . . . . . 16
2.5 Beads and mitochondria imaged with Biplane FPALM . . . . . . . . . . . 17
2.6 Particle tracking with feedback and confocal readout . . . . . . . . . . . . 19
2.7 Mean square displacement for different types of motion . . . . . . . . . . 21

3.1 Zernike polynomials corresponding to classical low-order aberrations . . 25
3.2 Function of a Shack-Hartman wavefront sensor . . . . . . . . . . . . . . . 26
3.3 Wavefront shaping with a deformable mirror . . . . . . . . . . . . . . . . . 27
3.4 Phase retrieval in stimulated emission depletion microscopy . . . . . . . . 30

4.1 Optical setup . . . . . . . . . . . . . . . . . . . . . . . . . . . . . . . . . . . . 32
4.2 Picture of the single particle tracking setup . . . . . . . . . . . . . . . . . . 33
4.3 Step response of piezo positioners . . . . . . . . . . . . . . . . . . . . . . . 37
4.4 Step response of the deformable mirror . . . . . . . . . . . . . . . . . . . . 38
4.5 The reduced Gaussian position estimator . . . . . . . . . . . . . . . . . . . 41
4.6 Input-output latency of the PC workstation . . . . . . . . . . . . . . . . . . 42
4.7 Schematic of feedback operation . . . . . . . . . . . . . . . . . . . . . . . . 43

5.1 Map of normalized Strehl ratio . . . . . . . . . . . . . . . . . . . . . . . . . 47
5.2 “Naive” and optimized point-spread function . . . . . . . . . . . . . . . . 48
5.3 Lateral step response . . . . . . . . . . . . . . . . . . . . . . . . . . . . . . . 51
5.4 Axial step responses with piezo mirror and deformable mirror . . . . . . 52
5.5 Localization precision as a function of detected photons . . . . . . . . . . 54
5.6 Programmed trajectories . . . . . . . . . . . . . . . . . . . . . . . . . . . . . 55
5.7 Bead diffusion . . . . . . . . . . . . . . . . . . . . . . . . . . . . . . . . . . . 57
5.8 Schematic view of a murine leukemia virus . . . . . . . . . . . . . . . . . . 58

5.9 Diffusion of a GFP-labeled murine leukemia virus . . . . . . . . . . . . . . . 59
5.10 Surfing of a murine leukemia virus on a living cell . . . . . . . . . . . . . . 60
5.11 Trajectory of a single vesicle . . . . . . . . . . . . . . . . . . . . . . . . . . . . . 62
5.12 Distribution of vesicle diffusion coefficients and velocities . . . . . . . . . 63
5.13 Photon traces for single-antibody tracking . . . . . . . . . . . . . . . . . . . 64

6.1 Possible implementation of second channel . . . . . . . . . . . . . . . . . . . 67
6.2 Jablonski diagram of a fluorophore . . . . . . . . . . . . . . . . . . . . . . . . 69

A.1 User interface . . . . . . . . . . . . . . . . . . . . . . . . . . . . . . . . . . . . 73
A.2 Code architecture . . . . . . . . . . . . . . . . . . . . . . . . . . . . . . . . . . 74

B.1 Spectra of fluorophores and optical components . . . . . . . . . . . . . . . . 75

D.1 Deformable mirror high voltage amplifier circuit . . . . . . . . . . . . . . . 78

E.1 Air vibration measurement . . . . . . . . . . . . . . . . . . . . . . . . . . . . . 79

# List of Abbreviations

**AOD** acousto-optic deflector

**AOM** acousto-optic modulator

**AOTF** acousto-optic tunable filter

**APD** avalanche photodiode

**BSA** bovine serum albumin

**CCD** charge-coupled device

**CMOS** complementary metal-oxide semiconductor

**CRLB** Cramér-Rao lower bound

**DNA** deoxyribonucleic acid

**EM-CCD** electron-multiplying CCD

**FBS** fetal bovine serum

**FCS** fluorescence correlation spectroscopy

**FPALM** fluorescence photoactivation localization microscopy

**FPGA** field-programmable gate array

**FRET** Förster resonance energy transfer

**FWHM** full width at half-maximum

**GFP** green-fluorescent protein

**GPS** global positioning system

**GPU** graphics processing unit

**MES** 2-(N-morpholino)ethanesulfonic acid

**MLE** maximum-likelihood estimator

**MLV** murine leukemia virus

**MMDM** micro-machined membrane deformable mirror

**MSD** mean square displacement

**NA** numerical aperture

**ND** neutral density

**OTF** optical transfer function

**PALM** photoactivated localization microscopy

**PBS** phosphate-buffered saline

**PMT** photo-multiplier tube

**PSF** point-spread function

**RME** receptor-mediated endocytosis

**RMS** root mean square

**RNA** ribonucleic acid

**ROI** region of interest

**sCMOS** scientific grade CMOS

**SHWS** Shack-Hartmann wavefront sensor

**SLM** spatial light modulator

**SNR** signal-to-noise ratio

**SPT** single particle tracking

**SPTM** single particle tracking microscopy

**SPTM** single particle tracking microscope

**STED** stimulated emission depletion

**STORM** stochastic optical reconstruction microscopy

**TIRF** total internal reflection fluorescence

# 1 Introduction

> This [ant] was a creature, more troublesom to be drawn, then any of the rest, for I could not, for a good while, think of a way to make it suffer its body to ly quiet in a natural posture; (. . . ) I took the creature, I had design'd to delineate, and put it into a drop of very well rectified spirit of Wine, this I found would presently dispatch, as it were, the Animal (. . . )
>
> *"Micrographia. Some Physiological Descriptions of Minute Bodies Made by Magnifying Glasses with Observations and Inquiries Thereupon"*
> Robert Hooke (1665)

Living systems exhibit dynamic processes over many orders of magnitude, from large-scale ecosystems to single molecules. On each level, interactions of large populations of individual "players" determine the function of a system: neurons cooperate to form complex circuits; an organism is an ensemble of many specialized organs and tissues. At the small end of the biological size spectrum, the cellular machinery of life functions due to the physical interactions of a multitude of individual molecules.

Each size range is associated with a characteristic range of time scales. The relevant time scale for biomolecular interactions is milliseconds and below. As emerging scientific tools provide access to previously unexplored spatial domains, it is equally important to enable observation of the corresponding temporal regimes.

Human understanding of fundamental biology is closely linked to the history of the microscope. As the instrument has evolved over the past five centuries (Croft, 2006), it has opened up views of increasingly elementary components of life—revealing, at the same time, deeper layers of hidden complexity. Yet it has always been challenging to study fast-moving dynamics under the microscope.

Robert Hooke often had to observe dead specimens to produce the famous drawings of small insects displayed in his *Micrographia*—the living animals' limbs were moving too fast (Hooke, 1665). The familiar transmission electron micrographs of mitochondria and other cellular organelles, whose iconic shapes inspire the schematic drawings in modern biology textbooks (Alberts et al., 2007), are snapshots of solidly embedded or frozen microtome sections.

In recent years, super-resolution far-field fluorescence microscopy (Hell, 2007; Toomre and Bewersdorf, 2010) has brought imaging of the nanometer regime into the reach of the light microscope. The non-invasive nature of photons in the visible spectrum (compared to e.g. electrons or x-ray photons) allows the observation of subcellular features under comparatively unperturbed live-cell conditions.

However, these nanoscopic technologies are just recently approaching video-rate imaging, i.e. temporal resolutions in the 100-ms range (Jones et al., 2011; Kner et al., 2009; Shim et al., 2012; Westphal et al., 2008). While this has the potential to provide a great amount of information, a simple order-of magnitude calculation illustrates that it is not sufficient to illuminate the full dynamic picture.

## 1.1 Dynamics at the Nanoscale

Consider free three-dimensional diffusion, which is often the rate-limiting process in nanoscale dynamics. The "speed" of a freely diffusing object can be estimated from its mean square displacement (MSD),

$$\langle d^2(\tau) \rangle = 6D\tau. \tag{1.1}$$

Here, $d(\tau)$ is the displacement of the object from the origin after a lag time $\tau$, $\langle \cdot \rangle$ denotes the temporal average (often extended to an ensemble average over several observed trajectories), and

$$D = \frac{k_\mathrm{B} T}{6\pi\eta R_\mathrm{H}} \tag{1.2}$$

is the diffusion coefficient (with $k_\mathrm{B}$ being being the Boltzmann constant, $\eta$ the dynamic viscosity of the medium, and $R_\mathrm{H}$ the hydrodynamic radius of the diffusing object).

In water at the physiological temperature of 37°C ($\eta = 6.93 \times 10^{-4}$ Pa s; Huber et al., 2009), a typical eukaryotic cell of 10 µm diameter might move at a rather leisurely 600 nm per second on average (corresponding to a diffusion coefficient of $D \approx 0.07$ µm$^2$/s). A 200 nm-diameter virus exceeds this by nearly three orders of magnitude, achieving an average displacement of 140 nm per *milli*second ($D \approx$ 3.3 µm$^2$/s). A single green-fluorescent protein (GFP) molecule with an approximate diameter of 3 nm bounces around at over 1 µm per ms ($D \approx 220$ µm$^2$/s). These proportions are illustrated in Figure 1.1a.

Traditional live-cell imaging records the time evolution of a large ensemble of nanoscopic objects; it does not typically allow one to trace the fate of the *individual* objects. However, functional information may be encoded in their motion. Single particle tracking (SPT) addresses this shortcoming of conventional imaging methods by measuring the trajectories of a sufficiently sparse set of "small" objects (Saxton and Jacobson, 1997). The above-mentioned examples give an intuitive idea of the

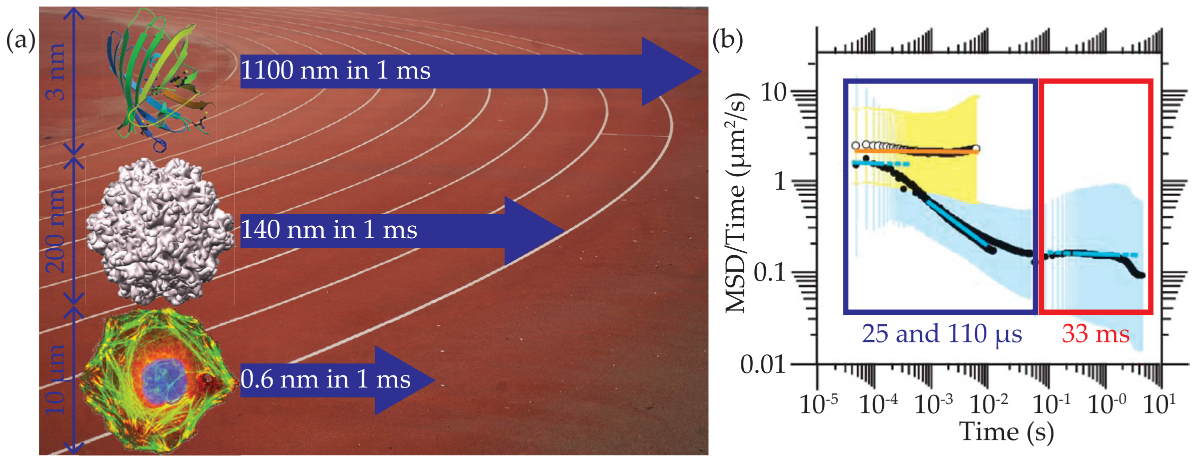

Figure 1.1: Orders of magnitude in nanoscale dynamics. (a) Average displacement of diffusing objects of various sizes in water at 37°C. Image sources: HeLa cell – Molecular Expressions (`http://micro.magnet.fsu.edu/`); virus capsid, GFP – Protein Data Bank (`http://www.rcsb.org/pdb/`); running track – `http://www.publicdomainpictures.net/`. (b) Reduced mean square displacement over time for gold-tagged DOPE lipids diffusing in the plasma membrane of FRSK cells at different time resolutions as indicated by the labeled boxes. The experiments were done with intact (blue line fits) and disrupted actin cytoskeleton (orange fit). Adapted from Murase et al. (2004).

temporal regime that SPT must access to probe the behavior of cellular organelles or macromolecular machines.

For a more quantitative example of "how fast" such a microscope needs to be to detect a certain dynamic behavior, consider Figure 1.1b. It displays the reduced MSD (i.e. MSD divided by time) for a gold-tagged phospholipid diffusing in the cellular plasma membrane as measured by Murase et al. (2004). The data in the red box was recorded at 33 ms temporal resolution. The resulting linear fit (blue line) shows a slope of zero, indicating free diffusion (see Chapter 2.3 for details on different modes of motion and their characteristic signatures).

The picture changes completely when the same experiment is repeated at temporal resolutions of 25 and 110 μs, as shown in the blue box. The fit (blue line) now shows a negative slope—a sign of corralled diffusion, i.e. intermittent trapping of the lipid in membrane compartments or "lipid rafts". This behavior is entirely invisible to a measurement with insufficient time resolution.

The measurements shown in Figure 1.1b use lipid-tethered gold spheres as labels, i.e. the contrast is provided by light scattering. This provides a strong and stable signal; detection efficiency is therefore not the main concern in designing experiments. This allows for the use of very fast detectors such as conventional complementary metal-oxide semiconductor (CMOS) cameras (Fujiwara et al., 2002).

However, the most widely used contrast mechanism for in-vivo microscopy is fluorescence (Pawley, 2006), where signal conditions are less favorable. The prevalence of fluorescence microscopy in biological imaging is due to its unique properties: the availability of endogenous probes like the GFP, the resulting superior labeling specificity, the small size of fluorescent probes, and the possibility to monitor several molecular species simultaneously in multi-color experiments.

Fluorescence-based single particle tracking microscopy (SPTM) has been used to investigate the dynamics of a variety of biological nanoscale objects, including proteins (Goulian and Simon, 2000; Yildiz et al., 2003), lipids (Fujiwara et al., 2002; Schmidt et al., 1996), vesicles (Li et al., 2004), polynucleotides (Lange et al., 2008), and viruses (Brandenburg and Zhuang, 2007). In the simplest case, this is done by recording a time series of two-dimensional images in a conventional widefield microscope[1], followed by post-processing to identify particles and assign trajectories.

Fluorescent signals, especially those emitted from single molecules, are of much smaller intensity then those available in scattering experiments. Additionally, most fluorophores undergo photobleaching when excited repeatedly (Lakowicz, 2006), resulting in a fixed overall photon budget. This creates a trade-off between the number of photons available per individual measurement and the total number of measurements that can be performed.

These characteristics create challenging requirements for achieving sub-millisecond temporal resolution in fluorescent SPT. To make the best use of the available signal, high detection efficiency and effective background suppression are crucial. Photobleaching both in the current region of interest (ROI) and in adjacent regions must be controlled and limited.

## 1.2 Thesis Outline

The goal of this thesis was the implementation and demonstration of an instrument that addresses these difficulties and provides three-dimensional tracking of fluorescent objects in living cells with a temporal resolution in the 100-µs range.

Two basic strategies have previously been pursued in adding the third dimension to particle tracking experiments (Dupont and Lamb, 2011). The first strategy modifies regular widefield detection to provide additional information about the axial (z) position of the particles under observation. In the second strategy, 3D position information is extracted by either scanning the surrounding volume of the particle in circular orbits with a laser focus, yielding a position-dependent signal modulation, or by the use of a spatial arrangement of several point detectors. As the field of view is limited to the immediate vicinity of the observed particle, a feedback mechanism is used to move the position of the observation volume in real time. This concept achieves typical time resolutions of about 5–30 ms (Cang et al., 2008).

---

[1] i.e. a microscope in which an extended field of view is illuminated

In designing our SPT microscope, we opted for a hybrid approach. The goal of sub-millisecond temporal resolution strongly suggested a feedback-driven framework. At the same time, sensitivity was crucial, and a flexible way of switching between confocal and widefield readout highly desirable.

The resulting instrument, whose design, implementation, characterization, and application is the subject of this thesis, combines electron-multiplying CCD (EM-CCD) readout with fluorescence excitation by a focused laser beam. 3D localization is provided by a "Biplane" detection scheme that we originally developed for localization-based super-resolution microscopy (Juette et al., 2008; Mlodzianoski et al., 2009). Here, I use a modified version of the Biplane idea, in which two small ROIs of 5 × 5 pixels each correspond to two axially shifted observation areas in the sample. Reading out only five lines of the camera enables frame rates up to 7.5 kHz (130 µs temporal resolution). Beam-steering retains the particle in focus and keeps its image position fixed to the two ROIs on the camera chip. The small size of the ROIs makes them act as confocal pinholes, suppressing background and enabling optical sectioning (while providing a view of the intensity distribution within the "pinhole").

In the initial implementation (Juette and Bewersdorf, 2010), beam-steering was accomplished by means of a tiltable piezo mirror for lateral (x,y) movement and a piezo-actuated objective holder for axial (z) movement. Motivated by the comparatively slow response of the objective piezo and concerns of coupling piezo motion into the sample through the immersion medium, I subsequently implemented a fast remote focusing mechanism based on adaptive optics to eliminate both issues. The potential suitability of a deformable mirror for this purpose had been suggested previously (Juette, 2009).

After giving an overview about the field of single particle tracking and an introduction to adaptive optics, I describe in detail the rationale and implementation of the instrument and discuss experimental results that characterize the performance of the instrument. Measurements with fluorescent beads were performed to determine the temporal response and localization precision. Further experiments evaluate the range of velocities (in directed motion) and diffusion coefficients (in Brownian motion) that can be tracked. I also demonstrate the potential for biological applications. Retroviral particles are tracked as they undergo actin-driven directed motion on the plasma membrane of living cells, and trajectories of intracellular transport vesicles are recorded. Additional proof-of-principle experiments demonstrate the capability to detect single fluorophores on proteins labeled with organic dye molecules.

I am including brief accounts of some publications with my involvement that were not integral parts of this thesis project. They nevertheless shaped the ideas and methods presented here. These sections are labeled "Related work".

# 2

# Fundamentals of Single Particle Tracking

> I never cared much for moonlit skies
> I never winked back at fireflies
> But now that the stars are in your eyes
> I'm beginning to see the light
>
> *"I'm Beginning to See the Light"*
> Lyrics by Don George (1944)

This chapter provides an overview of the current state of the art in fluorescence single particle tracking microscopy (SPTM). I will begin with a discussion of the the central idea of SPTM: the precise determination of the position of a "small" (i.e. typically sub-diffraction sized) object from its image, a pixelated and often noisy intensity distribution. The characteristics of the relevant intensity distributions are introduced, and methods for finding their center in two and three dimensions are presented.

After a brief highlight on pointillism microscopy, an exciting recent application of single-molecule localization, I proceed to a survey of the various technological concepts that have been pursued in SPTM, with an emphasis on 3D methods. This discussion of the methods for acquiring single particle trajectories is followed by an introduction to trajectory analysis based on mean square displacements (MSDs): how is the quantitative information contained in the trajectory of an object extracted and categorized?

## 2.1 Single Particle Localization

In order to determine the position of an object by optical means, the spatial distribution of light emitted by the object must be registered by a spatially resolved detector or, equivalently, scanned using a temporally resolved detector. There must be at least two detection points along each direction. Alternatively, intrinsic or artificially introduced asymmetries of the intensity distribution can be exploited to extract positional information. Before discussing practical implementations of these principles, I will describe the fundamental nature of intensity distributions encountered in a fluorescence microscope.

### 2.1.1 Image Formation in Fluorescence Microscopy

The theoretical description of optical image formation by fluorescence commonly relies on the assumption that the microscope is a space-invariant linear system. The linearity is guaranteed by the incoherent nature of fluorescence: the image is described by a superposition of intensities, rather than electric fields. Space-invariance translates to the condition that the impulse response of the system only depends on the distance between excitation and observation point. In practice, only an approximation of this behavior can be achieved; the following should be thought of as a local description of the imaging properties of the microscope (see Section 3.4 for a "reality check" of the space-invariance assumption).

If the imaging system is linear and space-invariant, the observed intensity distribution $i$ in image space can be obtained as the convolution of the object function[1] $o$ with the system's translationally invariant point-spread function (PSF) $h$,

$$i(\boldsymbol{r}) = \int \mathrm{d}^3 r' \, o(\boldsymbol{r'}) h(\boldsymbol{r} - \boldsymbol{r'}), \tag{2.1}$$

where $\boldsymbol{r}$ and $\boldsymbol{r'}$ are the coordinate vectors in the image and the sample, respectively.

By Fourier-transforming Equation 2.1, its content can be restated in terms of wave vector coordinates $\boldsymbol{k}$:

$$I(\boldsymbol{k}) = O(\boldsymbol{k}) H(\boldsymbol{k}). \tag{2.2}$$

$I$, $O$, and $H$ represent the Fourier transforms of $i$, $o$, and $h$, respectively. In Fourier space, the convolution with the PSF $h$ is replaced by a simple multiplication with the optical transfer function (OTF) $H$ of the system, which characterizes the system's response in the frequency domain. Note that the OTF always has a finite support—spatial frequencies beyond the support are not transmitted by the system. This is the Fourier space statement of the microscope's limited optical resolution.

The PSF itself is calculated from electromagnetic theory (Born and Wolf, 1999). In the case of a low numerical aperture (NA), it is well-approximated by a scalar field, disregarding polarization. In the optical far-field, the propagating focused field distribution generating the PSF can be considered as a superposition of plane waves. This leads to a Fraunhofer diffraction integral for the amplitude distribution $h_\mathrm{A}(\boldsymbol{r})$,

$$h_\mathrm{A}(\boldsymbol{r}) = \int \mathrm{d}^3 k \, H_\mathrm{A}(\boldsymbol{k}) \mathrm{e}^{\mathrm{i}\boldsymbol{k}\cdot\boldsymbol{r}}. \tag{2.3}$$

$h_\mathrm{A}(\boldsymbol{r})$ is called the coherent PSF of the system. The function $H_\mathrm{A}(\boldsymbol{k})$ weights the individual plane waves according to their amplitude contribution. It is the field amplitude

---

[1] The *object function* may be defined as the characteristic function of the sample, weighted with its local emitter strength.

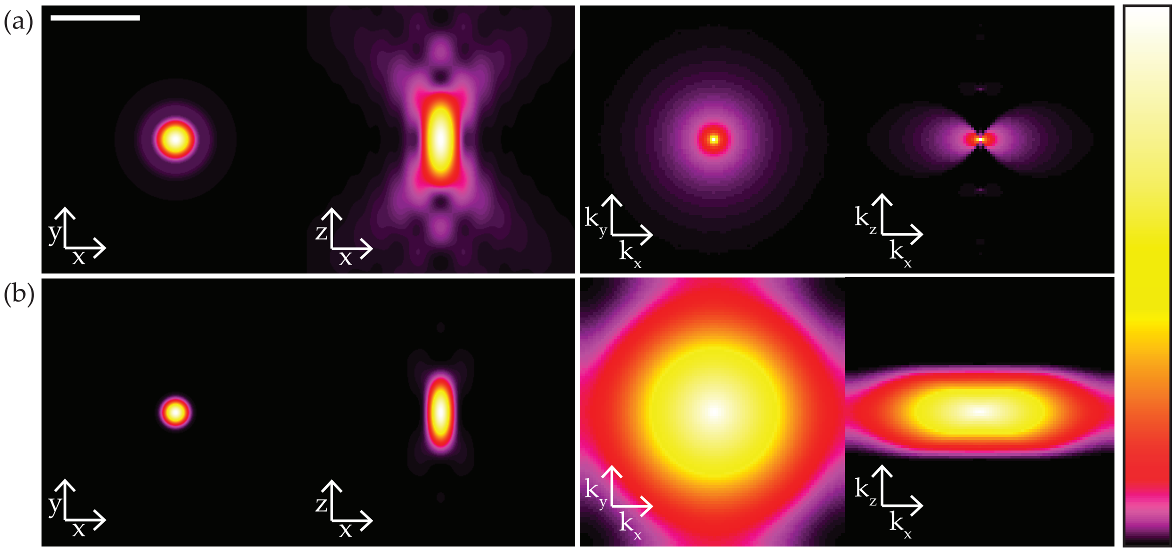

Figure 2.1: Point-spread function[2] (left panels) and optical transfer function (right panels) of a widefield microscope (a) and a confocal microscope (b). The color scale is normalized to the maximum intensity in each panel. PSF scale bar: 1 µm.

equivalent of the OTF, called the coherent OTF. The intensity PSF $h(\boldsymbol{r})$ is obtained as the squared absolute value of $h_\mathrm{A}(\boldsymbol{r})$. A typical PSF of a widefield microscope, as obtained numerically, is shown in Figure 2.1a, along with the corresponding OTF.

The effective PSF of a confocal microscope resembles the square of the widefield PSF (Figure 2.1b). More precisely, it is the product of its excitation and detection PSFs[3]

The support of the coherent OTF is a spherical "cap" defined by the angular bandwidth of allowed wave vectors. This angle range is given by the aperture angle of the objective. For a fixed wavelength $\lambda$, the cap is a two-dimensional manifold and can be projected onto a circular segment of the plane, yielding the complex-valued pupil function $P(\boldsymbol{k}) = P(k_x, k_y)$. This is a rescaled representation of the intensity and phase distribution in the back focal plane of the objective.

Using the pupil function, Equation 2.3 can be rewritten into a two-dimensional Fourier transform,

$$h_\mathrm{A}(\boldsymbol{r}) = \int \mathrm{d}k_x\,\mathrm{d}k_y\,P(k_x, k_y)\mathrm{e}^{\mathrm{i}(k_x x + k_y y)}\mathrm{e}^{\mathrm{i}k_z(k_x,k_y)z}, \tag{2.4}$$

where $k_z(k_x, k_y) = \sqrt{(n/\lambda)^2 - (k_x^2 + k_y^2)}$ and $n$ is the refractive index of the immersion medium. In the scalar approximation, the three-dimensional PSF is completely determined by the two-dimensional pupil function.

---

[2] Numerical calculation following Richards and Wolf (1959), assuming a 1.2 NA water immersion objective ($n = 1.333$), 488 nm excitation wavelength, 517 nm detection wavelength (emission maximum of Alexa 488), and random polarization.

[3] For a fluorescence microscope, these two "elementary" response functions differ slightly due to the wavelength difference between excitation and emission (Stokes shift) and the size of the detection pinhole.

In a high-NA system, polarization effects are significant due to the high focusing angles, which lead to a three-dimensional redistribution of polarization components. To account for these effects, a full vectorial treatment of the electric fields is required (Richards and Wolf, 1959).

### 2.1.2 Localization in Two Dimensions

The lateral full width at half-maximum (FWHM) $w$ of a PSF as shown in Figure 2.1 can be approximated by

$$w = \frac{\lambda}{2n\sin(\alpha)}, \tag{2.5}$$

where $\lambda$ is the wavelength of the detected light, $n$ the refractive index of the immersion medium, $\alpha$ the semi-aperture angle of the objective (and $n\sin(\alpha)$ its NA). This quantity was first recognized as the diffraction limit of optical resolution by Abbe (1873). According to the Rayleigh criterion (Hecht, 2001), two point sources can only be separated when their distance exceeds $w$.

The position of an isolated point source, however, can be determined with much higher accuracy. If the detection of $N$ photons is considered as a series of position measurements with standard deviation $\sigma_0 = w/(2\sqrt{2\ln(2)})$, the standard deviation of the mean is

$$\sigma = \frac{\sigma_0}{\sqrt{N}}. \tag{2.6}$$

The center position $(x_0, y_0)$ and other parameters, including amplitude $A$ and background $b$ can be estimated by fitting a suitable model function to the experimentally obtained intensity distribution. The most common approach (Carter et al., 2005; Cheezum et al., 2001; Saxton and Jacobson, 1997) is to fit a two-dimensional Gaussian,

$$g(x, y|x_0, y_0, A, b, \sigma_0) = A \times \exp\left[-\frac{(x-x_0)^2 + (y-y_0)^2}{2\sigma_0^2}\right] + b. \tag{2.7}$$

For applications where large numbers of particle positions must be determined quickly, e.g. in pointillism microscopy (Section 2.1.4), a variety of methods with smaller computational footprint can be used, including iterative centroid algorithms (R. E. Thompson et al., 2002), gradient-based determination of radial symmetry centers (Parthasarathy, 2012), and a variant of the Bancroft algorithm, whose original form is used for the satellite-bases global positioning system (GPS) (Andersson, 2008). Computational speeds can also be improved by making use of the highly parallel operation of graphics processing units (GPUs) (Smith et al., 2010).

The simple estimate of localization accuracy given in Equation 2.6 can be replaced by more sophisticated statistical analysis, using the Fisher information matrix of the imaging system to estimate a Cramér-Rao lower bound (CRLB) for the localization accuracy and other performance metrics (Chao et al., 2009; Ober et al., 2004). These studies have also shown that standard methods of data fitting using least squares as a merit function are not optimal for achieving CRLB-limited accuracy; they should be replaced by an optimized maximum-likelihood estimator (MLE).

### 2.1.3 Localization in Three Dimensions

Perhaps the conceptually simplest way to extend particle localization to the axial dimension is volumetric raster-scanning using a (confocal or two-photon) laser scanning microscope. Since the central lobe of the confocal PSF is reasonably well approximated by a 3D Gaussian, the standard method of fitting a Gaussian to localize a point emitter in two dimensions can easily be extended to this approach. While this is practical for localizing objects in fixed samples, limitations of the scanning speed prohibit tracking of fast dynamics. The method has, however, been used successfully for relatively slow dynamic processes (Arhel et al., 2006; Bornfleth et al., 1999).

An alternative is to infer axial information from the shape of an out-of-focus widefield intensity distribution, such as the width of the central maximum or the diameter of surrounding rings (Speidel et al., 2003). However, these features are usually symmetric in z, leaving an ambiguity as to the actual particle position.

This ambiguity can be avoided by creating distinct axial asymmetries via the introduction of specific aberrations. Kao and Verkman (1994) placed a weak cylindrical lens in the detection beampath of a widefield SPTM, resulting in a slightly astigmatic PSF. Moving a point source out of focus produces an elliptical deformation of the observed focal spot along one of two perpendicular orientations, depending on the direction of axial displacement (Figure 2.2a). Gaussian fitting with two independently varying width parameters can be used to determine the axial position of the emitter from a calibration curve. This approach has been used for tracking quantum dots in cells (Holtzer et al., 2007) and, more recently, for a 3D version of stochastic optical reconstruction microscopy (STORM) (B. Huang et al., 2008; see Section 2.1.4 for an overview of STORM and related methods of “pointillism” microscopy).

Figure 2.2b illustrates a related but more complex approach based on PSF engineering: placing an appropriately designed phase mask in a plane conjugated to the objective pupil (i.e. in Fourier space with respect to the image), a PSF consisting of two helically twisted lobes can be generated (Pavani and Piestun, 2008). The relative orientation of the two lobes is a function of axial depth. Like astigmatism, this has been used both for particle tracking (M. A. Thompson et al., 2009) and for pointillism microscopy (Pavani et al., 2009; discussion of pointillism microscopy in Section 2.1.4). In comparison to astigmatism, the double helix PSF features an extended axial range and a more constant performance in lateral localization precision as a function of depth; a tradeoff lies in the fact that the two lobes limit observable particle densities and decrease total signal-to-noise ratio (SNR).

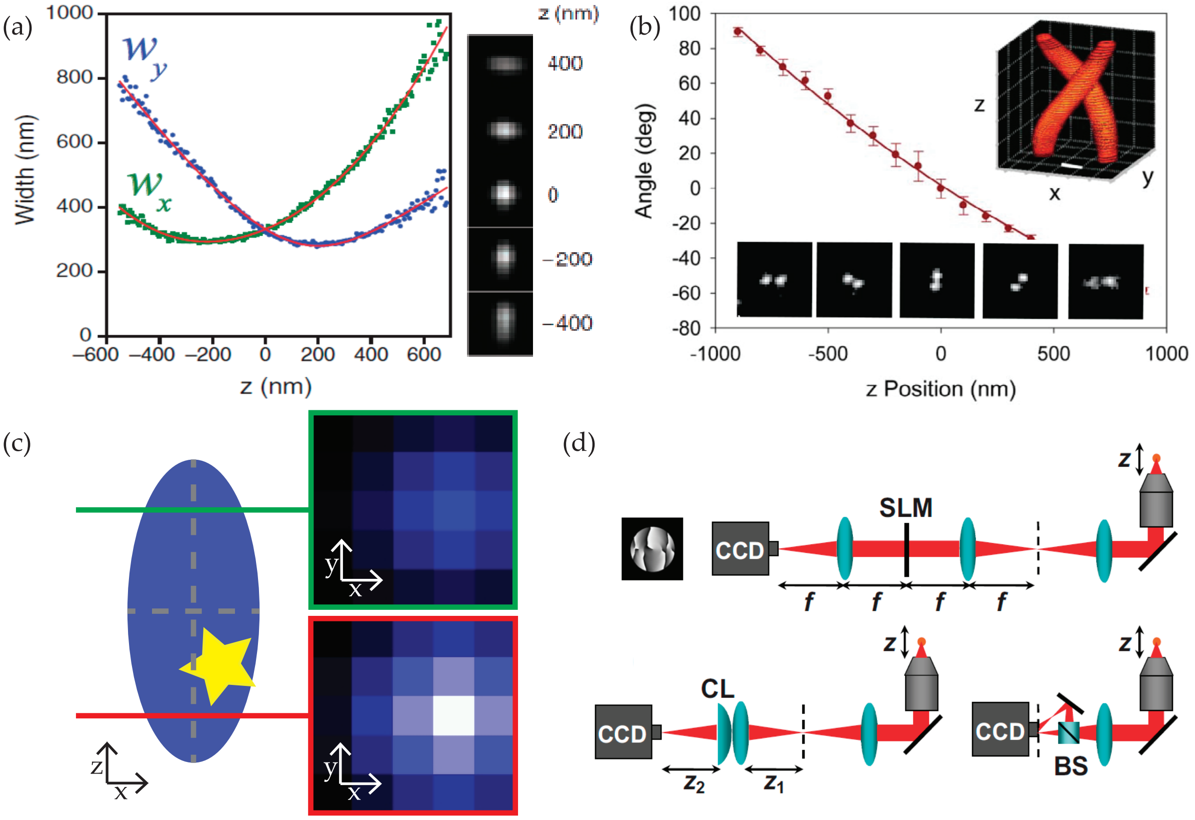
(a)
1000
800
600
400
200
0
Width (nm)
$w_y$
$w_x$
−600 −400 −200 0 200 400 600
z (nm)
z (nm)
400
200
0
−200
−400
(b)
100
80
60
40
20
0
-20
-40
-60
-80
Angle (deg)
z
x
y
-1000 -500 0 500 1000
z Position (nm)
(c)
z
x
y
x
y
x
(d)
CCD
SLM
f f f f
z
CL
CCD
z₂ z₁
z
CCD
BS
z

Figure 2.2: Illustration of three methods for axial particle localization. (a) Placing a cylindrical lens in the detection beam path creates astigmatic distortion of the PSF for out-of-focus planes. The $z$ position is obtained by fitting the the width parameters $(w_x, w_y)$ independently. Adapted from B. Huang et al. (2008). (b) Placing a specific phase mask in a telecentric plane generates a PSF with two helically twisted lobes. Their relative orientation encodes z position. Adapted from Pavani et al. (2009). (c) In Biplane, the two planes represent two voxels along the $z$ direction. The intensity distribution can be fitted directly to determine the position of a particle in the observation volume (represented here as a blue laser focus). (d) Schematic of the practical implementations of the double helix (top), astigmatic detection (bottom left) and Biplane (bottom right). Adapted from Badieirostami et al. (2010)

A third approach, which we chose to pursue with our SPT instrument, splits the detection beam path into several (typically two) branches of different lengths to enable simultaneous observation of several sample planes (Figure 2.2c). Originally conceived to correlate imaging of the plasma membrane with events deeper inside the cell (Prabhat et al., 2004), this idea has since been used for three-dimensional widefield particle tracking (Toprak et al., 2007) and has formed the basis for 3D localization in our Biplane fluorescence photoactivation localization microscopy (FPALM) instrument (Juette et al., 2008 and Section 2.1.4) .

All the approaches described so far provide an axial localization precision that is approximately by a factor of three worse than its lateral counterpart. This is due to the higher axial width of the PSF (compare Equation 2.6) and therefore intrinsic to any method using a conventional microscope geometry. Axial improvement of the PSF is the goal of 4Pi confocal microscopy (Hell and Stelzer, 1992) and its widefield counterpart, $I^5M$ (Gustafsson et al., 1999), which coherently combine two opposing objective lenses to increase the effective NA of the system. This leads to an up to sevenfold increase in axial resolution. Combined with single-molecule localization, the 4Pi geometry has been used for nearly isotropic resolution in pointillism microscopy (Shtengel et al., 2009). The complex and alignment-sensitive interferometric design of 4Pi is difficult to use in live-cell imaging and, to my knowledge, has not been used for SPT despite the superior 3D localization.

#### Related Work: Comparison of 3D Localization with Biplane and Astigmatic Detection

Due to the importance of 3D localization in both particle tracking and pointillism microscopy (Section 2.1.4), we conducted a study (Mlodzianoski et al., 2009) to compare the performance of astigmatism and Biplane. This work was performed on a modification of our original 3D FPALM setup (Juette et al., 2008), in which the Biplane beam splitter cube could optionally be replaced by a cylindrical lens.

Three-dimensional fitting was done with a newly developed algorithm using a measured PSF as the model (Juette, 2009). This intrinsically accounts for system aberrations and can easily be adapted to any localization scheme. To provide interpolation of the 3D PSF data set while retaining a maximum of information, we implemented a subpixel position-shift routine based on 3D Fourier transforms.

The problem of estimating the value of a sampled function at a certain point of interest $\boldsymbol{r}-\boldsymbol{a}$ can be interpreted as the problem of shifting the whole function by the amount necessary to make the nearest node $\boldsymbol{\xi}_l$ coincide with $\boldsymbol{r}-\boldsymbol{a}$. Mathematically, this can be achieved by convolving the function with a Dirac delta distribution:

$$\mathrm{h}_{\boldsymbol{a}}(\boldsymbol{r}) = \mathrm{h}(\boldsymbol{\xi}_l) \otimes \delta\left(\boldsymbol{\xi}_l - \mathbf{D}_{\boldsymbol{a}}(\boldsymbol{r})\right), \tag{2.8}$$

where $\mathbf{D}_{\boldsymbol{a}}(\boldsymbol{r}) = \boldsymbol{\xi}_l - [\boldsymbol{r}-\boldsymbol{a}]$ describes the vector between the position $\boldsymbol{r}-\boldsymbol{a}$ and its closest neighbor $\boldsymbol{\xi}_l$. In Fourier space the convolution assumes the simple form of a multiplication,

$$\begin{aligned}\mathcal{FT}\left\{\mathrm{h}_{\boldsymbol{a}}(\boldsymbol{r})\right\} &= \mathcal{FT}\left\{\mathrm{h}(\boldsymbol{\xi}_l)\right\} \times \mathcal{FT}\left\{\delta\left(\boldsymbol{\xi}_l - \mathbf{D}_{\boldsymbol{a}}(\boldsymbol{r})\right)\right\} \\ &= \mathrm{H}(\boldsymbol{k}_l) \times \exp\left(-\mathrm{i}\boldsymbol{k}_l \cdot \mathbf{D}_{\boldsymbol{a}}(\boldsymbol{r})\right).\end{aligned} \tag{2.9}$$

$\mathrm{H}(\boldsymbol{k}_l)$ is the OTF of the system. It is calculated once at the beginning of the procedure as the Fourier transform of $\mathrm{h}(\boldsymbol{\xi}_l)$. Multiplication with the phase factor $\exp\left(-\mathrm{i}\boldsymbol{k}_l \cdot \mathbf{D}_{\boldsymbol{a}}(\boldsymbol{r})\right)$ and inverse Fourier transform yield the shifted function $\mathrm{h}_{\boldsymbol{a}}(\boldsymbol{x})$.

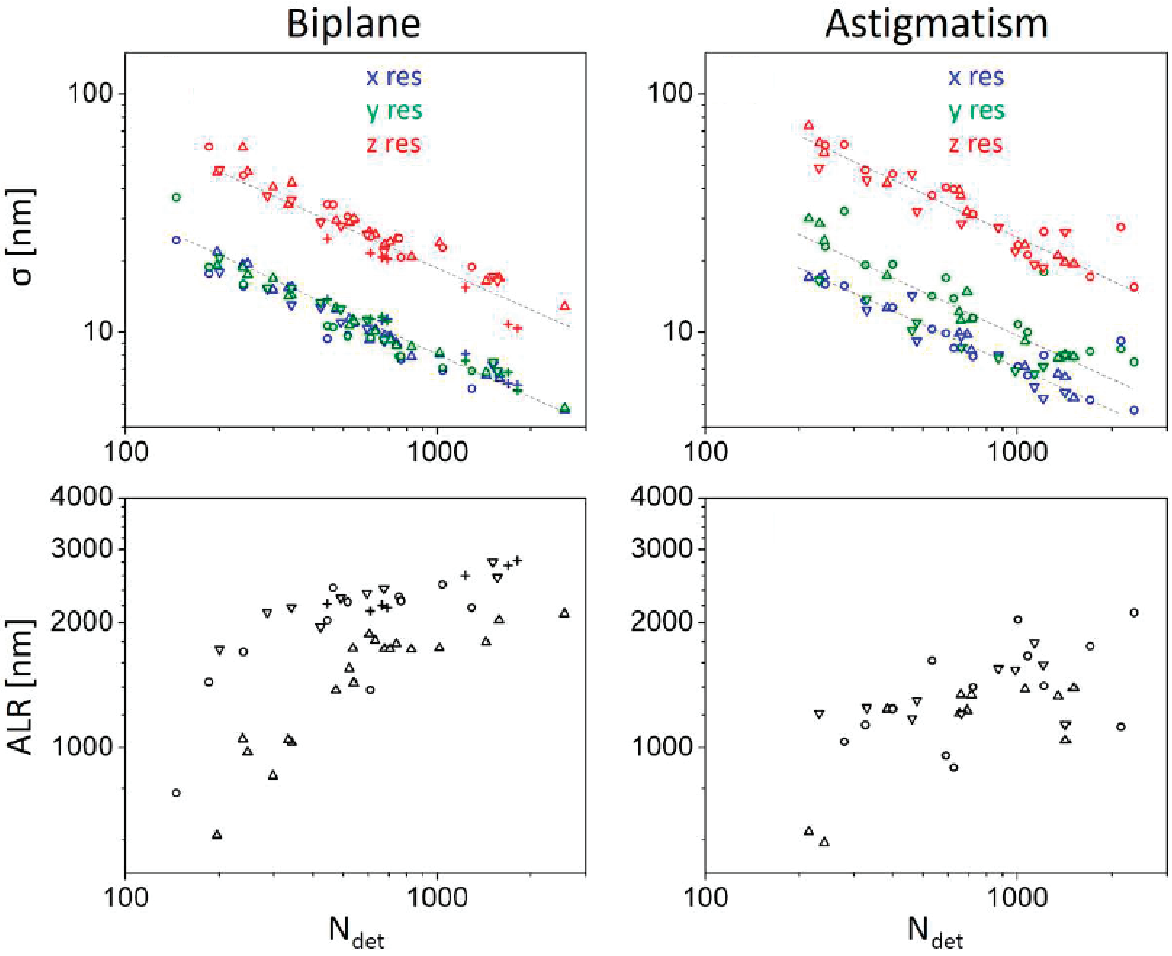

Figure 2.3: Experimental comparison of 3D localization with Biplane (left panels) and astigmatism (right panels). The top panels show the localization precision (standard deviation) for a single fluorescent bead as a function of the number of detected photons. The bottom panels show the axial localization range (ALR), i.e. the range over which each particle could be localized in at least 50 of the recorded frames. Adapted from Mlodzianoski et al. (2009).

Some of the key results of the experimental comparison are summarized in Figure 2.3. Overall, Biplane had a slightly better localization precision, greater axial range for reliable localization, and better uniformity of localization over the useful axial range. These findings were independently confirmed by numerical comparisons applying CRLB analysis to Biplane, astigmatism, and double helix localization (Badieirostami et al., 2010). Based on these results, we chose Biplane as the localization method for the single particle tracking microscope (SPTM).

### 2.1.4 Pointillism Microscopy

As mentioned before, single-molecule localization is a fundamental component of a family of super-resolution fluorescence imaging methods, independently developed under the names of photoactivated localization microscopy (PALM) (Betzig et al., 2006), fluorescence photoactivation localization microscopy (FPALM) (Hess et al., 2006), and stochastic optical reconstruction microscopy (STORM) (Rust et al., 2006). These methods circumvent the diffraction limit by constructing an image as a map of individually localized fluorescent molecules. At any given time, the set of visible molecules must be sparse, so that their diffraction-limited images do not overlap[4]. This is achieved by keeping a majority of the probe molecules in a non-fluorescent dark state, from which many of them successively return to the ground state in a stochastic manner; these molecules are then excited, imaged, and localized until they photobleach. Over time, a super-resolved micrograph accumulates (Figure 2.4), much like a pointillist painting is composed of a large number of paint spots.

Initially, pointillism microscopy relied on photoswitchable or photoactivatable fluorophores, which initially reside in a (native or optically induced) dark state. A conformation change induced by low-intensity "activation" light converts them to their fluorescent form. It has since been realized (Fölling et al., 2008; Heilemann et al., 2008) that almost all common fluorophores can be used and an activation laser is generally unnecessary: by irradiating the sample with a high intensity of the excitation wavelength, the majority of fluorophores can be pumped into a non-fluorescent triplet or ionized free radical state (typically aided by the presence of a reducing agent in the imaging buffer, see Linde et al., 2011). Subsequently, stochastic subsets of the molecules return to the singlet system and can be imaged.

#### Related Work: Biplane Fluorescence Photoactivation Localization Microscopy

Our 3D pointillism microscope uses two-plane detection for 3D localization and was therefore dubbed Biplane FPALM. The first implementation (Juette et al., 2008) included a 405 nm solid state laser for activation and a 488 nm Argon laser for excitation of photoactivatable fluorophores emitting in the green, such as PA-GFP and caged fluorescein. It has later been extended to provide multiple laser lines for multicolor imaging (Mlodzianoski et al., 2011).

Images are recorded on an EM-CCD camera and a region of interest (ROI) around each detected molecule is determined by a variant of the CLEAN algorithm (Högbom, 1974), which is also the basis of particle identification in most SPT analysis. In short, the algorithm smoothes each camera frame with a Gaussian kernel, detects the brightest spot, adds its position to the ROI list, and sets adjacent pixels to zero. This procedure is repeated until all features above a set threshold have been determined.

---

[4] This condition has recently been made less strict by new fitting methods for overlapping particle images (Cox et al., 2011; F. Huang et al., 2011; Zhu et al., 2012)

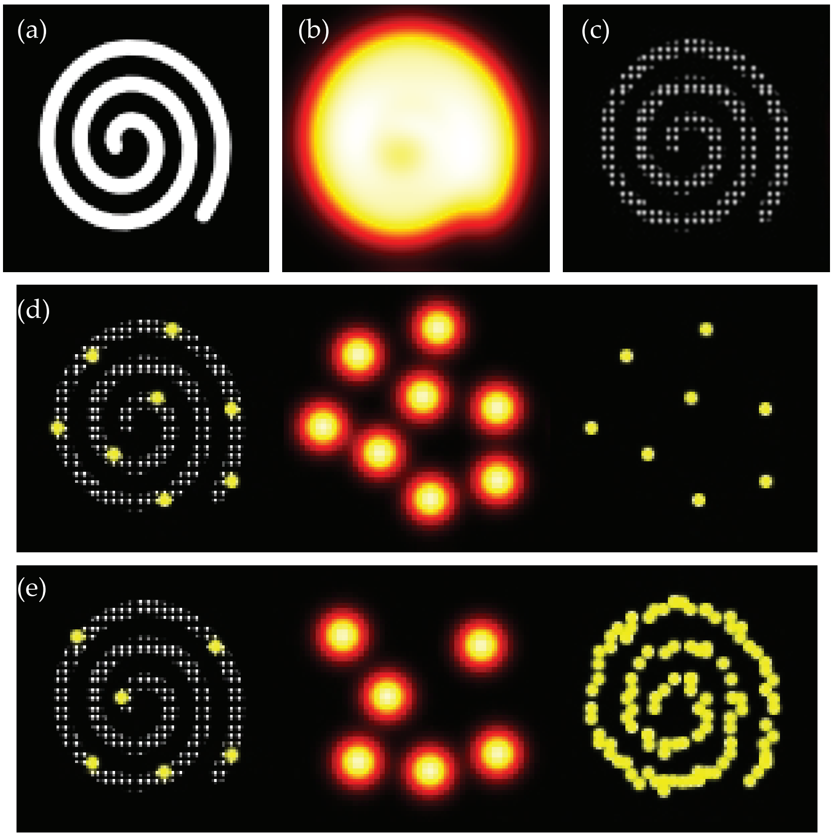

Figure 2.4: Principle of pointillism microscopy. A microscopic structure (a), whose nanoscale features are conventionally obscured by diffraction (b), is labeled with a population of fluorescent probe molecules that can be made to reside in a non-fluorescent dark state (c). Stochastic switching of sparse sets of molecules to their fluorescent form allows for their precise localization and reconstruction of a super-resolved molecular map of the sample (d–e).

Each ROI identified by the detection algorithm is then processed by the fitting routine described above. A high-resolution image is reconstructed by binning the recorded localizations into sufficiently small voxels to achieve Nyquist sampling at the expected localization accuracy.

We were able to achieve a 3D resolution of approximately 25 × 25 × 75 nm (x × y × z). Samples requiring a larger z range than the approximately 2 µm achievable with a single Biplane “slice" can be imaged by sequential recording of several z-positions and merging of the datasets. To establish the instrument’s capability for handling thick samples (like entire cell volumes), we imaged 4 µm polystyrene beads and were able to accurately reconstruct their spherical surface (Figure 2.5a). The instrument has grown into a tool for routine imaging of a variety of fixed biological samples (Figure 2.5b). Data analysis is now performed using the “SRX" software suite that ships with the commercial Biplane FPALM device (SR-200,

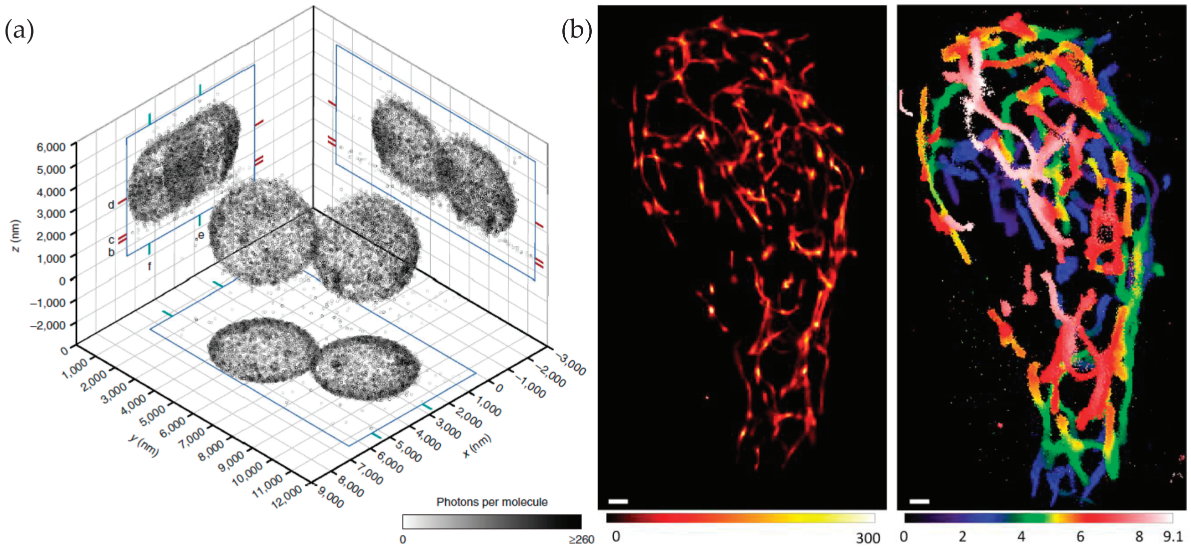

Figure 2.5: Examples of Biplane FPALM imaging. (a) 4 µm diameter polystyrene beads surface-labeled with caged fluorescein, reconstructed from ∼ 9,000 single molecule localizations. Adapted from Juette et al. (2008). (b) Mitochondrial network in a HepG2 cell labeled with mtEos2 (∼ $10^6$ localizations). The left panel shows a z projection of the 9 µm thick stack (with a color scale representing the number of localized molecules per pixel), the right panel shows the same data with a color scale encoding the z position in micrometers. Scale bars: 1 µm.Adapted from Mlodzianoski et al. (2011).

Vutara) based on our original design.

## 2.2 Survey of 3D Single Particle Tracking Methods

The first successful attempts at nanoscale SPT in a biological context date as far back as thirty years. Early measurements were performed by attaching a video camera to a microscope and tracing the path of lipoprotein-receptor complexes on clear plastic sheets overlaid on a TV screen (Barak and Webb, 1982). The advent of digital video readout and processing allowed for automated determination of object positions and reconstruction of trajectories (e.g. the movement of kinesin-coated beads along microtubules: Gelles et al., 1988). This helped establish SPT as a widely used quantitative technique (Saxton and Jacobson, 1997).

Until recently, most SPT was restricted to analyzing two-dimensional (x,y) projections of motion obtained by conventional widefield imaging or total internal reflection fluorescence (TIRF) microscopy. This is closely linked to the fact that a sufficient SNR for the localization of small objects is most conveniently achieved by using in-vitro systems, such as motor proteins moving cargo along cytoskeleton components attached to a flat substrate (Gelles et al., 1988; Yildiz et al., 2003).

Within the last decade, advances in both optical components and methods as well as fluorescent probe development have rendered SPT in living cells more feasible. In this context, motion is inherently three-dimensional and often extends over several micrometers in depth. Methods to extend particle tracking into the third dimension can generally be subdivided into two categories (Dupont and Lamb, 2011): (i) methods using conventional microscopy to record an image sequence, which is then analyzed in post-processing to identify particles, determine their positions, and assign trajectories; (ii) methods using active feedback to track a particle in real time during its actual motion.

### 2.2.1 Analysis of Widefield Image Sequences

The methods in this first family are based on the ideas presented in Section 2.1.3. Images are recorded using a sensitive digital microscopy camera, typically an EM-CCD camera. Axial localization is achieved either by making use of the 3D information inherent in the detected intensity distribution (Prabhat et al., 2004; Ram et al., 2008; Toprak et al., 2007), or by introducing additional z-position sensitive aberrations (Holtzer et al., 2007; Kao and Verkman, 1994; M. A. Thompson et al., 2009).

Identification and localization of the particles in a recorded movie follows the same procedures as in pointillism microscopy (which, in fact, has frequently refined previously existing methods originating from the much older field of SPT). The next step is to group the obtained localizations into plausible trajectories. The reliability of this step depends on various factors, including the density of observed particles, their average displacement in the interval between to camera exposures, their probability to escape from the limited axial observation depth or to disappear due to photobleaching. Once probable trajectories are identified, the analysis proceeds to examine the underlying modes of motion (see Section 2.3).

The main advantage of these methods is their ability to acquire numerous trajectories simultaneously. A significant drawback of this strategy is that the depth over which particles can be localized and tracked is limited to about one or two micrometers (Mlodzianoski et al., 2009). In addition, these methods are very sensitive to high particle densities and background fluorescence.

### 2.2.2 Live Feedback

These drawbacks can be eliminated by feedback-based methods, albeit at the expense of simultaneous acquisition. The idea of a microscope that automatically keeps a moving object in focus dates back to a classic article by Berg (1971). In order to observe swimming bacteria over extended periods of time, the sample chamber of a darkfield microscope was equipped with an electro-mechanical transducer. This allowed for automated movement of the chamber based on a feedback signal generated by differential amplification of the output of an arrangement of optical

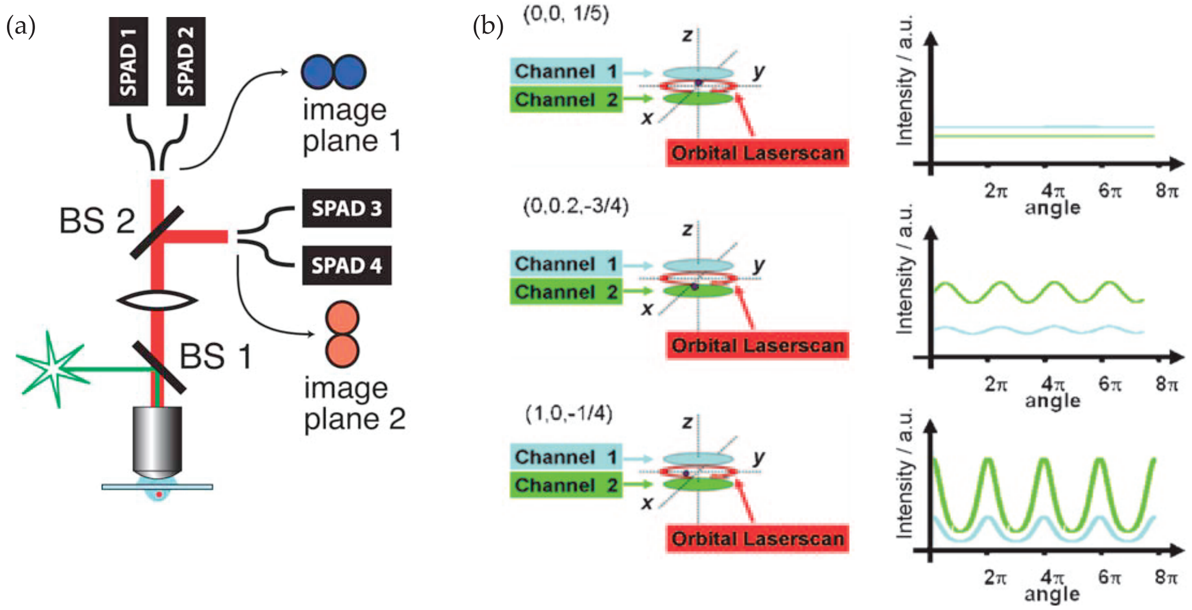

Figure 2.6: Particle tracking with feedback and confocal readout. (a) Using a bundle of optical fibers, a tetrahedral arrangement of detection points is imaged onto four single-photon avalanche photodiodes (SPAD). Adapted from Lessard et al. (2007). (b) In orbital tracking, a focused laser beam is scanned around the observation point in circular trajectories. The modulation in detected intensity encodes the particle position. In the implementation shown here, Biplane detection provides axial discrimination. Adapted from Katayama et al. (2009).

fibers monitoring the 3D position of the bacterium. Peters et al. (1998) adapted the idea to track scattering polystyrene beads with nanometer precision in 3D using a position-sensitive detector.

Several recent implementations of this principle have used confocal setups in often complex geometries requiring separate beampaths for lateral and axial tracking and multiple point detectors (Cang et al., 2006, 2007). Lessard et al. (2007), were able to track quantum dots diffusing in water-glycerol mixtures at millisecond temporal resolution with a scanning stage, using a tetrahedral arrangement of optical fiber tips, with fibers connected to single-photon counting avalanche photodiodes (APDs) for feedback. Their setup is shown in Figure 2.6a.

Figure 2.6b illustrates another successful feedback approach, originally proposed by Enderlein (2000): a laser focus is scanned in one or several rapid circular orbits around the particle of interest. This creates a characteristic temporal intensity modulation on the point detector, which can be fitted to infer the particle position.

Several groups have implemented 3D variants of this scheme. Levi et al. (2005) used it in a two-photon microscope and observed, among other processes, phagocytosis of beads with a temporal resolution of about 30 ms, limited by the scanning speed of the galvanometer mirrors. McHale et al. (2007) substantially improved the scanning speed by using acousto-optic modulators (AOMs). This, however, requires the use of a scanning stage for recentering the particle, as AOMs are not suitable for fluorescence descanning. Katayama et al. (2009) combined orbital scanning and one-photon excitation with a variant of Biplane detection as an improved method of axial position determination.

These feedback-based systems offer better time resolution, axial tracking range, and, due to the inherent confocalization, better optical sectioning and background suppression. However, they do not record a conventional image of the particle. Especially in a cellular setting, this poses the risk of misinterpreting the collected abstract signals. Two particles approaching each other or inhomogeneous background, for example, can easily escape detection, resulting in artifacts in particle localization. In addition, methods relying on fiber bundles to relay a set of observation points in the sample to point detectors such as APDs, sacrifice some of the quantum efficiency of the detectors by creating a “dark spot" in the center of the detection volume (Cang et al., 2008).

Our setup (Chapter 4.1) uses focused laser excitation similar to Figure 2.6a and Biplane detection on two pinhole-equivalent small regions of 5 × 5 pixels each on an EM-CCD camera chip. Real-time tracking uses a fast beam-steering system based on a two-axis piezo mirror for lateral motion and remote focusing with a micro-machined membrane deformable mirror (MMDM) for axial motion. This approach thereby combines the best of both worlds: fast 3D tracking at maximum detection efficiency.

## 2.3 Trajectory Analysis

Once a set of trajectories is recorded with any method of SPT, statistical analysis is performed to extract quantitative parameters of the observed types of motion. The most common tool in trajectory analysis is the computation of the mean square displacement (MSD) $\langle d^2(\tau)\rangle$, defined by

$$\langle d^2(\tau)\rangle = \frac{1}{T-\tau}\int_{\tau}^{T} \mathrm{d}t\,|\boldsymbol{r}(t)-\boldsymbol{r}(t-\tau)|^2, \tag{2.10}$$

where $\tau$ is the lag time, $T$ the duration of the trajectory, and $\boldsymbol{r}(t)$ the measured position at time $t$ (with $\boldsymbol{r}(0) = 0$ by definition). In practice, when $N$ discrete time steps $\boldsymbol{r}_i(i \in \{0,\dots,N-1\})$ of a trajectory are recorded, the discrete version of this definition has to be used:

$$\langle d_i^2\rangle = \frac{1}{N-1-i}\sum_{j=i}^{N-1} |\boldsymbol{r}_i - \boldsymbol{r}_{j-i}|^2. \tag{2.11}$$

Different types of motion lead to different characteristic types of MSD curves (Saxton and Jacobson, 1997). I will consider the commonly encountered types of motion in

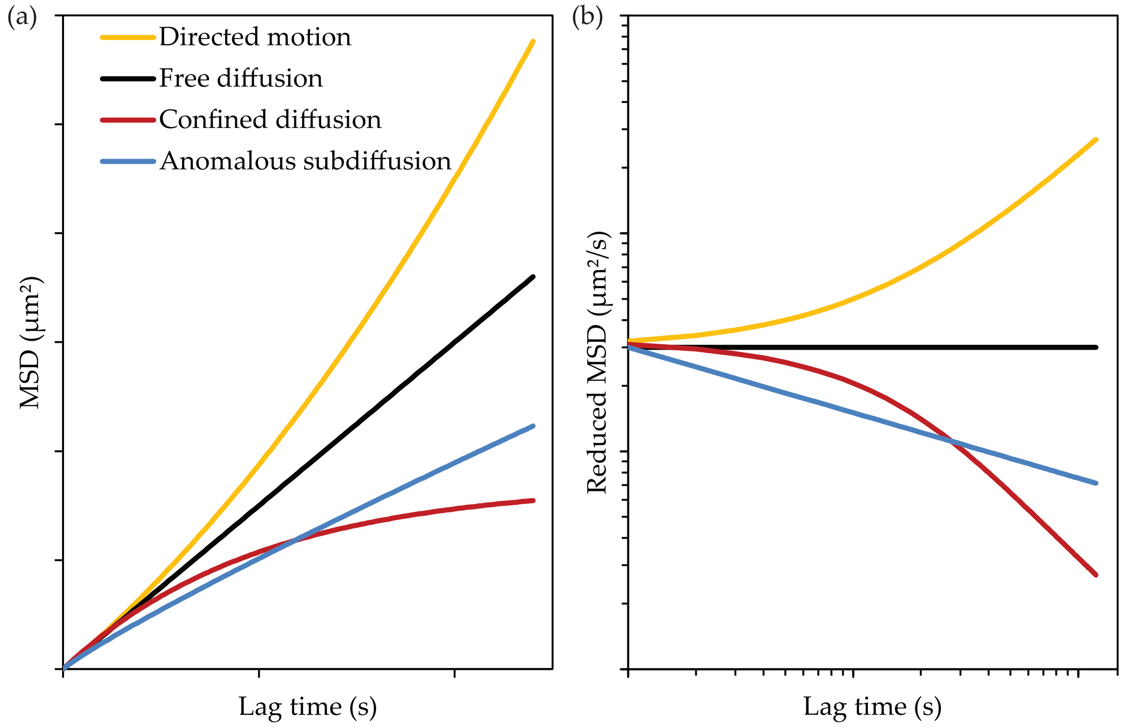

Figure 2.7: Identifying different types of motion by their characteristic footprint in the mean square displacement (MSD). (a) MSD curves of free diffusion (black), directed transport or flow plus independent diffusion (orange), anomalous subdiffusion as observed in corralled membranes (blue), and confined diffusion within an impermeable barrier (red). (b) A double-logarithmic plot of the reduced MSD, i.e. MSD divided by lag time, may highlight different regimes of motion more clearly than the linear representation.

SPT: free diffusion, directed motion, confined diffusion, and anomalous subdiffusion (Figure 2.7).

Free isotropic $n$-dimensional diffusion can be modeled as the superposition of $n$ independent orthogonal one-dimensional random walks $r_k(t)$ with time steps $\Delta t$. The mean displacement $\langle \Delta r_k \rangle = \langle r_k(t+\Delta t) - r_k(t) \rangle$ must be zero, since steps in both directions have equal probability. Making use of the fact that uncorrelated variances add up linearly, the MSD for the full $n$-dimensional process can then be obtained as

$$\begin{aligned} \langle \Delta d^2 \rangle &= \mathrm{Var}[\Delta r] + \langle \Delta r \rangle^2 \\ &= \sum \mathrm{Var}\left[\Delta r_k^2\right] + \sum \underbrace{\langle \Delta r_k \rangle^2}_{=0} = 2nD\Delta t, \end{aligned} \tag{2.12}$$

as the step size variance of each random walk must be $2D\Delta t$ to adequately represent Brownian motion (Einstein, 1905).

For 3D diffusion, the MSD is thus given by the linear function

$$\langle d^2(\tau)\rangle_{Diff} = 6D\tau. \tag{2.13}$$

If directional fluid flow or active transport along a linear structure with a velocity $v$ is present, a quadratic term must be added:

$$\langle d^2(\tau)\rangle_{Dir} = 6D\tau + (v\tau)^2. \tag{2.14}$$

Often, motion in cells looks like free diffusion on long time scales, but turns out to be partially inhibited by obstacles or intermittently confined to bounded areas. Such a case was examined in the introduction, where corralled diffusion of lipids in the plasma membrane was observed. This type of anomalous subdiffusion can be accounted for by introducing an exponent $\alpha < 1$ in Equation 2.13:

$$\langle d^2(\tau)\rangle_{Sub} = 6D\tau^{\alpha}. \tag{2.15}$$

Finally, diffusion may be entirely confined to a certain volume. The exact form of the MSD in this case depends on the geometry of the confinement volume. While expressions for several basic shapes (spheres, cubes etc.) have been derived (Saxton, 1995), I will limit this discussion to noting that the typical behavior is similar to

$$\langle d^2(\tau)\rangle_{Conf} = R^2 \left(1 - c_1 \mathrm{e}^{-6c_2 D\tau/R^2}\right), \tag{2.16}$$

which asymptotically approaches the square of the confinement radius $R$ for long lag times ($c_1$ and $c_2$ are constants characteristic of the confinement shape).

Often, different types of motion are dominant in different time regimes. This can be displayed more clearly by plotting a reduced MSD $\langle d^2_{\mathrm{Red}}(\tau)\rangle = \langle d^2(\tau)\rangle/\tau$ in double-logarithmic representation (Figure 2.7b).

In any experimental situation, additional factors like noise, localization uncertainty, integration time, and frame rate will affect the appearance of the observed MSD (Michalet, 2010).

# 3 Elements of Adaptive Optics

> Où finit le télescope, le microscope commence. Lequel des deux a la vue la plus grande ? Choisissez. Une moisissure est une pléiade de fleurs ; une nébuleuse est une fourmilière d'étoiles.
>
> *"Les Misérables"*
> VICTOR HUGO (1962)

Adaptive optics is the measurement and adaptive correction of phase aberrations in an imaging system, typically in a feedback loop. The concept was first proposed by Babcock (1953) to improve astronomical images by correcting for wavefront distortions caused by atmospheric turbulences; the first successful demonstration was reported more than twenty years later by Buffington et al. (1977). Adaptive optics is now routinely used to achieve better image quality in astronomy (Davies and Kasper, 2012), ophthalmology (Roorda, 2011), and microscopy (Booth, 2007).

Our single particle tracking microscope (SPTM) makes use of the fast wavefront shaping properties of a deformable mirror, one of the most common adaptive optical elements, as an axial beam-steering device. The proper operation of the mirror requires its characterization and optimization using wavefront sensing.

The aim of this chapter is to present the required background information on the theory and implementation of adaptive optical systems. In addition, it includes a "related work" summary concerning phase retrieval, a numerical method for reconstructing phase information from pure focal intensity measurements. This leads up to a short exposition on how phase retrieval can be used for characterizing and aligning a stimulated emission depletion (STED) microscope.

## 3.1 Aberration Theory in the Scalar Approximation

Adaptive optics in microscopy is mainly concerned with time-dependent phase aberrations arising from (fluctuating) refractive index inhomogeneities in the sample. These aberrations alter the imaging properties of the microscope, resulting in a compromised coherent OTF. In the scalar approximation, this is reflected in a compromised phase term of the complex-valued pupil function, which represents a planar projection of the coherent OTF (see Section 2.1.1). It can be interpreted as the intensity and phase distribution in the back focal plane of the objective. For this chapter, we will assume a unit disc representation of the pupil function $P(\rho,\theta) = p(\rho,\theta)\mathrm{e}^{\mathrm{i}\phi(\rho,\theta)}$, where $p(\rho,\theta)$ is the magnitude, $\phi(\rho,\theta)$ the phase term of the pupil function (with polar coordinated $\rho \in [0,1]$ and $\theta \in [0,2\pi]$).

It is convenient to represent the phase term $\phi$ in terms of a complete set of orthogonal polynomials on the unit disk. In aberration theory, Zernike polynomials $Z_n^m(\rho,\theta)$ (Zernike, 1934) are frequently used for this purpose. Their definition is

$$Z_n^m(\rho,\theta) = R_n^m(\rho) \times \begin{cases} \cos(m\theta), & \text{for } m > 0, \\ 1, & \text{for } m = 0, \\ \sin(m\theta), & \text{for } m < 0, \end{cases} \tag{3.1}$$

with $n \in \mathbb{N}_0$, $m \in \mathbb{Z}$, and $|m| \leqslant n$. The radial functions $R_n^m(\rho)$ are defined by

$$R_n^m(\rho) = \begin{cases} \sum\limits_{l=0}^{\frac{1}{2}(n-m)} \frac{(-1)^l\,(n-l)!}{l!\,\left[\frac{1}{2}(n+m)-l\right]!\,\left[\frac{1}{2}(n-m)-l\right]!}\,\rho^{n-2l}, & \text{for } n-m \text{ even}, \\ 0, & \text{for } n-m \text{ odd}. \end{cases} \tag{3.2}$$

Low-order Zernike polynomials correspond directly to classical optical aberrations, such as tip/tilt, defocus, astigmatism, coma, or various orders of spherical aberrations (Figure 3.1). Another useful property is the fact that the Fourier transform of a Zernike mode has a simple closed-form representation using Bessel functions (Noll, 1976).

Table 3.1 lists the explicit expressions for some low-order Zernike polynomials, their normalization coefficients, and the corresponding “elementary" aberrations. It uses a consecutive numbering of only the non-zero modes ($Z_k$ instead of $Z_n^m$) in such an order that, for each $n$, $m$ varies from lowest to highest.

With this numbering, the polynomials satisfy the orthogonality relation

$$\frac{1}{\pi}\int_0^1 \mathrm{d}\rho\,\rho \int_0^{2\pi} \mathrm{d}\theta\, Z_k(\rho,\theta)\, Z_l(\rho,\theta) = \frac{1}{N_k}\delta_{kl}, \tag{3.3}$$

where $\delta_{kl}$ is the Kronecker symbol and the normalization coefficients $N_k$ are

$$N_k = \left\{ \frac{1}{\pi}\int_0^1 \mathrm{d}\rho\,\rho \int_0^{2\pi} \mathrm{d}\theta\, \left[Z_k(\rho,\theta)\right]^2 \right\}^{-1}. \tag{3.4}$$

Introducing Zernike polynomials, the phase term of the pupil function becomes

$$\phi(\rho,\theta) = \sum_{k=0}^{\infty} a_k Z_k(\rho,\theta) \approx \sum_{k=0}^{K} a_k Z_k(\rho,\theta), \tag{3.5}$$

where the cutoff mode $K$ in the finite-order approximation is determined by the maximum number of polynomial nodes relevant for the system to be described.

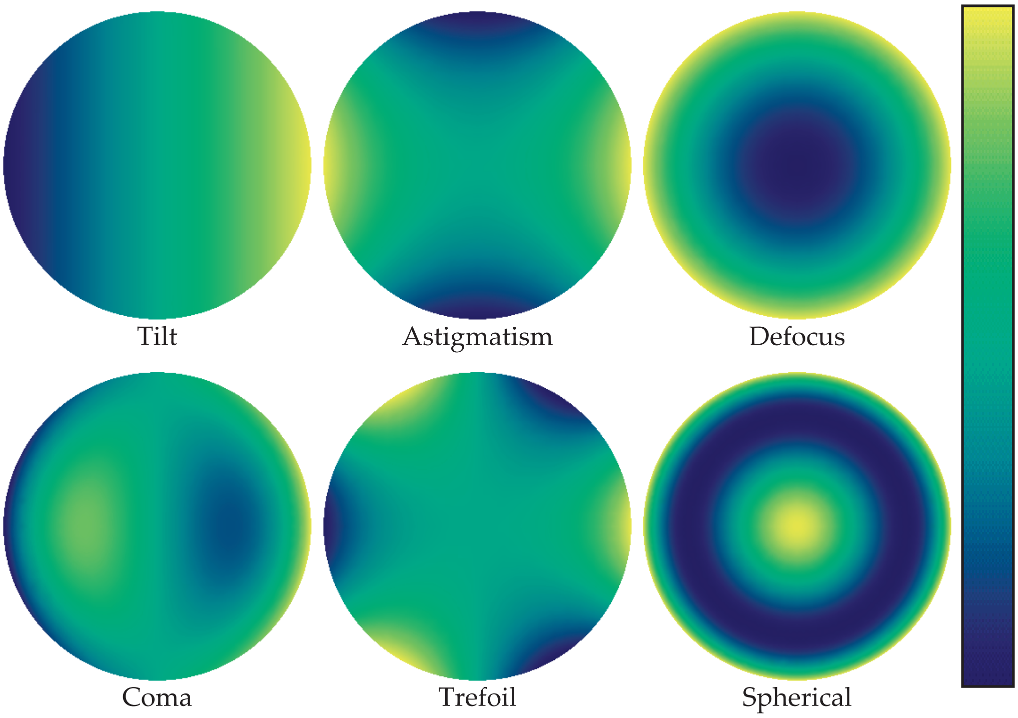

Figure 3.1: Zernike polynomials corresponding to classical low-order aberrations

| **Order** $n$ | **Mode** $k$ | **Norm. factor** $N_k$ | **Polynomial** $Z_k(\rho,\theta)$ | **Interpretation** |
|---|---|---|---|---|
| 0 | 0 | 1 | 1 | Piston |
| 1 | 1 | 4 | $\rho \sin \theta$ | Tilt in $x$ direction |
|  | 2 | 4 | $\rho \cos \theta$ | Tilt in $y$ direction |
| 2 | 3 | 6 | $\rho^2 \sin 2\theta$ | Astigmatism (±45°) |
|  | 4 | 3 | $2\rho^2 - 1$ | Defocus |
|  | 5 | 6 | $\rho^2 \cos 2\theta$ | Astigmatism (0°, 90°) |
| 3 | 6 | 8 | $\rho^3 \sin 3\theta$ | Trefoil |
|  | 7 | 8 | $(3\rho^3 - 2\rho) \sin \theta$ | Coma |
|  | 8 | 8 | $(3\rho^3 - 2\rho) \cos \theta$ | Coma |
|  | 9 | 8 | $\rho^3 \cos 3\theta$ | Trefoil |
| 4 | 10 | 10 | $\rho^4 \sin 4\theta$ | – |
|  | 11 | 10 | $(4\rho^4 - 3\rho^2) \sin 2\theta$ | Secondary Astigmatism |
|  | 12 | 5 | $6\rho^4 - 6\rho^2 + 1$ | Spherical aberration |
|  | 13 | 10 | $(4\rho^4 - 3\rho^2) \cos 2\theta$ | Secondary Astigmatism |
|  | 14 | 10 | $\rho^4 \sin 4\theta$ | – |

Table 3.1: Zernike polynomials up to fourth order

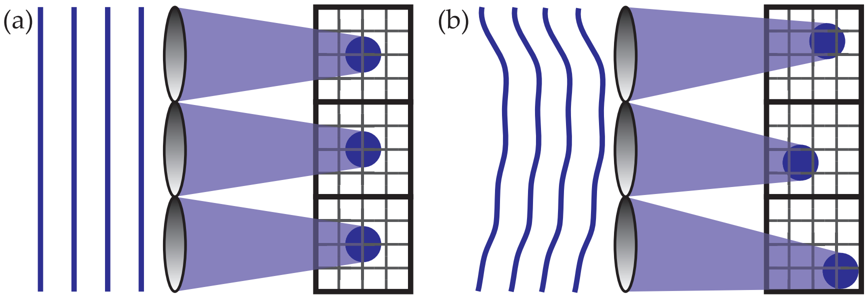

Figure 3.2: Function of a Shack-Hartman wavefront sensor. (a) For an incoming plane wavefront, the focal spots formed by all microlenses are centered on the respective sensor areas. (b) Distortion of the wavefront leads to local displacement of the spots.

## 3.2 Wavefront Sensing

Adaptive optics revolves around phase information of propagating light, which is not trivially accessible in typical microscope setups. Accurate phase information could be retrieved by an interferometer coupled into the beam path, but the precise alignment of such a system is cumbersome to maintain. A Shack-Hartmann wavefront sensor (SHWS) (Shack, 1971) solves this issue by providing a simple way to measure the shape of a wavefront (i.e. surface of constant phase) directly in the plane of interest, e.g. in the objective pupil plane.

The principle of a SHWS is illustrated in Figure 3.2. It consists of a digital camera (CCD or CMOS) whose chip is covered by a Hartmann mask, a rectangular array of microlenses, each of which covers an area of several pixels side length on the sensor. An incoming plane wave gets focused onto an array of focal spots centered under the respective lenslets. A distorted wavefront leads to local shifts of the spots, from which the local slope of the wavefront can be calculated. An estimate of the overall phase function can then be reconstructed (Southwell, 1980), usually in terms of Zernike coefficients.

In a typical adaptive optics system, the phase information reconstructed from the SHWS measurement is fed back to an adaptive element, e.g. a deformable mirror, to correct for dynamic aberrations in real time. In our case, the deformable mirror is only used for defocus and correction of defocus-induced spherical aberrations. Wavefront sensing is nevertheless important to characterize and optimize the instrument parameters of the deformable mirror.

## 3.3 Wavefront Shaping

Shaping of a wavefront, i.e. introduction of spatially resolved phase delays, is achieved by means of a transmissive or reflective element capable of generating varying optical path length differences across the field of view. In the simplest case, this can be a

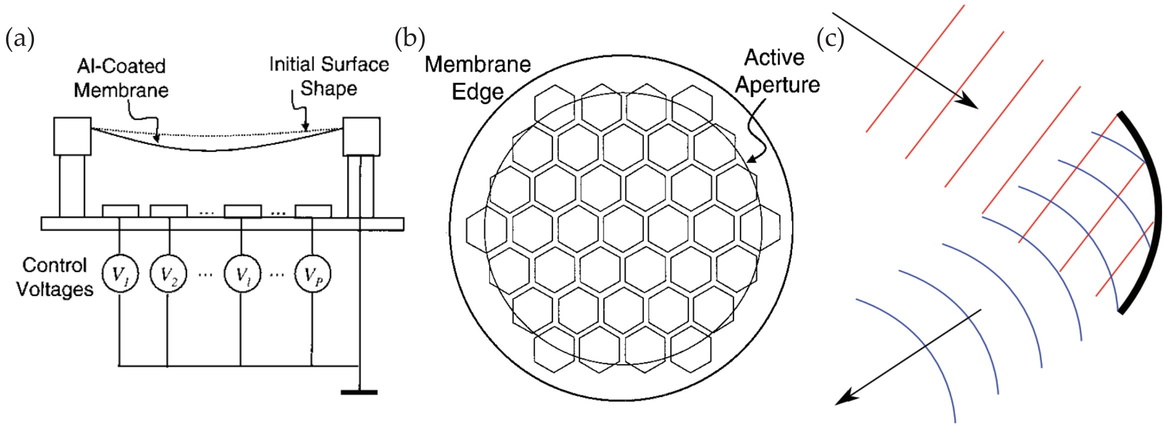

Figure 3.3: Wavefront shaping with a deformable mirror. Schematic side view (a) and top view (b) of a micro-machined membrane deformable mirror with a hexagonal electrode array. The reflectively coated membrane can be deflected by applying a set of control voltages $(V1, \ldots, V_N)$ across the air gap. Adapted from Zhu, Sun, and Fainman (1999) and Zhu, Sun, Bartsch, et al. (1999). (c) Generation of a spherical wavefront (blue) from a plane wavefront (red) by reflection at a spherical surface.

static phase mask, e.g. a vortex phase plate as commonly used in optical tweezers, STED microscopy, and other optical techniques (Züchner et al., 2011).

Adaptive wavefront shaping mainly uses two types of devices: spatial light modulators (SLMs) and deformable mirrors. A SLM is a pixelated nematic liquid crystal device, similar in function to a computer monitor. Controlling the voltage of the individual pixels generates a phase shift for linearly polarized light of a specific orientation. This is useful as a high-resolution programmable phase mask for laser applications and has been used, for instance, for focus shaping and aberration correction in stimulated emission depletion (STED) microscopy deep inside scattering tissue (Gould et al., 2012).

For random polarizations (e.g. in fluorescence detection), deformable mirrors are more suitable. The type we are using in the SPTM is a micro-machined membrane deformable mirror (MMDM) (Vdovin et al., 1997). It consists of a reflectively coated circular silica membrane fixed around the edge and suspended above a hexagonal array of thirty-seven electrodes (Figure 3.3a–b). Applying a pattern of control voltages to the electrodes generates local deflection of the mirror. The correct voltage array for a desired mirror shape (typically described in terms of Zernike coefficients) must be experimentally determined for a given mirror and setup geometry (see Chapter 5.1 for a description of our calibration procedure).

Our main use of the MMDM is to generate defocus, resulting in an axial shift of the laser focus in the sample. To second order, this requires a simple spherical shape of the mirror, transforming an incident plane wave into a converging spherical wave (Figure 3.3c). However, in combination with the objective lens, this produces fourth and higher order spherical aberrations, as explained in the following section.

## 3.4 Defocus with a Lens Satisfying the Sine Condition

Microscope objectives are generally optimized for the best possible approximation of a laterally translation-invariant PSF. This ensures homogeneous optical quality over a large field of view. Lens design seeks to guarantee this property by satisfying the optical sine condition for mapping rays from object space to image space (Born and Wolf, 1999). It is not possible to simultaneously achieve an axially translation-invariant PSF, which would require satisfying a different ray mapping condition, the Herschel condition (Born and Wolf, 1999).

Botcherby et al. (2008) imagined a point source placed at a position $(x, y, z)$ with respect to the origin of the principal sphere of a high-NA objective lens. They then derived an expression for the phase term of the generated pupil function and showed that, invoking the sine condition, it assumes the following form:

$$\phi(\rho, \theta | x, y, z) = nk \sin\alpha \left[ x\rho\cos\theta + y\rho\sin\theta + z\sqrt{\frac{1}{\sin^2\alpha} - \rho^2} \right]. \tag{3.6}$$

Here, $\alpha$ is the semi-aperture angle of the lens, $n$ the refractive index of the immersion medium, and $k$ the wavenumber in vacuum.

It can be seen from this equation that lateral displacement of the point source only produces tilt in the pupil. Axial displacement leads to a rotationally symmetric curved wavefront; however, this is not a purely spherical profile. Expansion in powers of $\rho$ leads to the high-NA defocus function $\phi_z(\rho)$ (the $z$ term of Equation 3.6),

$$\phi_z(\rho) = znk \left[ 1 - \frac{\rho^2 \sin^2\alpha}{2} + \frac{\rho^4 \sin^4\alpha}{8} + \dots \right]. \tag{3.7}$$

This explains why focusing a spherical wavefront using a high-NA objective lens results in a PSF corrupted by spherical aberrations. The consequence for remote focusing with our MMDM is that pre-correction of these aberrations must be performed by adding the appropriate negative phase terms to the mirror profile (Chapter 5.1).

It should be noted that in Biplane imaging, the same effect leads to some degree of spherical aberration in the PSF of at least one of the two image planes. However, the plane separation (500–800 nm) is small compared to the several micrometers of defocus range achieved by the deformable mirror, leading to a comparatively small decrease in imaging quality.

## 3.5 Phase Retrieval

While wavefront sensing and interferometry are adequate ways to acquire phase profiles, it is sometimes desirable to measure a pupil function without any modifications to the optical setup. It is possible, using numerical phase retrieval (Gerchberg and Saxton, 1972), to reconstruct the pupil function from the measured focal intensity distribution (PSF). In order to retrieve phase information, the Gerchberg-Saxton algorithm requires at least two images $h^{(i)}$ from different axial positions in the vicinity of the geometrical focus.

The algorithm starts with an initial guess for the pupil function (e.g. unity magnitude and zero phase). This pupil function is then multiplied by the defocus phase terms corresponding to the axial positions of the $h^{(i)}$, yielding pupil functions $P^{(i)}$ for each of these positions.

Fourier transforming the $P^{(i)}$ produces an initial set of coherent PSF sections $h_A^{(i)}$, whose amplitude terms are then discarded and replaced by the square root of the measured $h^{(i)}$. The new $h_A^{(i)}$ are used to calculate updated versions of the $P^{(i)}$, which are then averaged to create a new pupil function for the next iteration. This procedure is repeated until satisfactory convergence is achieved.

The Gerchberg-Saxton algorithm operates entirely in the scalar approximation; however, Hanser et al. (2004) developed an improved version to account for vectorial effects in high-NA objective lenses, making phase retrieval feasible for high-end microscopy systems (see also Hanser et al., 2003). Débarre et al. (2011) used a modified version of the method to characterize a deformable mirror.

### Related Work: Phase Retrieval in Stimulated Emission Depletion Microscopy

We developed the approach by Hanser et al. further with the goal to apply phase retrieval to the super-resolution microscopes built in our lab. This led to a new characterization and alignment tool for STED microscopy (Kromann et al., 2012).

In STED microscopy (Hell and Wichmann, 1994), diffraction-unlimited resolution is achieved by overlaying the excitation laser focus of a point-scanning fluorescence microscope with a ring-shaped intensity distribution, the STED focus, featuring an intensity zero in its center. The wavelength of the STED focus is tuned to the red spectral tail of the fluorophore’s emission spectrum, enabling it to depopulate the excited state by stimulated emission. A sufficiently high intensity of the STED focus leads to saturation of the stimulated emission process, i.e. depletion of the excited state. Only a narrow, diffraction-unlimited, central spot contains molecules that are able to return to the ground state by spontaneous fluorescence emission, creating a super-resolved image.

We applied a new noise removal method to image stacks of the STED focus, acquired by scanning a gold-bead. The denoised data could then be used for phase retrieval, reconstructing accurate representations of the vortex phase plate used for generating the STED focus (Figure 3.4a). The ability to accurately detect a shift of the phase mask from its optimal position can be used to facilitate beam alignment.

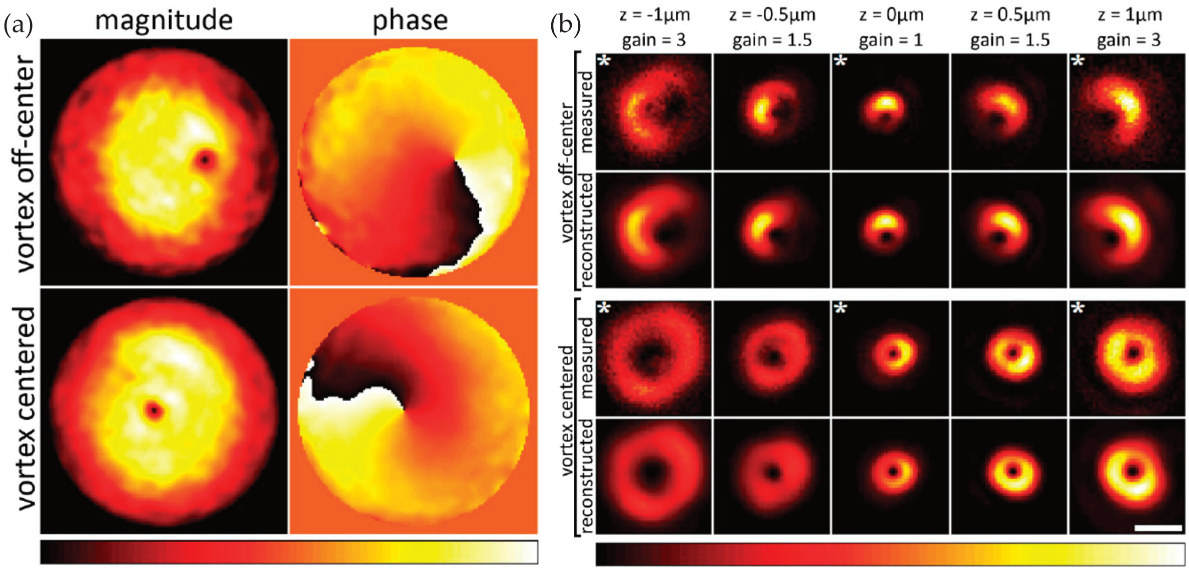
(a)
magnitude
phase
vortex off-center
vortex centered
(b)
z = -1µm gain = 3
z = -0.5µm gain = 1.5
z = 0µm gain = 1
z = 0.5µm gain = 1.5
z = 1µm gain = 3
vortex off-center
measured
reconstructed
vortex centered
measured
reconstructed
*

Figure 3.4: Phase retrieval in stimulated emission depletion microscopy. (a) Pupil magnitudes (left) and phases (right) retrieved from two measurements of the STED focus intensity distribution with the vortex phase mask in different positions (top and bottom). The phase ramp and line of singularity of the mask are accurately reproduced. Magnitude images are normalized to their maximum values. Dynamic range of phase images: $[-\pi, \pi]$. (b) First and third rows: z-stacks of measured STED foci. Second and fourth rows: STED foci reconstructed from the retrieved pupil functions (based on images marked by white asterisks). In each row, the intensities are normalized to the highest pixel intensity in that row after applying a gain to the images as indicated above each column. Scale bar: 1 µm. Adapted from Kromann et al. (2012).

Additionally, we were able to demonstrate that numerical reconstruction of the STED focus from the retrieved pupil function showed remarkably accurate results (Figure 3.4b). Phase-retrieved pupil functions, especially in combination with Zernike decomposition, can therefore provide an extremely compact model for the optical characteristics of a STED microscope.

# 4 Setup and Methods

> Mikroskope und Fernröhre verwirren
> eigentlich den reinen Menschensinn.
>
> *"Wilhelm Meisters Wanderjahre"*
> Johann Wolfgang von Goethe (1821)

As shown in Chapter 2, existing approaches in 3D fluorescence single particle tracking microscopy (SPTM) generally fall into two categories: post-processing of camera-based image sequences, and live-feedback systems. Our instrument follows a hybrid approach, integrating an electron-multiplying CCD (EM-CCD) camera with a feedback-based tracking scheme.

This chapter provides an overview of the optical setup, details the design rationale and integration of beam-steering and readout technologies, and describes the feedback-driven operation of the system. The custom software package for instrument control, calibration, and data analysis is presented in Appendix A.

## 4.1 Optical Setup

The optical setup is shown schematically in Figure 4.1. It is is based on a commercial inverted microscope stand (DM-IRBE, Leica Microsystems) equipped with a 63×/1.2 NA water immersion plan apochromat objective (Leica). The objective has a correction collar to account for spherical aberrations due to variation in cover slip thickness. The microscope stage (a standard manual three-plate stage) can be fitted with a temperature-regulated heated stage insert (TC-202A, Harvard Apparatus) for in-vivo measurements at physiological temperatures.

The microscope stand and all external components are mounted on a vibration-damped optical breadboard table (System 1, TMC Vibration Control). Additional attenuation of external vibrations is provided by placing the table on an isolated section of the floor of our microscope room, consisting of a concrete block decoupled from the building by means of a pneumatic damping system. A project enclosure built from black PVC boards protects the external beampath from stray light, air flow, and dust. Figure 4.2 shows a picture of the setup.

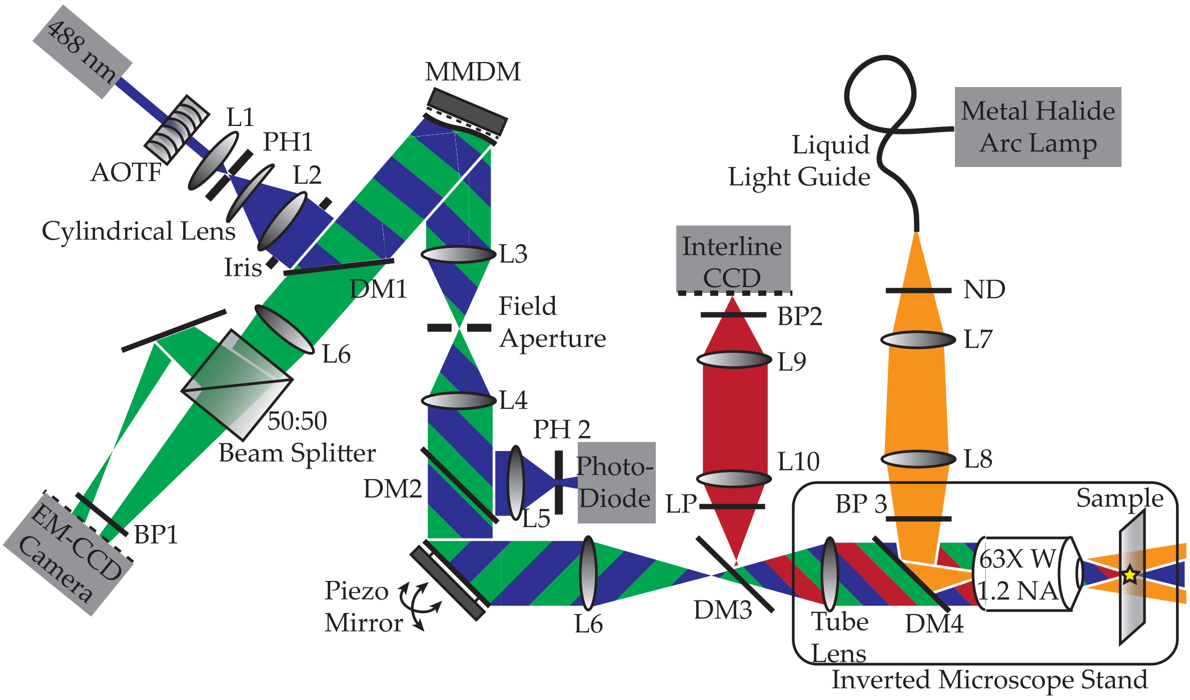
488 nm
AOTF
L1
PH1
L2
Cylindrical Lens
Iris
MMDM
DM1
L3
Field
Aperture
L6
50:50
Beam Splitter
L4
PH 2
Photo-
Diode
L5
DM2
BP1
EM-CCD
Camera
Piezo
Mirror
L6
DM3
Liquid
Light Guide
Metal Halide
Arc Lamp
Interline
CCD
BP2
L9
L10
LP
ND
L7
L8
BP 3
Sample
63X W
1.2 NA
Tube
Lens
DM4
Inverted Microscope Stand

Figure 4.1: Optical setup. L1–L11: lenses. PH1 and PH2: pinholes. DM1–DM4: Dichroic mirrors. AOTF: acousto-optical tunable filter. MMDM: micromachined membrane deformable mirror. ND: neutral density filter. LP: longpass filter. Color code of the beampath: blue – tracking excitation laser; green – tracking fluorescence; orange – overview excitation lamp; red – overview fluorescence.

Fluorescence excitation is provided by an optically pumped semiconductor laser emitting up to 50 mW at 488 nm (Sapphire 488 LP50, Coherent). An acousto-optic tunable filter (AOTFnC-400.650-TN, AA Opto-Electronic) is used to switch the laser, regulate its intensity, and synchronize laser irradiation with camera exposure times (eliminating unnecessary photobleaching and photodamage to the sample during readout dead times). The laser light is then focused by an $f = 30$ mm lens[1] (L1) onto a 30 µm pinhole (PH1) and recollimated by an $f = 400$ mm lens (L2).

An adjustable iris aperture close to L2 provides the option to clip the beam to a narrow circle for alignment purposes. An f=1000 mm cylindrical singlet lens, mounted in a holder that can be rotated around the optical axis, is positioned between PH1 and L2 to pre-compensate for astigmatism introduced by the dichroic mirror[2] DM1 (FF502/670-Di02, Semrock), which reflects the laser beam into the scanning/descanning beampath.

The scanning/descanning beampath contains the MMDM (15 mm 37-ch “OKO

---

[1] Except where otherwise noted, all lenses in the external beampath are one-inch diameter achromatic doublets (AC254 Series, Thorlabs) with anti-reflective coating for visible wavelengths.

[2] for transmission characteristics of dichroics and other optical components, see Appendix B

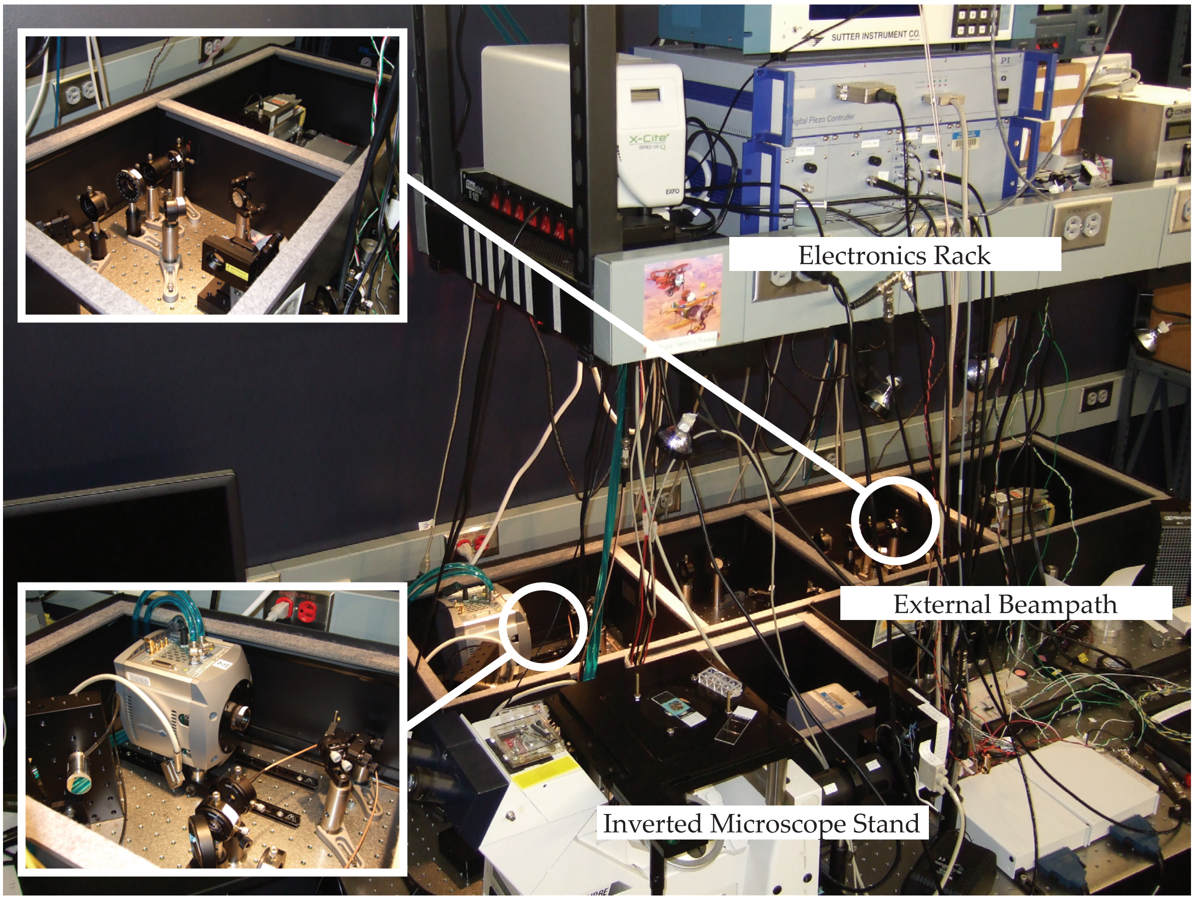

Figure 4.2: Picture of the single particle tracking setup with insets highlighting details of the excitation (upper left) and detection (lower left) beam path.

Mirror”, OKO Flexible Optical) and the piezo mirror (S-330.2SL, Physik Instrumente), providing axial and lateral movement of the laser focus, respectively. The micro-machined membrane deformable mirror (MMDM) and piezo mirror are positioned in two conjugate planes of the objective pupil, created by lenses L3, L4, and L6 (all $f = 200$ mm) in conjunction with the 1× tube lens of the microscope stand (nominal focal length $f = 200$ mm). This configuration ensures that the introduced phase modifications are imaged accurately into the back aperture of the objective. A custom-made rectangular field aperture between L3 and L4 (in a conjugate image plane) provides additional background suppression and facilitates viewing of the sample in widefield fluorescence mode.

Part of the laser light is redirected by a dichroic mirror (DM2; Di01-R488/561, Semrock) towards lens L5 ($f = 40$ mm), which focuses it slightly in front of a pinhole (PH 2) placed in front of a Silicon photodiode (SM05PD2A, Thorlabs), generating a signal to measure the amount of defocus introduced by the MMDM.

Beyond the scanning/descanning beampath, the laser beam is coupled into the sideport of the microscope stand and focused into the sample by the tube lens and the objective. Fluorescence light is collected by the same objective, passes through the tube lens and the scanning/descanning beampath, and is transmitted through the dichroic mirror DM1, which separates it from the excitation light.

An $f = 500$ mm lens (L6) images the observed sample area onto the sensor of a back-thinned, water-cooled EM-CCD camera (Ixon DU-860, Andor Technology) with 128 × 128 pixels at a total lateral magnification of 157.5× (effective pixel size: 152 nm). A bandpass filter (BP1; FF01-525/45, Semrock) filters out background light. Between L6 and the EM-CCD chip, the lightpath is split into two branches by a 50:50 non-polarizing beamsplitter cube. The transmitted light reaches the chip directly, while the slightly longer reflected branch is redirected onto a separate area of the chip by a dielectric mirror. Due to the path length difference, the two images on the chip correspond to two sample planes with an axial separation of about 500–800 nm. The plane separation can be adjusted by varying the distance between the beamsplitter cube and the redirecting mirror, taking into account that the total axial magnification is approximately the square of the lateral magnification, i.e. ~25,000×.

As an alternative to the MMDM, the objective is mounted on a piezo-driven axial translation unit (PIFOC P-726, Physik Instrumente). A comparison of the two options for axial focus steering is shown in Section 4.2. The microscope's sample stage can optionally be equipped with a three-axis piezo translation stage (P-733.3DD, Physik Instrumente); this can be used as a calibration and characterization tool by programming defined trajectories into the stage controller.

In addition to the tracking channel, which is optimized for EGFP, Alexa 488, and spectrally similar fluorophores, the instrument has a conventional widefield fluorescence channel to provide structural overview in a second color using red-emitting fluorophores like mCherry, Cy5, etc.

A metal halide arc lamp (X-Cite 120Q, Lumen Dynamics) is coupled into the back port of the microscope stand via a liquid light guide and two two-inch diameter singlet lenses L7 ($f = 100$ mm) and L8 ($f = 300$ mm). A shuttered filter wheel (Lambda 10-2, Sutter Instruments) containing multiple neutral density (ND) filters serves to switch the light and select the excitation intensity. A bandpass filter (BP2; FF01-567/15, Semrock) selects the desired excitation wavelength range. The light from the lamp is reflected towards the objective by a dichroic mirror (DM3; FF576/661-Di01, Semrock), the exit pupil of the liquid light guide being imaged into the back aperture of the objective to achieve widefield illumination in the sample.

Red fluorescence is collected by the objective, transmitted through DM3 and the tube lens, and separated from the green fluorescence of the tracking channel by a shortpass dichroic mirror (DM4; FF541-SDi01, Semrock). A longpass filter (LP; BLP01-488R, Semrock) removes reflected laser light before a lens pair (L9, L10; both $f = 100$ mm) creates an image of the sample on the sensor of an Interline CCD camera (Clara DR-328G, Andor Technology) with a total magnification of 63. The effective pixel size is 102 nm. Background light is suppressed by a bandpass filter (BP3; FF01-615/45, Semrock). Commercial filtercubes for green-fluorescent protein (GFP) and mCherry (Semrock) in combination with the arc lamp allow observation of the two channels through the eyepieces of the microscope to identify regions of interest (ROIs).

Instrument control, data acquisition, and data analysis are performed on a high-performance PC workstation (Precision T7500, Dell) running Microsoft Windows XP. The control and acquisition software suite "Aerobatics" was developed in Labview (versions 8.6 and 11, National Instruments). Communication with the devices on the optical table is established via a PCI Express input/output interface card (PCIe-6323, National Instruments), a proprietary PCI interface card for the EM-CCD camera, and various RS-232 and USB connections.

## 4.2 Beam Steering

In our feedback-based tracking method, fast laser beam steering and fluorescence descanning in both the axial and lateral direction is necessary to keep the particle in focus throughout the measurement. Stage-scanning, e.g. by using a three-axis piezo stage, was ruled out because of insufficient response bandwidths and concerns about artificially influencing dynamics by vibrating the sample. We surveyed various technologies for the purpose of beam steering.

Non-resonant galvanometer mirrors are frequently used for lateral beam steering in laser scanning microscopes (Pawley, 2006) and achieve sinusoidal scanning at several kilohertz. Random access time, the more relevant figure for our purpose, is typically on the order of 200–300 µs.

This is comparable to the fastest piezo tip/tilt systems. These have the advantage that integrated two-axis systems with a single mirror are available, which avoids having to place two galvanometer mirrors either in two telecentric planes or suboptimally positioning both mirrors in the proximity of only one such plane. Both types of mirrors are usually equipped with accurate position sensors, allowing for either closed-loop operation or precise monitoring of the current position in open-loop configuration.

Acousto-optic deflectors (AODs) have been used as beam-steering devices in two-photon microscopy for extremely fast (about 10 µs step response) random-access scanning in one (Lechleiter et al., 2002) or two (Salomé et al., 2006) dimensions. Even 3D scanning using an arrangement of custom-made AODs has recently been demonstrated (Kirkby et al., 2010). However, this is not practical when descanning of detected fluorescence is required. While the polarization dependence and strong chromatic dispersion of AOD crystals can be compensated by suitable arrangements of multiple crystals, their narrow transmission bandwidth would still reject too much fluorescence light.

For axial scanning, the most common method (after stage scanning) is the use of a linear translation stage for the microscope objective, which can be actuated by a galvanometer, stepper motors, or piezos. Piezo solutions have typical step response bandwidths up to 200 Hz.

To avoid movement of the objective, remote focusing, i.e. introduction of beam divergence or convergence in a different part of the beampath can be used. A simple way to achieve this is the use of an electrically tunable lens (Blum et al., 2011). This is essentially a liquid filled container bounded by polymer membranes; adjusting the fluid pressure rapidly alters the membrane curvature and thus the focal length of the lens. Step response settling times of the fastest available lenses are around 10 ms.

A faster way to do remote focusing makes use of a second objective lens, placed in the excitation beampath to generate an intermediate image plane. A small mirror mounted on an axial piezo translation stage can then be used for defocusing at several kilohertz (Botcherby et al., 2008). However, this geometry requires a beamsplitter near the back aperture of the second objective. For descanning of fluorescence emission, this means that at least 75 % of the light would be lost at the beam splitter (which is passed twice) .

Due to these considerations, we initially built our setup using a two-axis piezo mirror for lateral scanning and a linear piezo translation stage for axial objective movement. In a later stage we integrated a deformable mirror for axial scanning to replace the piezo translation stage.

### 4.2.1 Performance of Piezo Positioners

To characterize the response of our piezos, step functions with small amplitudes were generated on an analog output of the IO interface card. Simultaneously, the signal from the piezos' internal sensors was recorded using an analog input of the card and the software SignalExpress (National Instruments). Determination of the rise time from 10 to 90 % of the total amplitude yielded (284 ± 5) µs for the tip/tilt mirror (S-330.2SL with strain gauge sensor, Physik Instrumente) and (1511 ± 73) µs for the objective piezo (PI-FOC P-726.1CD with capacitive sensor, Physik Instrumente). The response curves are shown in Figure 4.3. The laterally elongated shape of the PSF compensates for a slower axial response only up to a factor of about three.

### 4.2.2 Integration of a Micromachined Membrane Deformable Mirror

In addition to the 5-fold slower axial versus lateral piezo performance, there is a possibility that vibrations of the objective piezo are coupled into the sample through the immersion medium. Both factors can be eliminated by fast remote focusing. It has previously been shown (Zhu, Sun, and Fainman, 1999) that an MMDM can be used to generate spherical wavefronts with kilohertz response frequencies. The step

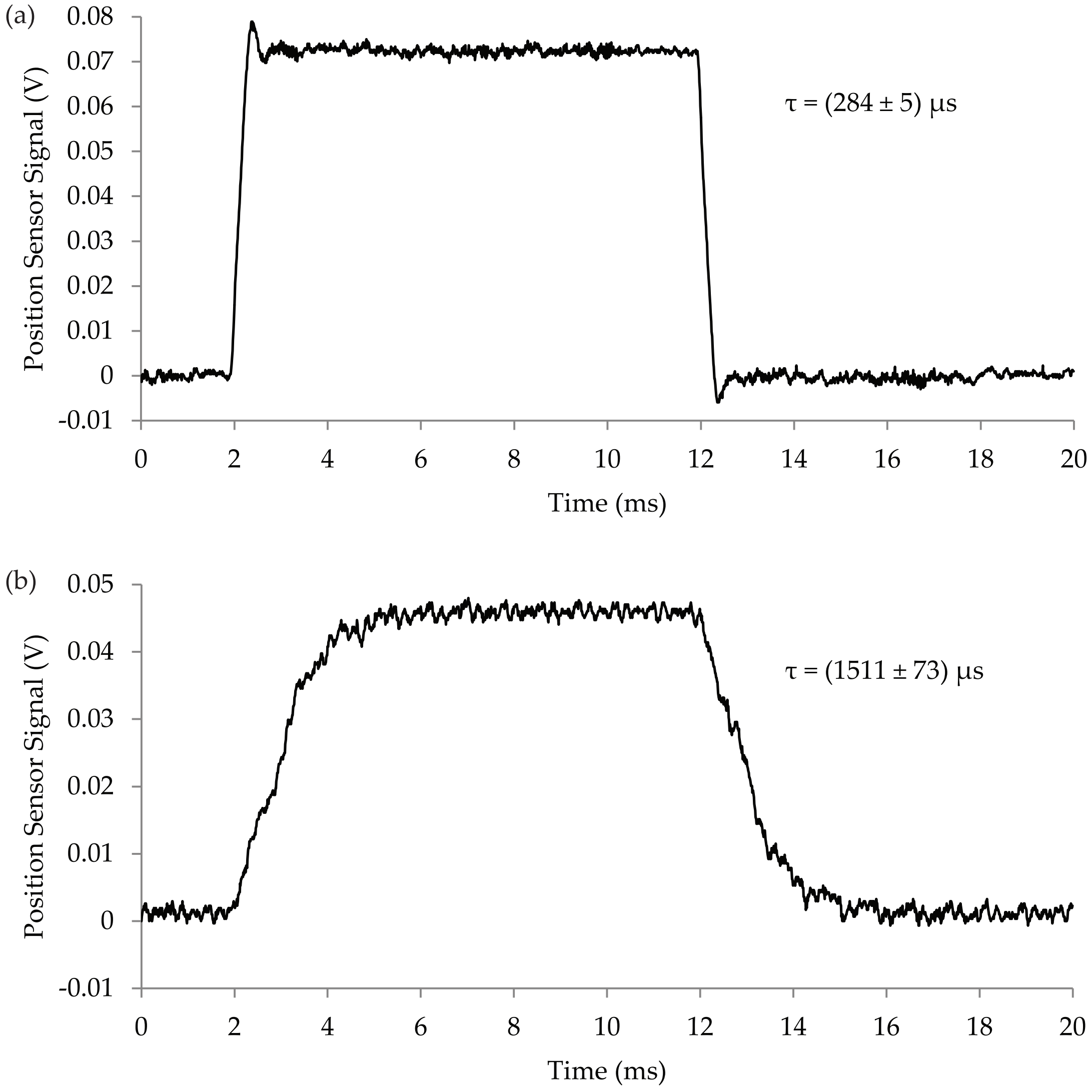

Figure 4.3: Step response of piezo positioners as measured by the piezo actuators' internal strain-gauge sensors. (a) Tip/tilt mirror for lateral beam steering. (b) Linear translation stage for objective movement. $\tau$ denotes the rise time from 10 to 90 percent of the total amplitude.

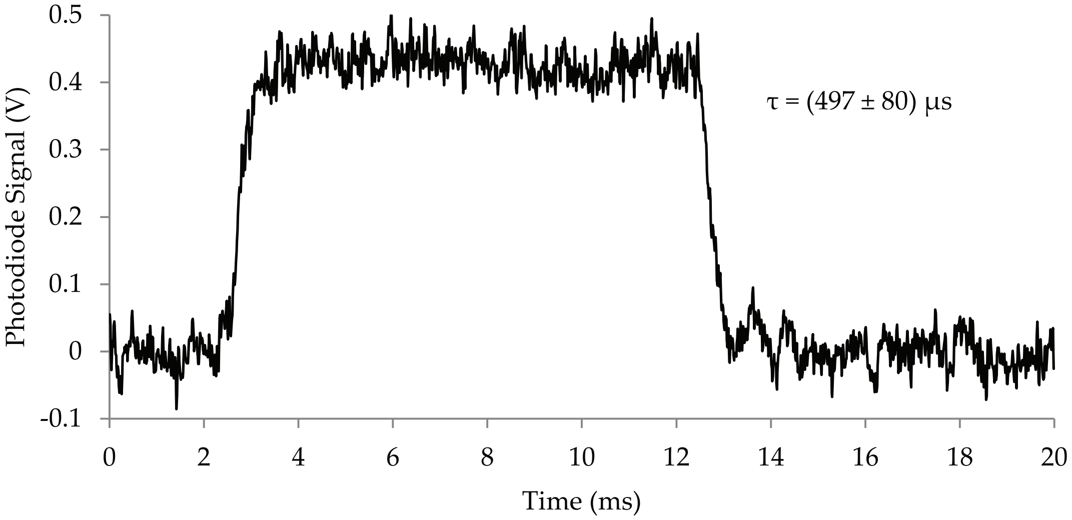

Figure 4.4: Step response of the deformable mirror. A signal proportional to the focal displacement was generated by focusing the reflected laser beam slightly in front of a silicon photodiode and identifying a linear region of the resulting calibration curve. $\tau$ denotes the rise time from 10 to 90 percent of the total amplitude.

response of our MMDM was measured by generating a step function defocus signal and monitoring the focal position (via the photodiode signal) using SignalExpress. The resulting curve is shown in Figure 4.4. With a rise time of (497 ± 80) µs, it is three times faster than the objective piezo and therefore not expected to be performance-limiting like the piezo.

Vdovin (1998) showed that, in principle, the mirror can also be used for lateral beam-steering by introducing tilt modes. However, I previously found that due to the fixed membrane edge, the tilt range over which an acceptable wavefront quality can be achieved is only 1 µm in each direction and further reduced by simultaneous defocus (Juette, 2009). We therefore restrict the MMDM to axial focus steering, where it achieves an effective range of about ±3.5 µm (see Section 5.1.1).

The noise visible in Figure 4.4 is mainly due to the photodiode circuit. It can be reduced by using a higher resistance in the RC filter, but this increases the signal rise time (about 130 µs as shown). It is shown in Section 5.2 that this noise does not contribute significantly to the overall localization precision.

## 4.3 Read Out of the Fluorescence Signal

For fluorescence detection, previous feedback-based tracking methods have generally relied on point detectors like avalanche photodiodes (APDs) or photo-multiplier tubes (PMTs). As discussed in Chapter 2, this has been implemented by either scanning the detection volume in circular orbits around the particle of interest (Katayama et al., 2009; Levi et al., 2005; McHale et al., 2007) or by using a tetrahedral arrangement of fiber tips (Lessard et al., 2007).

Both methods have the disadvantage that they detect fluorescence only from peripheral regions of the intensity distribution, resulting in a reduced detection efficiency. To compensate, the laser intensity has to be increased, resulting in accelerated photobleaching.

We avoid this problem by using the nearly continuous detection area of a back-thinned EM-CCD chip. EM-CCD cameras have improved sensitivity compared to conventional charge-coupled devices (CCDs), using a pre-amplification register that multiplies the originally collected charge by impact ionization. Quantum efficiencies in the visible spectrum exceed 90 %. However, this value is effectively reduced by half due to the additional Poisson-like noise inherent to the electron multiplication process. The resulting quantum efficiency is still only about 25 % smaller than that of APDs and exceeds PMTs by a factor of about three (Pawley, 2006). An additional advantage is that, unlike APDs, an EM-CCD chip with sufficiently low exposure times does not easily saturate at high light levels.

Achievable frame rates depend on the specific experimental configuration. Point detectors allow for a high pixel readout frequency, given sufficient fluorescence signal is available. In the tetrahedral detection scheme and for similar methods with pixel-parallel readout, this easily allows for submillisecond readout rates (Cang et al., 2007). Orbital tracking, on the other hand, requires scanning and therefore has typical time resolutions of at least several milliseconds (Dupont and Lamb, 2011), comparable to the full-frame readout time of an EM-CCD camera.

However, our descanned Biplane detection requires readout of only five lines. Using the fastest detection mode on the fastest EM-CCD camera available, this allows for frame rates of up to 7.6 kHz[3] (130 µs temporal resolution).

## 4.4 Position Estimation

Our feedback-based particle tracking method requires fast on-the-fly estimation of the particle position in each retrieved camera frame. At frame rates in the kilohertz range, full iterative fitting of the three-dimensional intensity distribution (Mlodzianoski et al., 2009) is prohibitively expensive.

---

[3] The fastest possible readout is achieved by combining two EM-CCD options: (i) Frame-transfer mode shifts the entire frame into an adjacent region of the chip, from which it is then read out while the next frame is already acquired. This allows typical duty cycles of nearly 100 percent (reduced to about 90 percent at 3.2 kHz frame rate). (ii) The isolated crop mode avoids discarding the charge outside the set ROI, making the sensor behave like a smaller one, resulting in an additional increase in frame rate. To use this mode, light must be prevented from falling onto the unused sensor region by using a field aperture.

Simple position estimation by subtracting pixels along each direction (e.g. subtracting the summed upper and lower planes for an axial estimate) could potentially be used; however, this position measure is proportional to the emitted fluorescence intensity, making it impossible to correctly tune the feedback loop when particles of varying brightness or photobleaching are expected.

I devised a simple position estimator that is fast enough for submillisecond operation, shows an approximately linear response to the particle position, and is nearly independent of particle brightness. It is based on the frequently made assumption (R. E. Thompson et al., 2002) that the central lobe of the PSF is reasonably well approximated by a 3D Gaussian.

Consider two finite thin cross-sections through the PSF, which are perpendicular to the $u$ direction ($u = x, y, z$) and separated by $\Delta u$. Since a 3D Gaussian is separable in its coordinates, the integrated intensity in each section is approximated by

$$I\left(u \pm \frac{1}{2}\Delta u\right) = I(0) \exp\left[-\frac{1}{2}\left(\frac{u \pm \frac{1}{2}\Delta u}{\sigma_u}\right)^2\right], \tag{4.1}$$

where $\sigma_u$ is the standard deviation of the PSF along the $u$ direction. An intensity-independent linear function $E(u)$ is then defined by

$$E(u) = \ln \frac{I\left(u - \frac{1}{2}\Delta u\right)}{I\left(u + \frac{1}{2}\Delta u\right)} = \frac{\Delta u}{\sigma_u^2} u. \tag{4.2}$$

To verify the brightness independence of the position estimator and determine the proportionality constant $m = \frac{\Delta u}{\sigma_u^2}$, the displacement estimator is calculated and plotted for a fluorescent bead imaged at different known positions, as shown in Figure 4.5. The resulting curves confirm that the brightness of the bead (regulated by varying the excitation laser intensity) has only a minor influence on the displacement estimator. The calibration factor, given by the slope of the linear region of the curves, changed by less than 4% when the brightness of the bead was nearly doubled. For the PSF of our setup, the linearity range of the displacement estimator was found to be more than ±150 nm laterally and about ±600 nm in the axial direction.

## 4.5 Feedback Operation

The operational centerpiece of the Biplane SPTM is the feedback loop driving the beam-steering hardware in response to the detected particle displacement. While the basic principle is straightforward—read camera frame, estimate particle position, recenter laser focus on determined position—the high temporal resolution of the system requires a careful design of the loop. To minimize latencies and jitter, we

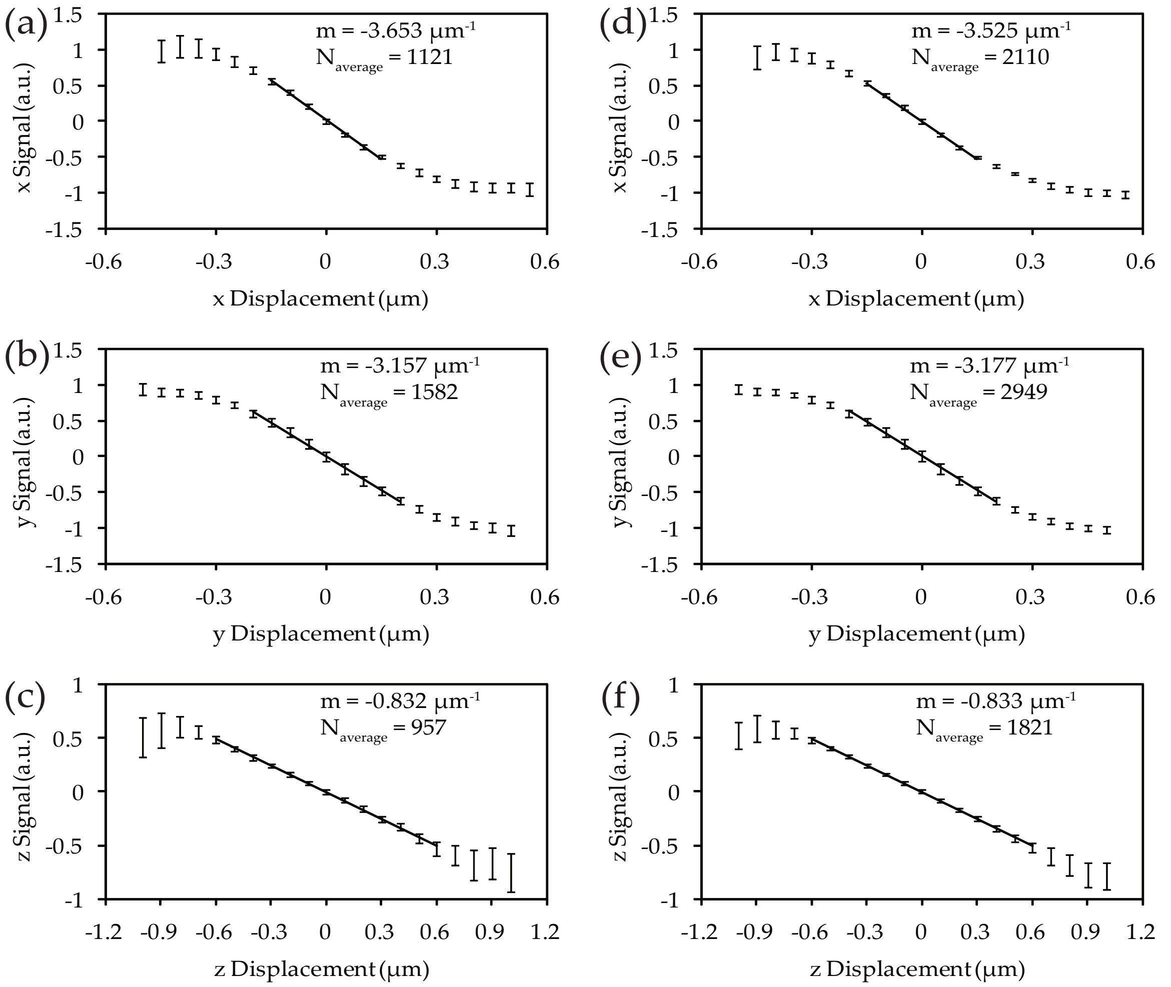

Figure 4.5: The reduced Gaussian position estimator as a function of position. A 200 nm fluorescent bead (F-8774, FluoSpheres 505/515, Invitrogen) attached to a coverslip was imaged at different positions of the piezo translation stage. The responses to translations along the x, y and z directions were measured separately. The measurement sequence was performed for two different laser intensities (subfigures a–c and d–f, respectively). At each position, 50 frames were acquired in biplane mode with 1 ms exposure time. After background subtraction, two regions of interest 5 × 5 pixels in size were extracted from each frame. The displacement estimator was then calculated for each frame using Equation 4.2 and averaged over the 50 frames for each position. The error bars in the plots show the interval of plus and minus one standard deviation. Linear least-squares fits were performed over the respective linear regions of the data as indicated by the black lines. The determined slope $m$ and the average number of detected photons per frame, $N_{\text{average}}$, are shown in the top right of each diagram. Adapted from Juette and Bewersdorf (2010), Supplements.

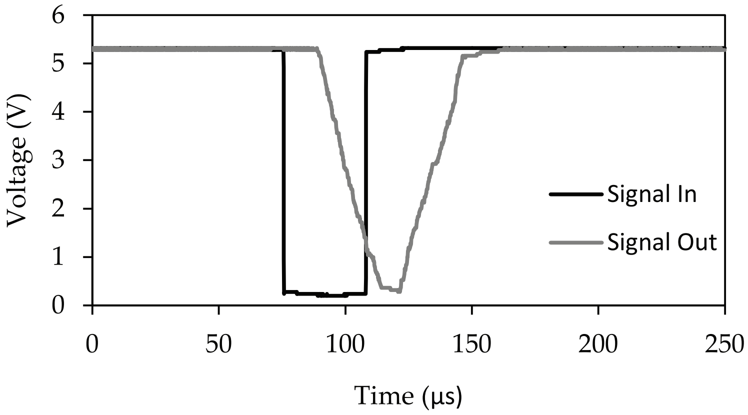

Figure 4.6: Input-output latency of the PC workstation using the PCIe IO interface card and LabView software. The trigger output of the EM-CCD camera is used as a reference signal. Upon detection of a signal change at the IO card's digital input, a loop implemented in LabView generates a signal flip, which is then sent to a digital output channel on a separate chipset on the IO card (to prevent internal routing). The signal delay is displayed on a digital oscilloscope, averaged over 128 signal periods to estimate the jitter.

initially considered a field-programmable gate array (FPGA) based architecture of the feedback system.

This, however, requires an exact knowledge of the EM-CCD camera's communication protocol, which was not available from the manufacturer. A measurement of the input-output latency of the PC workstation (Figure 4.6) used for instrument control indicated that sub-millisecond operation without dedicated feedback electronics was feasible.

Due to the different temporal responses of various hardware components, the feedback procedure was subdivided into several independently running loops as shown in Figure 4.7. The primary loop, or timing loop, is a hardware-synchronized software loop based on the falling flank of the camera's trigger output, which is connected to a digital input of the IO interface card. This indicates the end of a frame exposure. The timing loop performs the two operations with negligible temporal footprint: (i) acquisition of the position sensor signals for the piezo positioners and the MMDM; (ii) notification of the secondary loop that a new frame is available. This loop executes with high predictability and minimal latency up to the maximum camera frame rate of 7.6 kHz.

The secondary loop is responsible for retrieving the most current frame from the camera's internal frame buffer. Due to communication and data transfer rates, this step is limited to approximately 1 kHz repetition rate. This implies that at time resolutions below 1 ms, not every camera frame contributes to the feedback

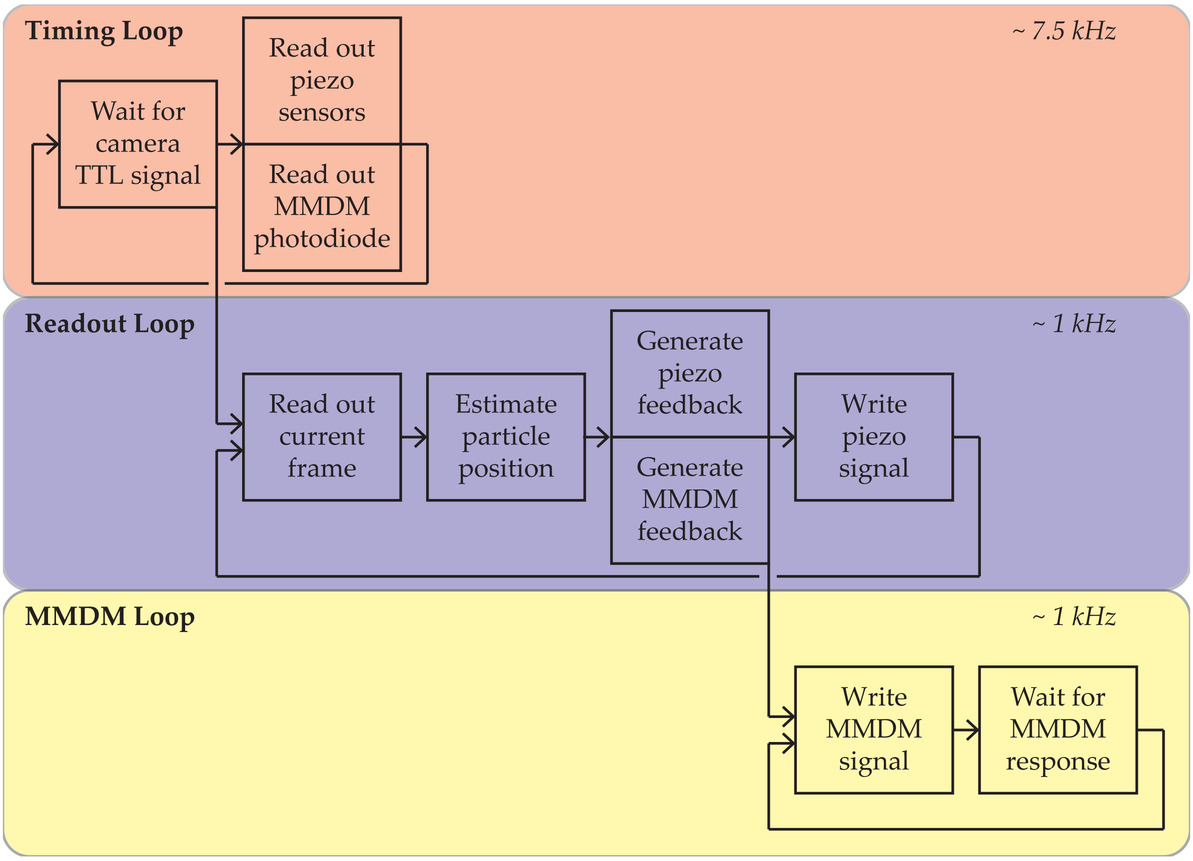
Timing Loop
~ 7.5 kHz
Wait for camera TTL signal
Read out piezo sensors
Read out MMDM photodiode
Readout Loop
~ 1 kHz
Read out current frame
Estimate particle position
Generate piezo feedback
Generate MMDM feedback
Write piezo signal
MMDM Loop
~ 1 kHz
Write MMDM signal
Wait for MMDM response

Figure 4.7: Schematic of feedback operation. The procedure is split between three asynchronous parallel loops responsible for (i) synchronization with the camera frame and readout of the focus position; (ii) retrieval of the current frame, generation of the feedback signal, and communication with the piezos; (iii) communication with the deformable mirror.

signal. Notifications from the timing loop are ignored while the readout loop is busy. However, the full position information is preserved, as the entire measurement series is stored in the frame buffer (up to 40,000 frames) and saved to disk at the end of the experiment. The particle position in all "missing" frames is then estimated and combined with the information about the position of the beam-steering system in each frame, as recorded by the timing loop. Temporal resolution is therefore limited by the camera frame rate, not by the camera readout frequency or the mechanical response of the steering system (as long as the particle does not escape the field of view between frames retrieved in real time).

Estimation of the particle position and calculation of the feedback signal is performed as soon as the camera frame has been written into PC memory. Using the computationally inexpensive reduced Gaussian position estimator described above, this does not add significant temporal overhead to the readout loop; neither does writing the new piezo position signal to the analog outputs of the IO card.

Sending the new voltage array to the MMDM requires a dedicated loop because the mirror driver unit only accepts a new command after a termination signal has been received by the PC. This is internally limited to 1 kHz repetition frequency. The MMDM loop is notified by the readout loop whenever new position data is available. It runs at nearly 1 kHz repetition frequency, asynchronously parallel with the readout loop.

The feedback signal itself is generated by multiplication of the detected displacement with a constant gain factor, i.e. the feedback system is purely proportional. Integral and derivative terms were initially used, but proved to be of no noticeable practical use and were left out of later versions of the control software. The proportional gain is tuned by a simple standard procedure (Hagglund, 1995). A fixed bead is tracked at a similar SNR as expected in the experiment. The gain for one axis at a time is gradually increased until the system shows oscillatory behavior. The gain is then decreased to about 50–70% of the “tipping point”.

# 5 Experiments and Results

> When you employ the microscope, shake off
> all prejudice, nor harbor any favorite opinions;
> for, if you do, ’tis not unlikely fancy will
> betray you into error, and make you see what
> you wish to see.
>
> *The Microscope Made Easy*
> Henry Baker (1742)

## 5.1 Instrument Calibration

The function of the single particle tracking microscope (SPTM) and the acquisition of reliable quantitative data require precise calibration of the instrument. This includes the optimization of the micro-machined membrane deformable mirror (MMDM) surface shape, calibration of positioning and camera parameters, and careful alignment of the beampath.

### 5.1.1 Deformable Mirror Optimization

The wavefront generated in the objective pupil by a voltage pattern applied to the MMDM is a function both of the mirror itself and of the specific experimental geometry (incidence angle, centering precision, and relay optics). In addition, the voltage response in membrane deformation is strongly coupled between individual electrodes. It is therefore necessary to implement a protocol for finding the optimal control voltages corresponding to a desired wavefront. The fast operation of the single particle tracking (SPT) feedback loop is enabled by the generation of a lookup table ahead of time, from which the required voltages can be found by interpolation.

#### Zernike Mode Optimization

I previously (Juette, 2009) compared the convergence speed and achieved wavefront quality of several iterative algorithms to optimize the surface shape of a deformable mirror. The comparison included steepest descent (Press et al., 2007), random search (Wright et al., 2005), and genetic algorithms (Albert et al., 2000). Feedback from a SHWS (WFS150, Thorlabs) was used for all methods; the root mean square (RMS) deviation of the current wavefront from the optimization target was the figure of merit. The Shack-Hartmann wavefront sensor (SHWS) was mounted in a lens tube system containing a $4f$ arrangement of achromatic lenses to image the objective pupil plane onto the sensor with appropriate magnification.

In that comparison, the best RMS deviation figures were achieved with a steepest descent algorithm using prior knowledge, developed by Zhu, Sun, Bartsch, et al. (1999). The prior knowledge is implemented by measuring the influence matrix $(b_{kl})$ of the deformable mirror. This characterizes the mirror response to each electrode in terms of Zernike coefficients. More precisely, it relates the coefficient $a_k$ of the $k$-th Zernike mode to the voltage $V_l$ applied to the $l$-th mirror channel:

$$a_k = b_{kl} V_l^2. \tag{5.1}$$

The coefficients' square dependence on the applied voltage was described theoretically by Vdovin (1998) and experimentally confirmed for our mirror (Juette, 2009). The influence matrix can therefore be obtained by applying a series of increasing voltages to each electrode separately, measuring the wavefront with the SHWS and fitting a straight line to the individual $a_k$ as a function of the control signal $c_l = V_l^2$.

The algorithm by Zhu, Sun, Bartsch, et al. (1999) uses the iteration formula

$$c_l' = c_l - \mu \sum_{k=1}^{K} \frac{1}{N_k} b_{kl} \left( a_k - a_k^{(T)} \right), \tag{5.2}$$

where $\mu$ is an experimentally determined convergence factor and $a_k^{(T)}$ the target coefficient for the $k$-th Zernike mode. This iteration formula was shown to take steps along the direction of steepest descent for the RMS wavefront deviation.

### Correction for Spherical Aberrations

As shown in Chapter 3.4, generation of pure defocus modes in the pupil plane does not correspond to pure defocus in the sample or image plane. However, it is possible to correct for this by including the appropriate spherical aberration terms in the optimization target.

To verify this, I used the steepest descent algorithm to generate a two-dimensional lookup table of voltage arrays for varying amounts of defocus and fourth-order spherical aberration (other spherical modes were excluded due to the limited higher-order performance of the deformable mirror). PSFs were then recorded for thirteen focal positions and nine different spherical aberration coefficients. All measurements were performed by scanning the same 200 nm fluorescent bead in steps along the z direction. A very low laser power (less than 1 µW in the back focal plane) was chosen

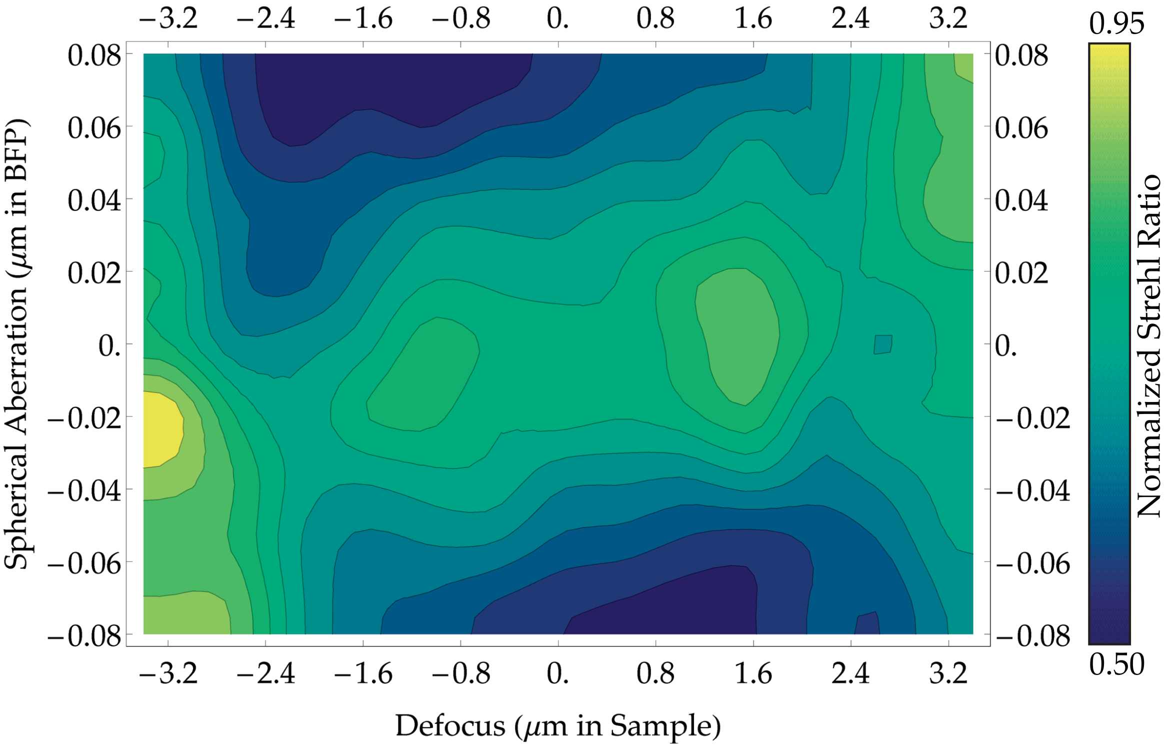

Figure 5.1: Map of normalized Strehl ratio, obtained by recording 117 point-spread functions for different deformable mirror settings as described in the text. The diagonally oriented plateau shows that a spherical aberration term proportional to the applied defocus corrects well for defocus-induced aberrations.

to virtually eliminate photobleaching and make intensity values comparable. For each z position, 20 frames were averaged. All PSFs were normalized to the maximum intensity across all measurements, and the rescaled maximum intensity for each PSF was extracted.

This value is proportional to the Strehl ratio, a common descriptor of the optical performance of a system. According to the Maréchal criterion, a system has diffraction-limited performance for Strehl ratios above 0.8, corresponding to a RMS wavefront error of less than $\lambda/14$ (Born and Wolf, 1999). Note that, while the optimized MMDM shape leads to a well-corrected PSF in the center of the deflection range, suggesting nearly diffraction-limited performance, the actual Strehl ratio is not known, as this would require knowledge of the maximum achievable peak intensity.

The obtained map of normalized Strehl ratios is shown in Figure 5.1. The diagonally oriented plateau confirms that a fourth order spherical term proportional to the amount of applied defocus provides good compensation of the high-NA defocus-induced aberration. Figure 5.2 shows a side-by-side comparison of PSFs at maximum positive defocus with and without pre-correction of spherical aberration.

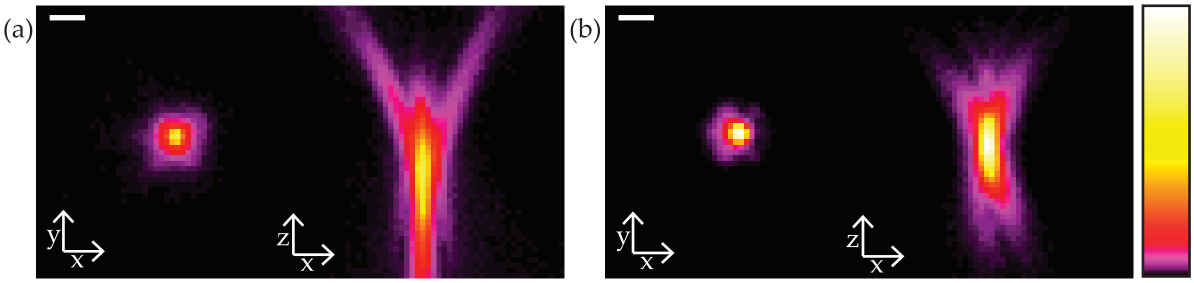

Figure 5.2: Point-spread functions with “naive” defocus of +3.2 µm (a) and after precompensation of fourth-order spherical aberration (b). Scale bars: 1 µm.

### 5.1.2 Beampath Alignment

Three aspects of beampath alignment are particularly critical for the performance of the microscope:

1. precise centering of both excitation and fluorescence light on the electrode pattern of the MMDM,
2. conjugation of the piezo mirror and the MMDM to the objective pupil plane,
3. precompensation of astigmatism introduced by the dichroic mirror used to couple in the laser beam.

I devised specific alignment procedures to reliably fulfill each of these conditions.

*Condition 1*—If this is not met, the optical performance of the MMDM is compromised. Firstly, if the electrode pattern is off-center, generation of Zernike modes is severely limited. Secondly, a misalignment of excitation and fluorescence leads to a different effect of the mirror in both beam paths, resulting in an inferior effective PSF.

To facilitate coalignment, a collimated 635 nm laser diode (CPS180, Thorlabs) was mounted in a two-axis tiltable holder that can be attached to the microscope’s objective turret (when the objective is removed). An adjustable iris in the mount allows for cropping of the alignment beam, while the excitation laser beam can be cropped by the iris aperture near lens L2 (see Figure 4.1). Iterative beam walks can then be performed to coalign both laser beams.

The alignment of both beams with the MMDM electrode pattern can be verified by applying maximum voltage to all electrodes. Print-through of the electrodes is then visible in planes near L4 and L5.

*Condition 2*—If the piezo mirror and the MMDM are not placed in conjugate planes of the objective pupil plane, their tilt and defocus will lead to underfilling of the pupil, which in turn leads to a decrease in excitation intensity for off-center focal positions. Correct placement can be verified by removing the objective and adding a fluorescent screen in the known position of the (virtual) pupil plane. The laser spot observed on the screen should not change its size or position when introducing tilt or defocus in the correct conjugate plane.

*Condition 3*—Due to the hard-coating process used by the manufacturer, all dichroic mirrors in the setup exhibit a certain degree of cylindrical distortion. This introduces astigmatism only in the reflected light path and is often not problematic, as the fluorescence is usually transmitted through the dichroic. However, without correction, the deformable mirror optimization routine will compensate for the astigmatism in the excitation, thereby introducing astigmatism in the descanned fluorescence.

To prevent this, a weak cylindrical lens fixed in a rotating mount is placed behind the pinhole in the excitation beampath. A shearing interferometer (Riley and Gusinow, 1977) placed behind the deformable mirror can then be used to monitor perpendicular astigmatism components and find the correct orientation and position of the cylindrical lens.

### 5.1.3 Positioning Calibration

Calibration of the position measurements involves three steps. In the first step, the piezo mirror position (i.e. angle) signal is calibrated with respect to displacement in the sample. This is done by imaging a bright fluorescent bead with widefield illumination and moving the piezo mirror to its four "corner" positions in between frames. 2D Gaussians are fitted to the images of the bead to determine the exact position differences generated by moving the mirror. A voltage-to-position conversion factor is then calculated.

Step two is the calibration measurement for the reduced Gaussian displacement estimator, as described in Section 4.4. Note that this step is not required for feedback operation, as the slope of the estimator calibration curve is "absorbed" into the tuning of the feedback gain. However, the estimator can be used for accurate position determination in post-processing, as long as the particle stays within the monotonicity range (see Figure 4.5) of the estimator. Alternatively, a full three-dimensional fit of the acquired data to an experimental PSF can be used for this purpose (Mlodzianoski et al., 2009).

The final step is only relevant when the deformable mirror is used for axial tracking. In this step, a calibration curve of the photodiode signal as a function of defocus is recorded. The alignment of the pinhole P2 and lens L5 (Figure 4.1) in front of the photodiode may need to be adjusted to achieve a linear signal.

### 5.1.4 Photon Count Calibration

Quantitative assessment of the instrument's localization precision as a function of detected photons (see 5.2.2) requires knowledge of the photon-to-count conversion factor $a$ of the EM-CCD camera. Assuming a linear photon-count dependence of the camera signal $S$ (i.e. $S = aN + b$, where $N$ is the number of detected photons),

| **EM gain** | 50 | 100 | 150 | 200 | 250 | 300 |
|---|---|---|---|---|---|---|
| **a** | 2.2 ± 0.32 | 4.36 ± 0.66 | 6.52 ± 0.98 | 8.68 ± 1.3 | 10.92 ± 1.64 | 13.12 ± 1.94 |

Table 5.1: Averaged photon-to-count conversion factor $a$ for our EM-CCD camera (Andor iXon Du-860)

the conversion factor for each camera pixel can be obtained by illuminating the camera chip with a stable light source and recording a series of frames with different exposure times or intensities. Photon statistics follow a Poisson distribution, whose variance is equal to its mean. It follows that

$$\mathrm{Var}\left[S\right] = a^2 \mathrm{Var}\left[N\right] = a^2 \langle N \rangle = a \left( \langle S \rangle - b \right). \tag{5.3}$$

Plotting the variance over the mean of the measured counts allows determination of $a$ from a linear fit (either for individual pixels or averaged over the sensor). To account for the additional noise of the electron-multiplying register, the obtained values must be divided by 2 (Pawley, 2006). Table 5.1 shows the conversion factors for our camera.

## 5.2 Instrument Characterization

Our microscope is equipped with a three-axis piezo stage mounted on top of the manual microscope stage. This allows to characterize the instrument's performance using well-defined, pre-programmed trajectories that are independent of the tracking system. That way, systematic errors are easy to identify. In these experiments, the piezo stage is operated in closed-loop mode, specified to sub-nanometer accuracy.

### 5.2.1 Step Response

The elementary response of the tracking loop is characterized using step movement of the piezo stage, monitored separately along the three axes. Figure 5.3 shows results of these measurements for the $x$ and $y$ directions, characterizing the performance of the piezo mirror. These measurements were done at a frame rate of 3.2 kHz, which is the maximum without using the isolated crop mode mode of the camera. Later experiments, after making the isolated crop mode available in the tracking software, were done at 7.6 kHz. Figure 5.4 shows results of these measurements, comparing the axial tracking performance of the objective piezo and the deformable mirror.

For all experiments, a sample containing fixed 200 nm fluorescent beads (sample preparation following the protocol described in Appendix C.1) was mounted on the piezo stage. The laser intensity was chosen to yield a sufficiently bright signal at submillisecond exposure times while avoiding strong photobleaching. Every ∼50 ms,

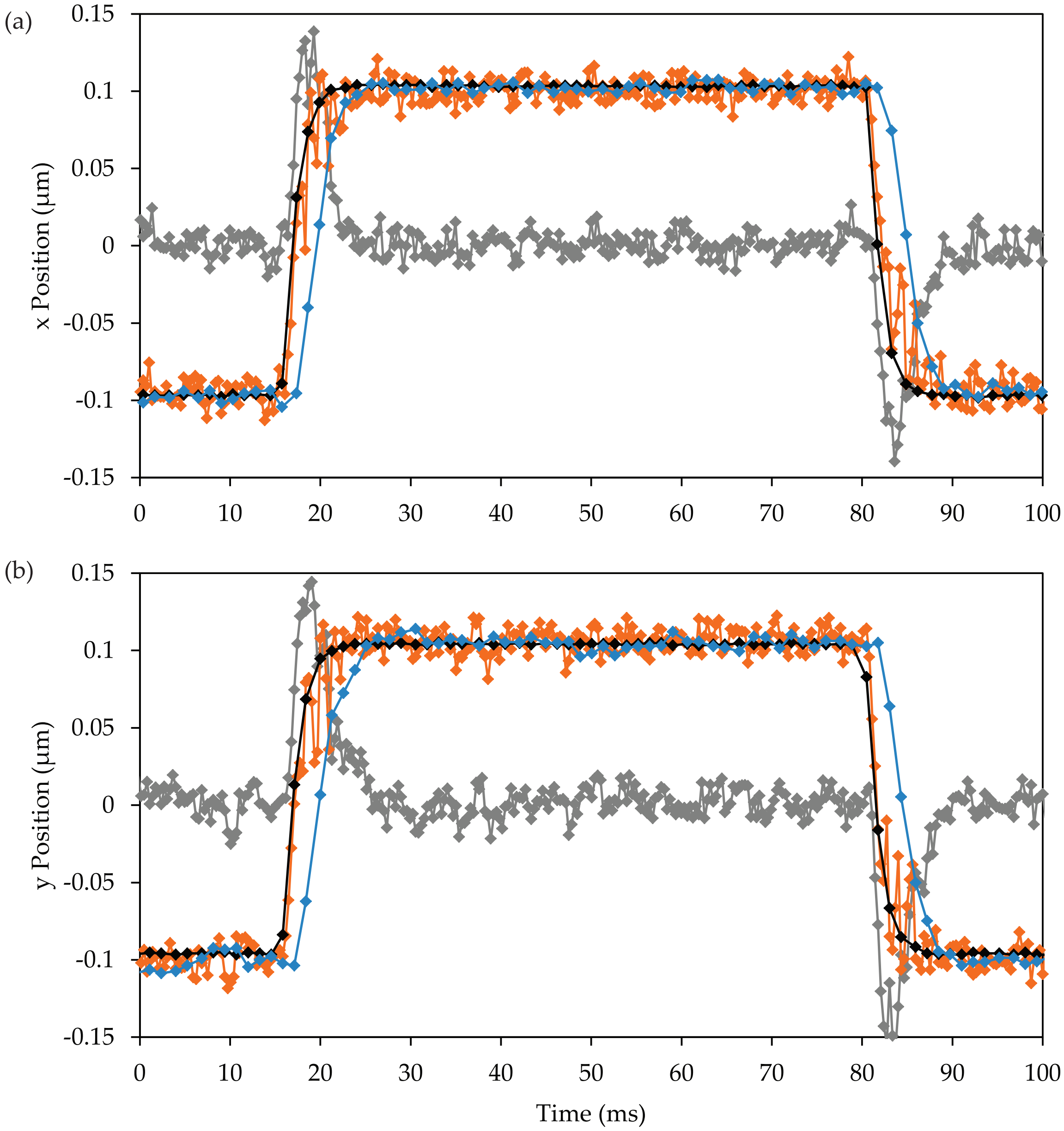

Figure 5.3: Lateral step response in the (a) $x$ and (b) $y$ direction, obtained by tracking a fixed fluorescent bead at 3.2 kHz while moving the sample in steps using the three-axis piezo stage. Black symbols and curve: stage position. Gray: Estimated bead position with respect to the laser focus. Blue: position of the laser focus. Orange: final trajectory, obtained as the sum of the gray and orange curves. Adapted from Juette and Bewersdorf (2010).

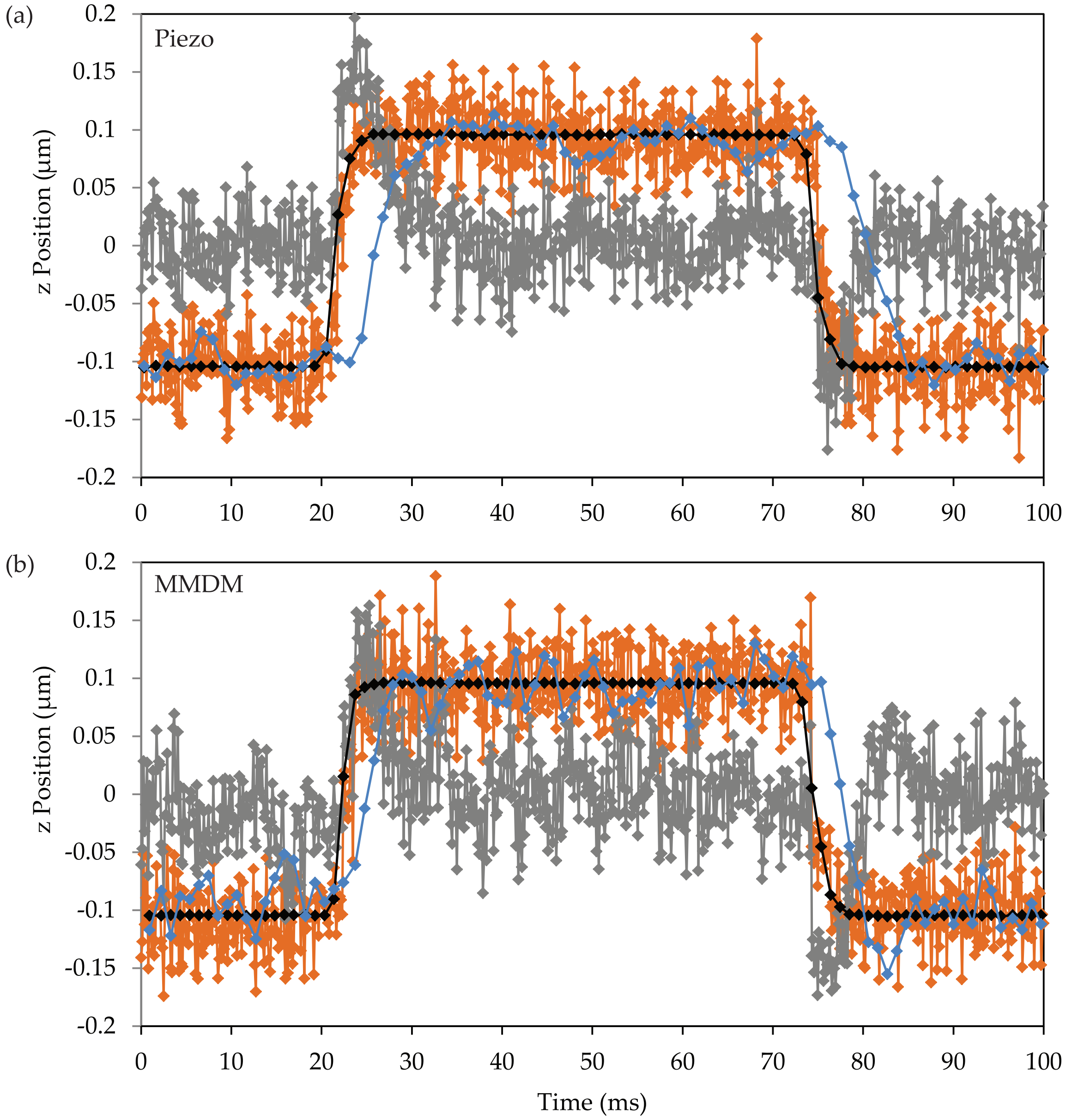

Figure 5.4: Axial step responses with (a) piezo mirror and (b) deformable mirror, obtained by tracking a fixed fluorescent bead at 7.6 kHz while moving the sample in steps using the three-axis piezo stage. Colors as in Figure 5.3.

the stage was shifted in either direction by 200 nm, while the instrument was set to track the position of the bead. In Figures 5.3 and 5.4, the position signal from the internal capacitive sensor of the stage is shown in black. For each frame, the position estimator (see Section 4.4) is calculated (shown in gray). The generated feedback signal leads to a (slightly delayed) response of the beam-steering element, shown in light blue. In post-processing, this signal is combined with the position estimator to obtain a precise, non-delayed measure of the particle position (orange).

The time delay between the registered motion and the response of the beam-steering element is about 2 ms for the piezo mirror, about 5 ms for the objective piezo. This axial response is improved to about 2 ms by using the deformable mirror. The localization precision is estimated by taking the position standard deviation over 150 frames while the stage is stationary in one position, yielding $\sigma_x = 7$ nm and $\sigma_y = 8$ nm for the lateral directions. In the axial direction, $\sigma_{\mathrm{OP}} = 26$ nm was obtained with the objective piezo, $\sigma_{\mathrm{DM}} = 27$ nm with the deformable mirror. This is consistent with the shape of the PSF, which is about 3-fold longer axially than laterally.

### 5.2.2 Localization Precision

According to Equation 2.6, the localization precision should scale inversely with the square root of the number of photons detected per frame. This is verified by tracking a fluorescent bead as described above, but without stage movement. After each measurement, the excitation intensity is increased. The localization precision is determind by taking the position standard deviation over 150 frames. The number of detected photons is estimated using the conversion factor from section 5.1.4. The resulting curve, which confirms the expected scaling behavior, is shown in Figure 5.5.

### 5.2.3 Programmed Trajectories

More complex two- and three-dimensional trajectories can be programmed into the piezo stage to characterize the tracking performance for directed motion. I used circles in the $x$-$y$, $x$-$z$, and $y$-$z$ planes, respectively, to determine the maximum velocity that can be tracked and reconstructed reliably.

Figures 5.6a and b show trajectories of single rotations of different diameters (between 200 nm and 7 µm) and at different tangential velocities, ranging from 5 nm/ms to 150 nm/ms. These trajectories were recorded using 200 nm fluorescent beads at a frame rate of 3.2 kHz.

The circles are reproduced accurately in all cases. As in the step functions discussed above, the tracking precision is about 3-fold worse in the axial than in the lateral direction, but well below the 100 nm radius of the smallest circle. The maximum speed of 150 nm/ms exceeds the velocities of all known processes involving motor proteins (Howard, 2001).

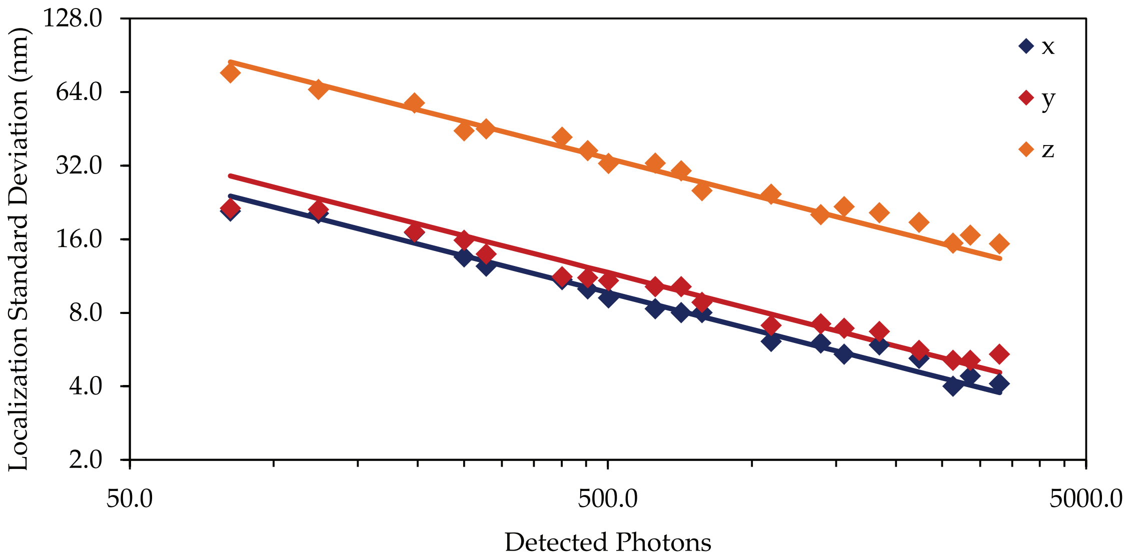

Figure 5.5: Localization precision as a function of detected photons. A fixed 200 nm fluorescent bead is imaged and tracked. The laser intensity is increased progressively and 150 frames are recorded for each intensity. The plot shows the determined standard deviations as a function of the number of detected photons, N. The displayed lines are proportional to $1/\sqrt{N}$ and were included to compare the measured data with the theoretically expected dependence. Figure adapted from Juette and Bewersdorf (2010), Supplement.

Figure 5.6c shows an example of a three-dimensional programmed trajectory, a helix aligned along the optical axis. This validates the system's capability to track complex 3D trajectories.

## 5.3 Applications

### 5.3.1 Finding Particles

The programmed trajectories used for characterization pass through defined positions. "Finding" them only requires to place the laser focus in one of these positions, and the particle will automatically be tracked. For all real applications, however, it is necessary to implement a way of locating particles for tracking.

The first step is to identify a region of interest (ROI). If a secondary (red) label for the overview channel is available, this is used to find such an area. Otherwise, a GFP filter cube can be switched in instead of the tracking filter set. This allows to monitor green fluorescence in a widefield view on the EM-CCD camera. In both cases, widefield excitation is provided by the metal halide arc lamp. Once the ROI is

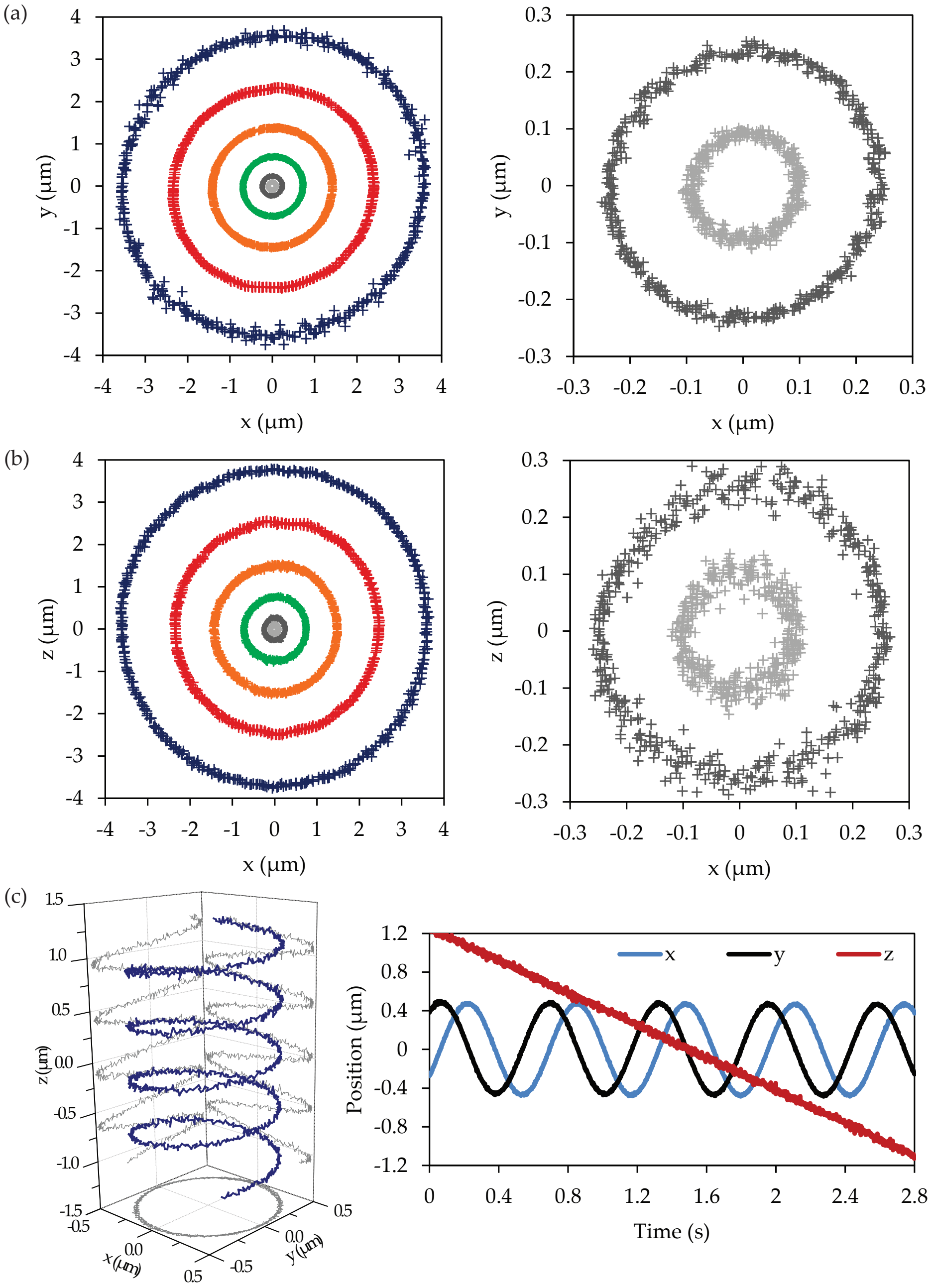

Figure 5.6: Trajectories programmed into a three-axis piezo stage, recorded by tracking 200 nm fluorescent beads. (a–b) Circular trajectories in the x-y (a) and x-z (b) planes with various radii r and velocities v, tracked at 3.2 kHz frame rate. Light gray: r = 100 nm, v = 5 nm/ms. Dark gray: r = 250 nm, v = 10 nm/ms. Green: r = 750 nm, v = 25 nm/ms. Orange: r = 1500 nm, v = 50 nm/ms. Red: r = 2500 nm, v = 100 nm/ms. Blue: r = 3750 nm, v = 150 nm/ms. (c) Helical trajectory, recorded at 500 Hz frame rate. Left: 3D reconstruction; right: x, y, and z coordinates as a function of time. Adapted from Juette and Bewersdorf (2010).

set and a tracking experiment is started, the instrument automatically searches for particles. I implemented three different search options into the tracking software:

- Simple thresholding. If the particle density in the sample is high, it is sufficient to keep the laser focus in a fixed position until a sufficiently bright object enters the field of view. Tracking begins as soon as a preset pixel intensity threshold is exceeded.

- Raster scanning. A two-dimensional plane segment or three-dimensional volume is scanned point by point, using the piezo mirror and objective piezo. Once the intensity threshold is exceeded, scanning is aborted and tracking begins.

- Random scanning. This is essentially the same as the second option, but instead of pre-generating a raster point array, a step of defined size, but in a random direction, is taken after each frame.

### 5.3.2 Diffusing Beads

The introductory motivation in Chapter 1 revolved around diffusion, which drives many biological processes and can be considered as the “speed limit” for intracellular motion. I therefore tested the ability of our microscope to track free three-dimensional diffusion over a range of diffusion coefficients.

This was done by suspending 200 nm fluorescent beads in mixtures of water and glycerol at different volume ratios, ranging from pure glycerol to pure water. Beads were then tracked at 3.2 kHz frame rate. Figure 5.7a and b show an example trajectory in pure water, recorded over a period of 3 s (corresponding to nearly 10,000 frames).

For each trajectory, the MSD was calculated as described in Chapter 2.3. Figure 5.7c shows the resulting MSD curves, obtained by averaging over 3 to 6 trajectories of lengths between 3 and 12 s for each concentration. The data was fit with a linear function to determine the diffusion coefficient D according to Equation 1.1. The obtained values for D (also shown in Figure 5.7c) range from 0.0017 $\mu m^2/s$ for pure glycerol to 2.4 $\mu m^2/s$ for pure water.

As a control for the obtained diffusion coefficients, the Stokes-Einstein relation (Equation 1.2) can be used to calculate the hydrodynamic radius for cases where the the dynamic viscosity $\eta$ is known. At 22°C, it is $8.8 \times 10^{-4}$ Pa s for glycerol and 1.27 Pa s for water (Haynes, 2012). The determined radii of (0.10 ± 0.02) µm for water and (0.100 ± 0.006) µm for glycerol are in excellent agreement with the specified bead radius of 0.1 µm.

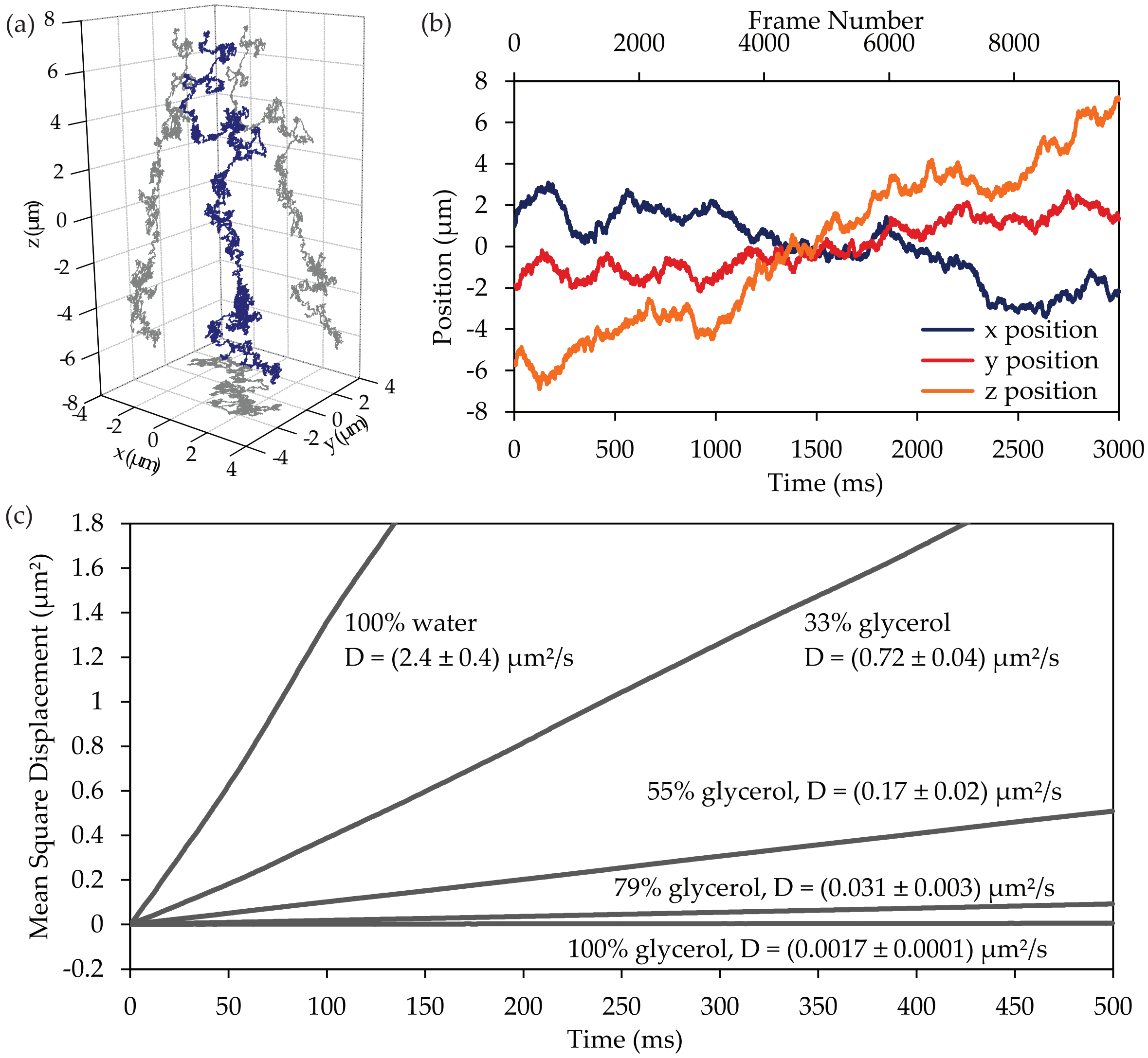

Figure 5.7: Free diffusion of 200 nm fluorescent polystyrene beads. (a) 3D rendering of the trajectory of a bead diffusing in pure water, recorded at 3.2 kHz frame rate for a duration of 3 s. (b) x, y, and z components of the same trajectory. (c) Mean square displacements (averaged over several trajectories) for beads diffusing in various mixtures of water and glycerol as indicated. The displayed diffusion coefficients D were obtained from the slopes of linear data fits.

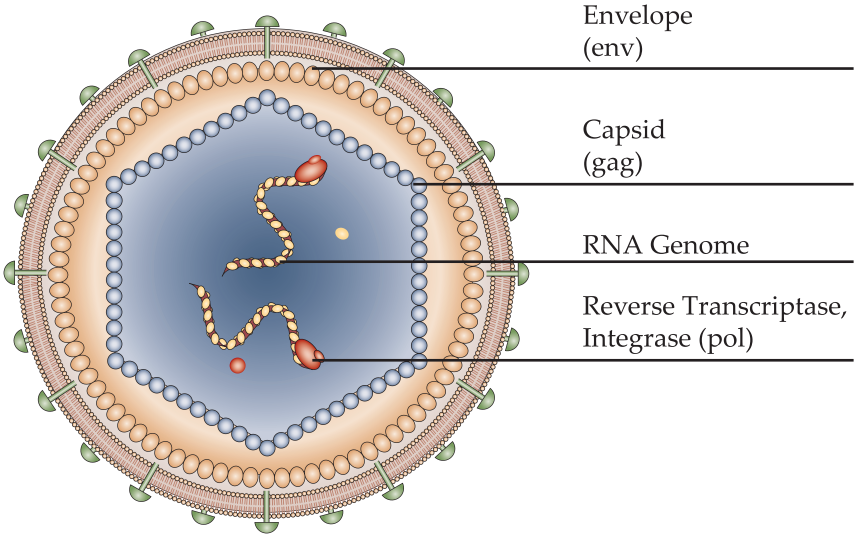

Figure 5.8: Schematic view of a murine leukemia virus. In parentheses: names of the gene regions coding for the viral proteins. Adapted from Silverman et al. (2010).

### 5.3.3 Live-Cell Particle Tracking

#### Viral Motion

A virus is a small infectious particle ($\lesssim 300$ nm) that has the ability to exploit a host cell's protein biosynthesis for its own replication. Retroviruses, specifically, contain an enzyme called reverse transcriptase, which transcribes the viral ribonucleic acid (RNA) to deoxyribonucleic acid (DNA), which is then incorporated into the host genome by another enzyme, integrase.

Murine leukemia virus (MLV), a virus that causes cancer in mice, is a frequently studied model retrovirus. Figure 5.8 shows a schematic view of a MLV particle. It consists of a protein structure, called the capsid, which contains the viral RNA and enzymes. The capsid is surrounded by a lipid envelope dotted with antigen proteins, which the virus uses to target receptors exposed on the plasma membrane of its cellular host.

To spread within the same organism, the virus uses mechanisms of direct transmission between neighboring cells (Mothes et al., 2010). After binding to a receptor on the membrane of the cell being infected, the virus engages the underlying actin cytoskeleton and "surfs" on the cell surface until it finds a preferred site for endcytosis (Lehmann et al., 2005). In collaboration with the Mothes lab, we wanted to test if we could visualize this surfing motion with out SPT microscope.

For these experiments, MLV particles containing several hundred GFP molecules were prepared by Dr. James Munro, following the protocol given in Appendix C.2. To assess the feasibility of virus tracking, we recorded trajectories of viral particles freely

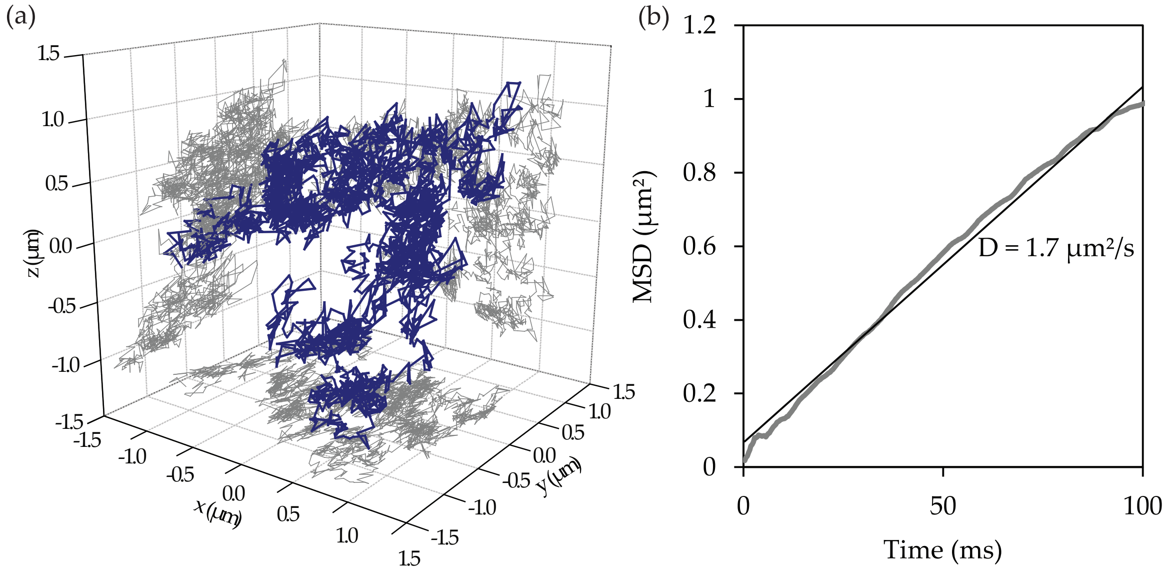

Figure 5.9: Diffusion of GFP-labeled murine leukemia virus in cell culture medium at 37°C. (a) 3D rendering of a 1 s long trajectory recorded at 3.2 kHz frame rate. (b) Mean square displacement and linear fit (with determined diffusion coefficient D).

diffusing in cell culture medium at 37°C. Figure 5.9 shows an example trajectory recorded at 3.2 kHz, along with the corresponding MSD. A linear fit to the MSD yielded a diffusion coefficient of 1.7 $\mu m^2/s$.

We then added the media containing the virus to living rat fibroblast cells expressing the receptor that MLV uses for cellular entry (see Appendix C.2). The receptor was labeled with mCherry for visualization in the overview channel. Correlating the tracking channel with the overview channel, we saw viral particles colocalized with receptor clusters on the cell membrane.

Subsequently, the expected directional surfing of the virus could be observed. Due to the relatively slow movement, tracking was performed at a frame rate of 50 Hz. Figure 5.10a shows a 2D projection of a representative trajectory overlaid with a widefield view recorded in the overview channel. Figure 5.10b is a 3D rendering of the same trajectory; subfigures c and d show the MSD and reduced MSD (see Chapter 2.3), respectively. The shape of the reduced MSD suggests directed transport in conjunction with intermediate confinement on shorter time scales (below approximately 1 second).

### Transport Vesicles

Receptor-mediated endocytosis (RME) is one of several processes by which cells internalize molecules. RME is based on the formation of membrane domains enriched in the cytosolic protein clathrin at sites where an external molecule has been recruited

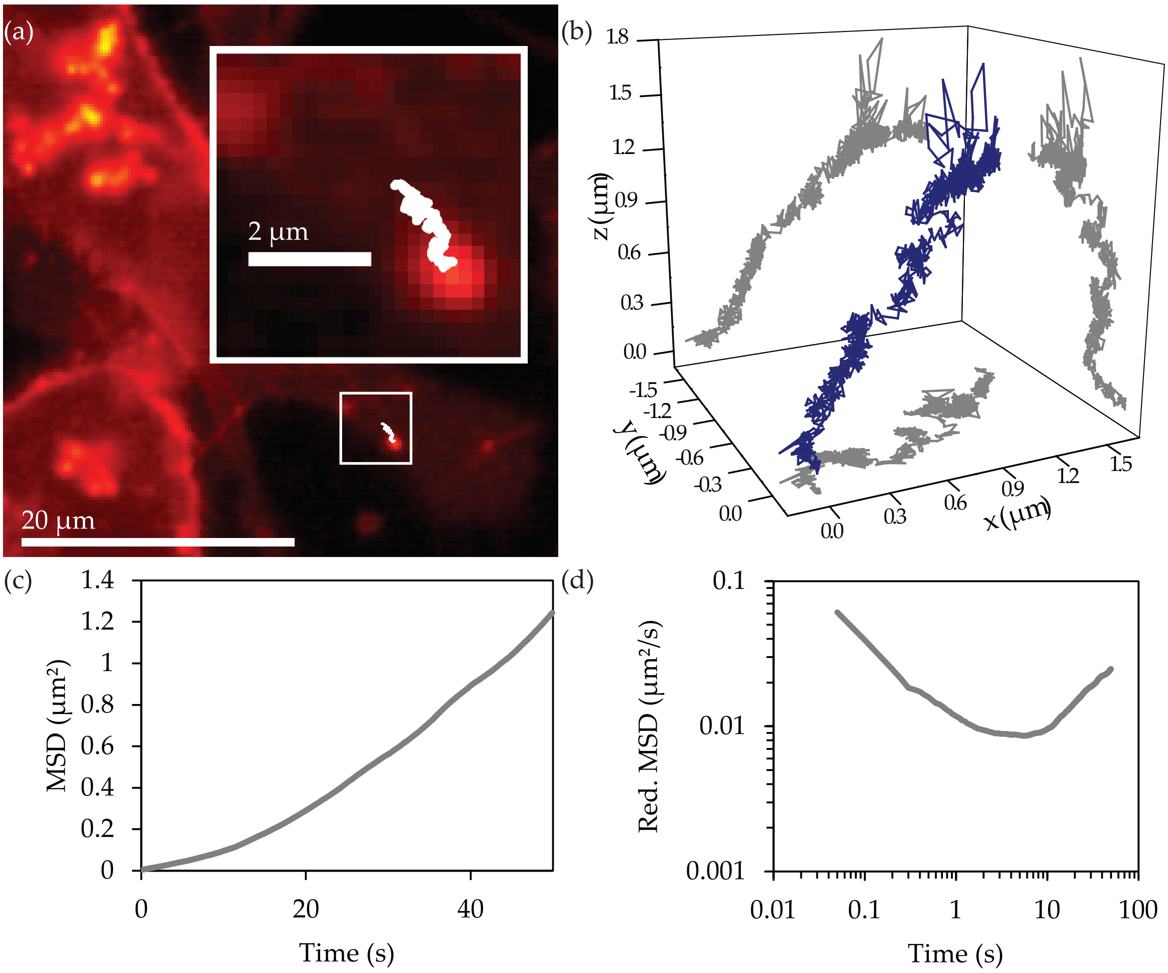

Figure 5.10: Surfing of a murine leukemia virus bound to MCAT receptor on the membrane of a living XC cell at 37°C. (a) Overlay (white) of a 90 s long trajectory trajectory (projected to the x-y plane; 20 ms time resolution) with a a widefield overview (red) showing the receptor distribution. (b) 3D rendering of the same trajectory. (c) Mean square displacement (MSD). (c) Double-logarithmic plot of the reduced MSD (MSD over time).

by a membrane-bound receptor. These clathrin-coated pits then bud off towards the interior of the cell, forming vesicles that are transported and processed by endocytic pathways (Alberts et al., 2007).

One example of a molecule internalized through RME is the glycoprotein transferrin (Goss and Toomre, 2008; Hopkins and Trowbridge, 1983). Transferrin occurs in the blood plasma and binds to free iron. The transferrin-iron complex binds to transferrin receptor on the plasma membrane of a cell. The entire complex, including the receptor, is subsequently taken up into the cytoplasma via formation of clathrin-coated vesicles. Their primary intracellular destination are early endosomes, intermediate compartments formed by the accumulation of vesicles. It has been shown (Jin and Snider, 1993) that transport along microtubules (cytoskeletal protein filaments) plays a central role in reaching this destination; this “sliding” is driven by the motor proteins kinesin and dynein (Howard, 2001).

In a collaboration with the Toomre lab, we used the SPT microscope to examine this transport process. Human umbilical vein cells were grown by Dr. Felix Rivera-Molina using the protocol described in Appendix C.3. The cells were incubated with transferrin labeled with the fluorescent dye Alexa 488, which was taken up by the cells. After incubation, intracellular transferrin trafficking could be observed in the perinuclear region of the cells. Finding areas of interest was aided by labeling of the transferrin receptor with mCherry.

The initial experiments were performed at room temperature (22°C), which slowed down dynamics and limited the time window available for observation to about 30 minutes. Nevertheless, trajectories of individual vesicles could be recorded, in this case at a frame rate of 10 Hz. Figure 5.11 shows an example trajectory and MSD analysis.

The experiments were then repeated (with new cells) at 37°C, and 31 vesicle trajectories were recorded at a temporal resolution of 1 ms. The lengths of obtained trajectories ranged from 70 to over 500 frames. The MSD for each trajectory was fitted with Equation 2.14, describing a superposition of diffusive and directed motion. Figure 5.12 shows the distribution of diffusion coefficients D and velocities v extracted from the fit, yielding averages of $v_{\text{average}}=(0.020 \pm 0.018)$ µm/s and $D_{\text{average}}=(2.1 \pm 1.7)$ $\mu m^2/s$.

### 5.3.4 Single Proteins

The following experiment was performed to verify the single-molecule sensitivity of the setup. Fluorescently labeled secondary antibodies (Alexa Fluor 488 Goat Anti-Mouse IgG H+L, Life Technologies) were diluted in phosphate-buffered saline (PBS), added to a coverslip, and dried. The SPT microscope was then used to find and track bright spots on the coverslip at a frame rate of 10 Hz.

According to the manufacturer, each antibody should be labeled with 4–6 dye molecules. To verify that a trajectory belongs to a single molecule (or a very small

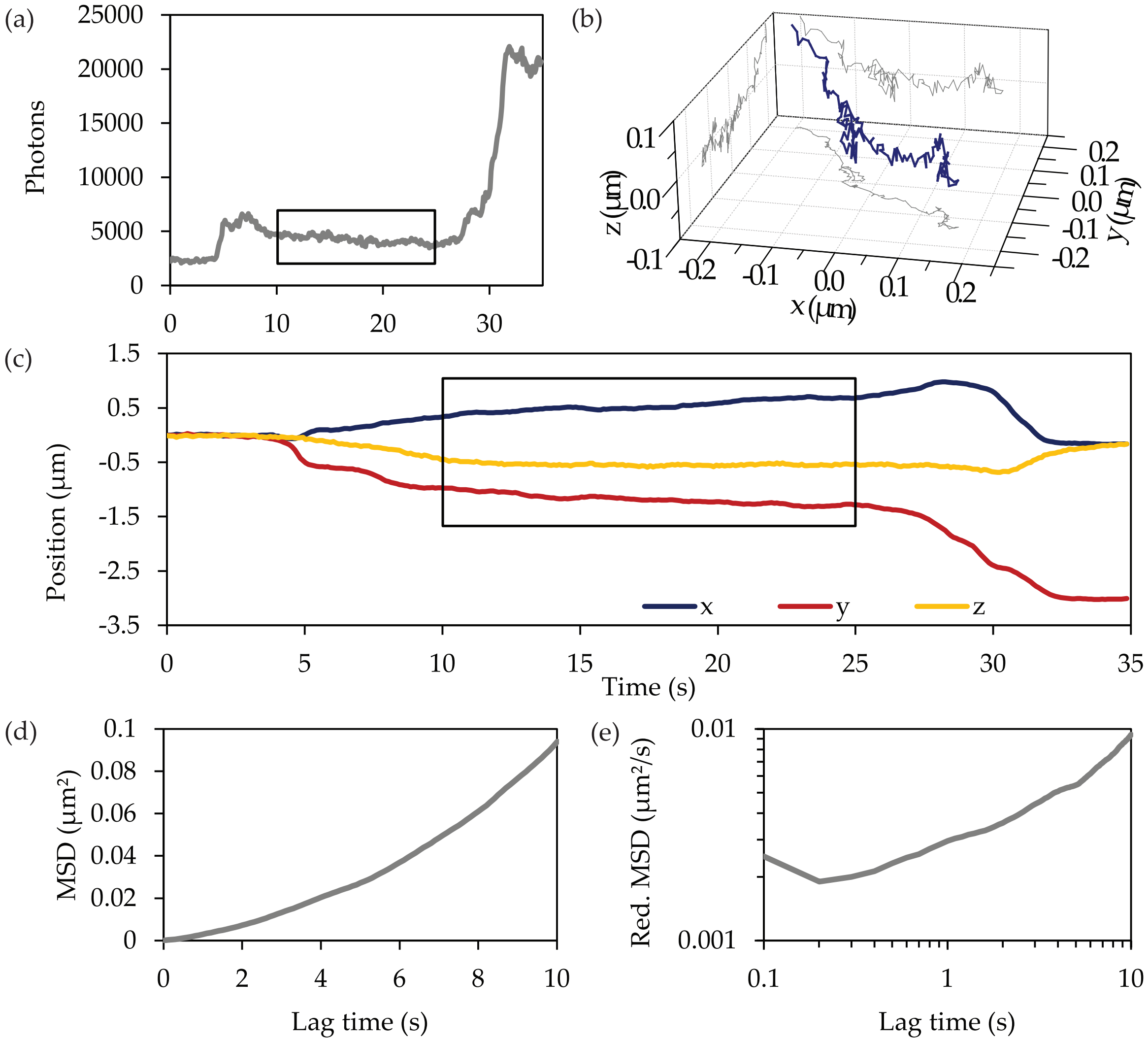

Figure 5.11: Trajectory of a single vesicle containing transferrin-Alexa 488, recorded at 10 Hz. (a) Photon counts per frame as a function of time. (b) 3D rendering of the trajectory segment marked by the boxes in a and c. (c) x, y, and z coordinates as a function of time. (d) Mean square displacement (MSD)) and (e) reduced MSD for the trajectory segment marked by the boxes in a and c.

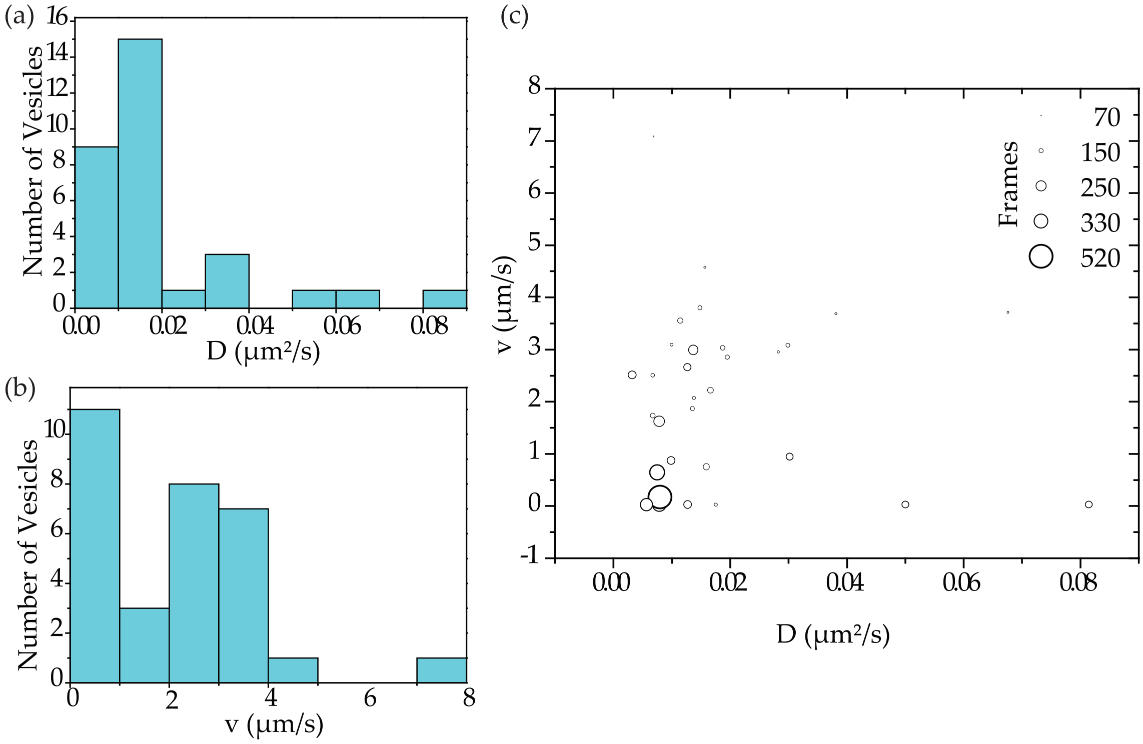

Figure 5.12: Distribution of diffusion coefficients and velocities for 31 single-vesicle trajectories obtained at 1 ms temporal resolution. (a) Histogram of diffusion coefficients D. (b) Histogram of velocities v. (c) Two-dimensional representation of the distribution of D and v. Each circle represents one measured trajectory. The size of the circle is proportional to the number of frames in each trajectory.

cluster), the number of registered photons over time can be analyzed. A small number of fluorophores should exhibit discrete steps in the photon trace, corresponding to single-fluorophore blinking and bleaching events. This characteristic behavior could be verified for 11 trajectories of up to 15 s length (Figure 5.13).

The localization precision for what can be assumed to be a single fluorophore was determined to be $\sigma_x = 8$ nm, $\sigma_y = 9$ nm, and $\sigma_z = 24$ nm for (1750 ± 160) photons emitted per 100 ms interval. In comparison, a fluorophore cluster emitting (7170 ± 730) photons per frame, was localized with precisions of $\sigma_x = 6$ nm, $\sigma_y = 7$ nm, and $\sigma_z = 19$ nm. This does not reflect the expected scaling behavior as shown in Figure 5.5. This may be explained by an influence of instrument drift, which becomes limiting at long exposure times. At first, it is also surprising that the step sizes in Figure 5.13 differ significantly. However, this can be explained by the different fixed orientations of the dye molecules in in the dried sample.

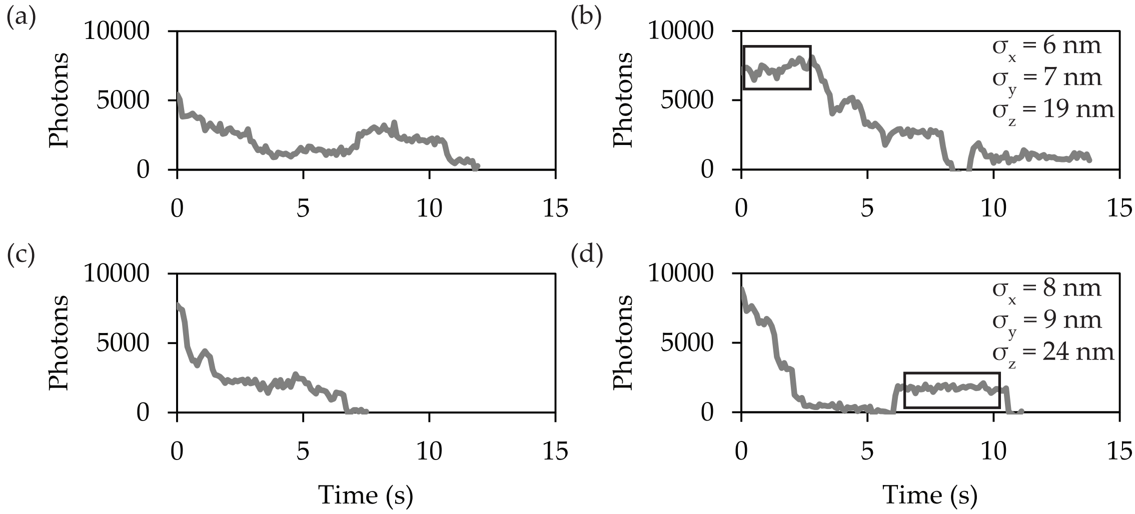

Figure 5.13: Number of registered photons as a function of time for four trajectories of Alexa 488-labeled IgG antibodies dried to a coverslip. For the boxed regions in (b) and (c), the standard deviation of particle localization was calculated as shown.

# 6 Discussion

> After all, can the human soul be glimpsed through a microscope? Maybe—but you'd definitely need one of those very good ones with two eyepieces.
>
> *"My Speech to the Graduates"*
> Woody Allen (1979)

## 6.1 Summary of Results

In this thesis, I have demonstrated three-dimensional tracking of fluorescent particles with a temporal resolution down to ∼130 µs. To achieve this performance over an extended depth range, the following factors had to be considered:

- Time resolution is limited by the readout frame rate.
- Good tracking precision requires high SNR.
- To keep an observed particle in focus over a large tracking range, real-time feedback must be used; the performance of the feedback system limits the range of dynamics that can be studied.

Our SPT microscope is optimized in all three aspects. Reading out only five lines of an EM-CCD sensor allows the collection of position data at a rate of up to 7.6 kHz. The two 5 × 5 pixel readout areas of only 750 nm side length inherently optimize the SNR by acting as confocal pinholes, which—in combination with focused laser excitation—results in good suppression of out-of-focus fluorescence. Detection sensitivity reaches the single-fluorophore level due to the low readout noise and high quantum efficiency of the EM-CCD camera.

The feedback mechanism relies on beam steering instead of slower stage-scanning. The new concept of using a deformable mirror for axial tracking makes the system response uniformly fast in all three dimension and avoids any mechanical coupling of the tracking motion into the sample.

The tracking capabilities of the instrument were evaluated quantitatively. The step response rise time of the system is 2 ms in the x, y, and z direction when the deformable mirror is used, and 5 ms in the z direction when using the objective piezo. From the reconstruction of programmed stage trajectories, I determined an upper velocity limit of 150 nm/ms for tracking directed motion. The highest measurable diffusion coefficient for free Brownian motion in 3D was 2.4 $\mu m^2/s$.

Localization precision, as determined from the standard deviation of repeated localizations, follows an expected inverse square root law depending on the number of detected photons per frame. In my experiments, it ranged from $21 \times 21 \times 77\ (nm)^3$ ($x \times y \times z$) for 80 detected photons to $4 \times 5 \times 15\ (nm)^3$ for 3000 detected photons. For brighter particles, it was limited by the mechanical noise of the feedback system.

The instrument was successfully used in live-cell experiments conducted at 37°C using a heated stage insert. As a part of the retroviral infection pathway, MLVs undergo an actin-driven surfing motion on the plasma membrane of a host cell. This directed motion was tracked with a time resolution of 20 ms, using viruses containing GFP. Small intracellular vesicles containing Transferrin glycoprotein (labeled with the fluorescent dye Alexa 488) were tracked at 1 ms time resolution as they were moving along microtubules.

To verify the single-fluorophore sensitivity of the microscope, I examined immobilized antibodies tagged with Alexa 488. They exhibited the typical blinking and stepwise photobleaching indicative of a single-fluorophore signal.

## 6.2 Perspectives in Feedback-Driven Single Particle Tracking

The strengths of Biplane SPT with feedback include high temporal resolution, a large three-dimensional tracking range, and effective background suppression through confocality. Of course, there are also some drawbacks compared to widefield-based SPT, mainly related to the problem of recording and correlating several simultaneous trajectories (as it is not possible to image multiple particles in a large field of view at once). In this outlook, I am suggesting strategies for addressing these shortcomings. In addition, I am discussing ways to further improve the technology and extend the scope of potential applications.

*Correlation of events.*—The widefield overview channel of our SPT microscope places trajectories in a structural context and allows for monitoring of morphological changes on an intermediate timescale. However, fast particle interactions can only be observed indirectly, e.g. by observing a change in diffusion coefficient upon binding of the tracked particle to an “invisible” partner.

This could be addressed by the addition of a second spectral channel for the same excitation and detection volume. Figure 6.1 shows a possible modification of the detection beampath. The two Biplane detection regions for the second channel

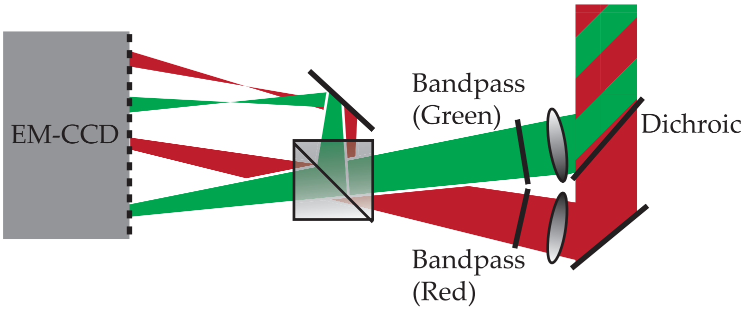

Figure 6.1: Schematic of proposed beampath modification for a second detection channel, using a longpass dichroic mirror to separate the two colors.

can be placed on the same five CCD lines as the primary channel, maintaining the high frame rate. By using red-shifted quantum dots or a long-Stokes-shift dye for the second channel, no additional excitation laser is necessary. A second laser can, however, be added for more flexibility in the choice of fluorophores.

This modification enables the observation of binding events or correlated motion of two particle species that are expected to stay close together throughout the process of interest. One could, for example, track the motion of a viral envelope protein with respect to the capsid, while the virus is surfing on the plasma membrane as described in Section 5.3.3. Another application might be simultaneous tracking of transferrin and transferrin receptor (see Section 5.3.3) or any other receptor-ligand system.

*Parallel acquisition of trajectories.*—It is not easily possible to create several laser foci of the same wavelength that can be independently moved in three dimensions. Multifocal microscopes using microlens disks (Bewersdorf et al., 1998) can only steer all foci in unison. A possible future solution might be stimulated by the development of polarization-independent high-resolution liquid crystal SLMs (Escuti and Jones, 2006). However, the added complexity might not be justified by the expected decrease in recording time provided by a small degree of parallelization.

A more promising path of parallel acquisition is to make the two spectral channels suggested above completely independent. This requires two separate sets of excitation and detection beam paths with independent beam steering and descanning. With this extension, one could track the fate of two partners during and after their interaction, e.g. of a viral antigen and the corresponding cellular receptor after endocytosis of the virus particle.

*Control of the particle density.*—To allow for a higher density of fluorescently labeled particles, optical control of fluorescence can be used. This only requires an additional laser (405 nm) for activation of photoswitchable fluorophores, like those used in pointillism microscopy (Fernández-Suárez and Ting, 2008). Upon activation of a target particle, the activation laser is immediately shut off by the acousto-optic tunable filter (AOTF). Photoswitching has previously been used to obtain high trajectory densities in widefield SPT (Appelhans et al., 2011; Hess et al., 2007; Manley et al., 2008).

*Integration of additional readout parameters.*—Using time-resolved point detectors, SPT can be combined with various spectroscopic methods. Wells et al. (2010) used tetrahedral detection for simultaneous tracking and fluorescence lifetime spectroscopy of quantum dots. Orbital scanning was originally conceived as a way to combine particle tracking with fluorescence correlation spectroscopy (FCS) (Berglund and Mabuchi, 2005; Levi et al., 2003). While our EM-CCD camera does not have sufficient time resolution for these types of spectroscopy, it should still be possible to obtain additional non-position information.

For example, the method can easily enable the readout of a Förster resonance energy transfer (FRET) signal. FRET, in short, is a dipole-dipole coupling of the excited state of one fluorophore (the donor) with the ground state of a nearby acceptor fluorophore. This resonance quenches donor fluorescence and enhances acceptor fluorescence in a strongly distance-dependent manner. This spatial sensitivity makes it a valuable tool for studying conformational dynamics in biomolecules (Lakowicz, 2006). In recent years, FRET measurements have been extended to the level of single donor-acceptor pairs (Roy et al., 2008).

Currently, FRET is limited to analyzing signal bursts in solution or, alternatively, studying substrate-bound in-vitro systems. 3D SPT-FRET would open up, for the first time, the possibility to monitor conformational events of molecules in a functionally undisturbed live-cell environment.

Instead of tracking two particles simultaneously, two-color detection can also be used to obtain two spectral channels for the same object. In combination with e.g. fluorescent sensors for pH (Bizzarri et al., 2009) or temperature (Vetrone et al., 2010), this could be used to probe physical and chemical parameters of local cellular environments in addition to diffusion properties.

*Further improvement of temporal resolution and response.*—Until recently, EM-CCD cameras were the only camera technology suitable for low-signal (e.g. single molecule) fluorescence application. This was largely due to the infavorable noise behavior of CMOS sensors. However, recent advances in scientific grade CMOS (sCMOS) technology have made such applications feasible (Z.-L. Huang et al., 2011). sCMOS sensors generally provide higher frame rates than their CCD counterparts, as line-shifting is made obsolete by readout registers for each individual pixel. In current commercial sCMOS cameras, the speed advantage is only noticeable for large ROIs, while for subregions of only a few lines, performance is comparable with EM-CCD cameras. However, this might change in the near future.

The mechanical response speed of the beam-steering system could be further improved by replacing our combination of a piezo mirror and a deformable mirror by two deformable mirrors in a “woofer-tweeter” configuration. This scheme has been introduced in adaptive optics for correcting aberrations with both high temporal bandwidth and high spatial resolution (Brennan and Rhoadarmer, 2006). High-frequency fluctuations are handled by a very small MMDM, the tweeter, whose

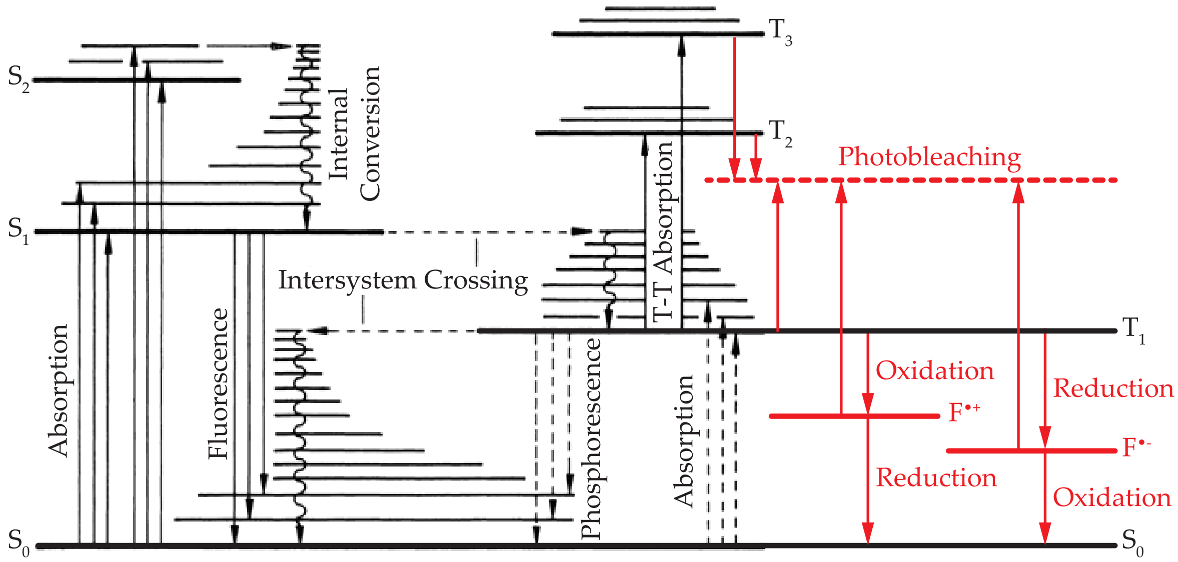

Figure 6.2: Simplified Jablonski diagram of an organic fluorophore. Black: textbook view, adapted from Haken and Wolf (2006). Red: influence of the chemical environment as described in recent literature (Ha and Tinnefeld, 2012; Linde et al., 2011).

mechanical response can be as fast as 20 µs (e.g. Multi-DM, Boston Micromachines). Slower and larger fluctuations are handled by a large-diameter deformable mirror, the woofer, whose low membrane stiffness allows for simultaneous generation of large tilt and defocus terms (e.g. Mirao, Imagine Optic). Such a system could provide full 3D focal positioning with a time response determined by the tweeter.

*Photophysics of fluorescent probes.*—While hardware improvements can increase the frame rate and beam-steering response of the SPT microscope, intensity and long-term stability of fluorescence emission are the most crucial parameters for improving temporal resolution, localization precision, the length of recorded trajectories, and the trade-off between these connected parameters. Brightness and photostability of a fluorophore are determined by the molecule’s intrinsic photophysics as well as the effect of its chemical environment.

The advent of single-molecule fluorescence spectroscopy and microscopy has been accompanied by an increased interest in understanding and controlling the involved molecular states and their transitions (Figure 6.2). In an ideal scenario, a fluorophore should alternate indefinitely between the ground state $S_0$ and the first excited singlet state $S_1$, limited only by the cross-section for photon absorption and the (nanosecond) lifetime of the excited state.

However, two types of phenomena interrupt this cycle: blinking and photobleaching (Ha and Tinnefeld, 2012). Blinking is the intermittent transition of a fluorophore to a state with a longer lifetime. This includes excited triplet states ($T_1$, $S_2 \ldots$) as well as radical ionized states ($F^{\bullet +}$, $F^{\bullet -}$), which can occur in the presence of reducing or oxidizing agents. Photobleaching is mostly induced by an irreversible reaction of the fluorophore with molecular oxygen. It is closely related to blinking, as the fluorophore is particularly susceptible to these reactions while in a triplet or radical state.

While long-lived dark states are a necessity in pointillism microscopy (Linde et al., 2011), their impact on fluorophore brightness and lifetimes is highly detrimental in most other applications, including SPT. Addition of triplet-quenching and oxygen-scavenging reagents to the imaging buffer can help in tuning fluorophore performance; however, the presence of these substances is often problematic in live-cell experiments (Ha and Tinnefeld, 2012). SPT and other single-molecule techniques can therefore benefit from the emerging development of intrinsically stabilized fluorescent probes with greatly enhanced brightness and reduced susceptibility to photobleaching (Altman et al., 2012). In synergy with expected advances in readout and beam-steering technologies, the study of nanoscale dynamics in the microsecond regime seems within reach.

# Appendices

# A Software Package

The SPT instrument is controlled by a custom software package written in LabView[1], named "Aerobatics". Similar to commercial microscope software, the user interface of Aerobatics consists of two panels, displayed side-by-side on two screeens (Figure A.1.) Panel 1 contains input fields for important experiment parameters and sliders to regulate the intensity of the light sources and the position of the beam-steering system. A function generator for the piezo stage, control of an external relay for switching additional hardware, and options for automated collection of data are also integrated. Dialogs for calibration and data analysis can be launched from the main window.

Panel 2 displays scalable live views of the two camera channels, zoomed up views of the two Biplane ROIs, and time traces of the position estimator and CCD counts. Updating of the live viewer is disables during high-frame rate experiments to avoid additional latencies caused by the display driver.

Software architecture is based on an event-machine design pattern (Blume, 2007), consisting of a single main loop that processes user interactions, updates the display, and calls sub-routines dynamically as needed (Figure A.2a). All configuration and measurement data is stored in a cluster, the LabView equivalent of a C-type struct, which is passed through successive iterations of the main loop by means of a shift register.

The core functionality, i.e. the fast feedback system for tracking experiments, is implemented as a set of parallel loops (Figure A.2b), which pass timing and data via notifiers. Independent parallel tasks are automatically distributed among the four available processor cores for best performance.

---

[1] LabView is a graphical programming environment based on the data-flow paradigm, which implements execution control as a wiring pattern connecting data sources and sinks represented as icons on a flow chart-like block diagram.

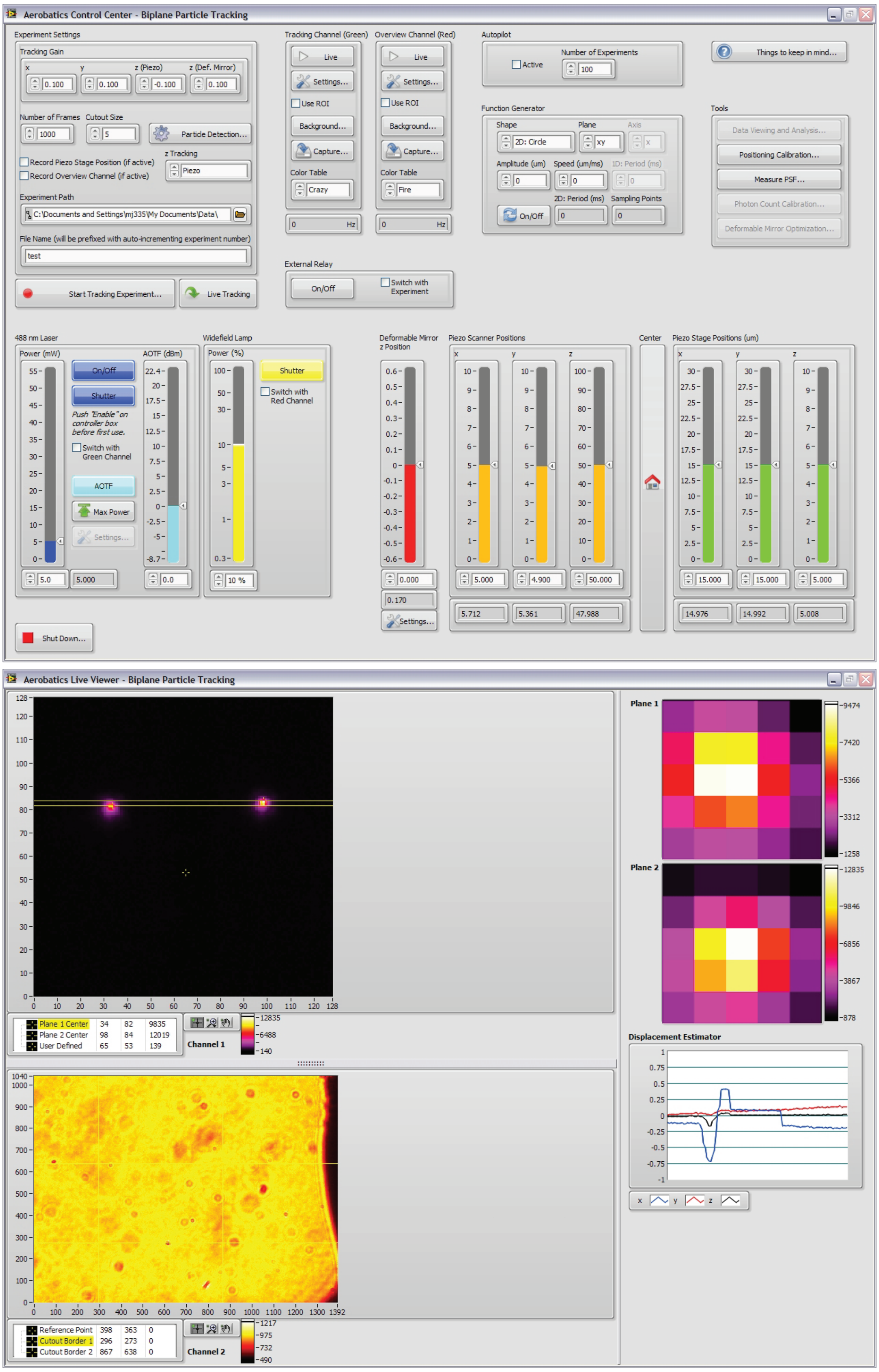
Aerobatics Control Center - Biplane Particle Tracking
Experiment Settings
Tracking Gain
Live
Settings...
Background...
Capture...
Particle Detection...
Start Tracking Experiment...
Live Tracking
On/Off
Things to keep in mind...
Function Generator
Tools
Data Viewing and Analysis...
Positioning Calibration...
Measure PSF...
Photon Count Calibration...
Deformable Mirror Optimization...
488 nm Laser
Shutter
AOTF
Max Power
Push "Enable" on controller box before first use.
Widefield Lamp
Deformable Mirror z Position
Piezo Scanner Positions
Center
Piezo Stage Positions (um)
Shut Down...
Aerobatics Live Viewer - Biplane Particle Tracking
Plane 1
Plane 2
Displacement Estimator
Channel 1
Channel 2
9474
7420
5366
3312
1258
12835
9846
6856
3867
878
1
0.75
0.5
0.25
0
-0.25
-0.5
-0.75
-1
x
y
z

Tracking Gain: x 0.100; y 0.100; z (Piezo) -0.100; z (Def. Mirror) 0.100

Number of Frames: 1000

Cutout Size: 5

☐ Record Piezo Stage Position (if active)

☐ Record Overview Channel (if active)

z Tracking: Piezo

Experiment Path: C:\Documents and Settings\mj335\My Documents\Data\

File Name (will be prefixed with auto-incrementing experiment number): test

Tracking Channel (Green): ☐ Use ROI; Color Table: Crazy; 0 Hz

Overview Channel (Red): ☐ Use ROI; Color Table: Fire; 0 Hz

External Relay: ☐ Switch with Experiment

Autopilot: ☐ Active; Number of Experiments: 100

Shape: 2D: Circle; Plane: xy; Axis: x

Amplitude (um): 0; Speed (um/ms): 0; 1D: Period (ms): 0

2D: Period (ms): 0; Sampling Points: 0

488 nm Laser: Power (mW) 5.0, 5.000; ☐ Switch with Green Channel; AOTF (dBm) 0.0

Widefield Lamp: Power (%) 10 %; ☐ Switch with Red Channel

Deformable Mirror z Position: 0.000; 0.170

Piezo Scanner Positions: x 5.000, 5.712; y 4.900, 5.361; z 50.000, 47.988

Piezo Stage Positions (um): x 15.000, 14.976; y 15.000, 14.992; z 5.000, 5.008

| | | | |
|---|---|---|---|
| Plane 1 Center | 34 | 82 | 9835 |
| Plane 2 Center | 98 | 84 | 12019 |
| User Defined | 65 | 53 | 139 |

Channel 1: 12835, 6488, 140

| | | | |
|---|---|---|---|
| Reference Point | 398 | 363 | 0 |
| Cutout Border 1 | 296 | 273 | 0 |
| Cutout Border 2 | 867 | 638 | 0 |

Channel 2: 1217, 975, 732, 490

Figure A.1: Aerobatics user interface. Top: control panel. Bottom: live viewer window.

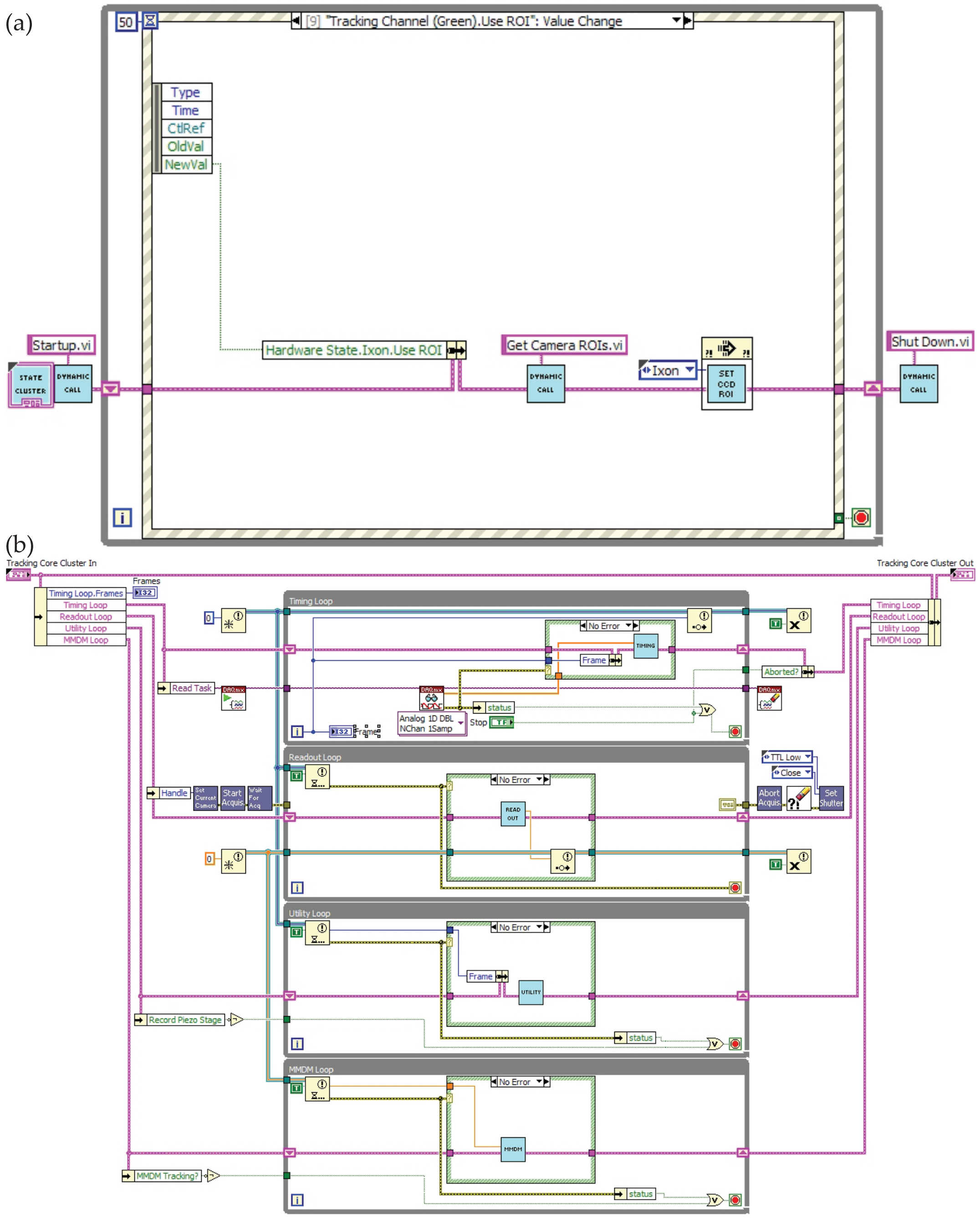
(a)
50
[9] "Tracking Channel (Green).Use ROI": Value Change
Type
Time
CtlRef
OldVal
NewVal
Startup.vi
STATE CLUSTER
DYNAMIC CALL
Hardware State.Ixon.Use ROI
Get Camera ROIs.vi
Ixon
SET CCD ROI
Shut Down.vi
i
(b)
Tracking Core Cluster In
Tracking Core Cluster Out
Frames
Timing Loop.Frames
Timing Loop
Readout Loop
Utility Loop
MMDM Loop
Read Task
Analog 1D DBL NChan 1Samp
status
Stop
No Error
Frame
TIMING
Aborted?
TTL Low
Close
Handle
Set Current Camera
Start Acquis.
Wait For Acq
Abort Acquis.
Set Shutter
READ OUT
UTILITY
Record Piezo Stage
MMDM
MMDM Tracking?

Figure A.2: Aerobatics code architecture. (a) Top-level event loop coordinating user interactions, data processing, and hardware operation. (b) Core implementation of the fast feedback loop, reflecting the operational design in Figure 4.7.

# B Spectra

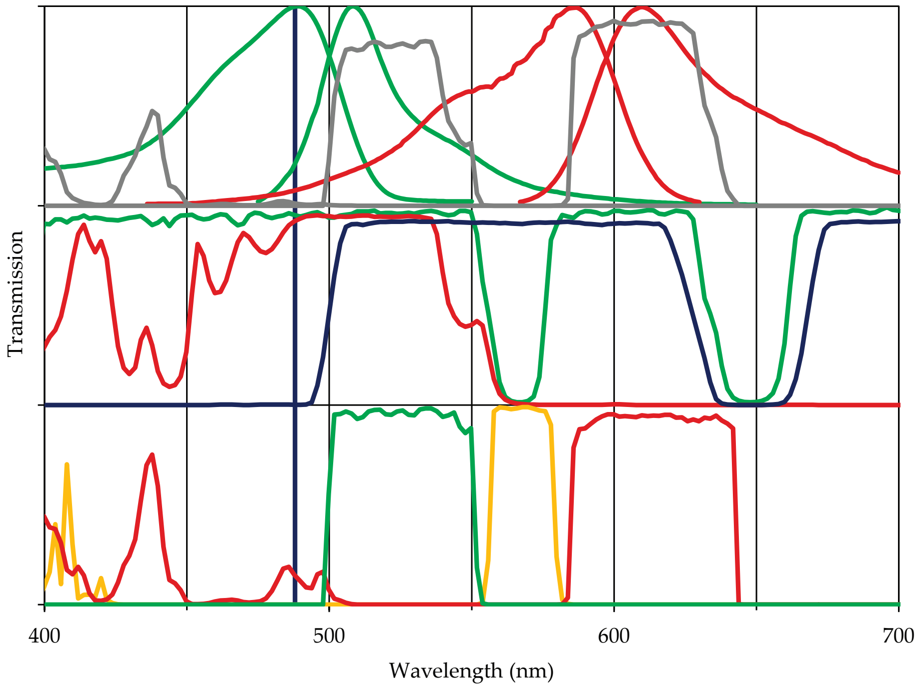

Figure B.1: Spectra of fluorophores and optical components. Refer to Figure 4.1 for naming of the components. Top row: absorption and emission spectra of fluorescent proteins EGFP (green) and mCherry (red) along with the effective detection bands (grey) for the green and red channels. Middle row: Transmission spectra of dichroic mirrors DM1 (blue), DM3 (red), and DM4 (green). Bottom row: transmission spectra of bandpass filters BP1 (green), BP2 (red), and BP3 (orange). The 488 nm laser line is shown in blue across all three rows. Sources of spectra: Fluorescent proteins – fluorophore database at `http://www.fluorophores.tugraz.at/`. Optical components – manufacturer website at `http://www.semrock.com`.

# C Sample Preparation

## C.1 Bead Samples

All bead samples were prepared using 200 nm fluorescent polystyrene beads (FluoSpheres Carboxylate-Modified Yellow-Green Microspheres, Life Technologies) with an absorption maximum at 505 nm and fluorescence peak at 515 nm. The stock suspension of beads was diluted in PBS to the desired concentration. For fixed bead samples, coverslips were incubated with 20 µl Poly-L-Lysine (Sigma Aldrich) for 10 minutes, washed with purified water, and subsequently incubated with 20 µl bead suspension. Excess suspension was washed of with purified water, and the dried coverslips were fixed to glass slides with two-component dental glue (Twinsil, Picodent).

For diffusion experiments, a sub-microliter amount of the bead suspension was diluted with several milliliters of the desired mixture of water and glycerol. 35 mm diameter cell cuture dishes with a coverslip bottom were completely filled with the bead dilution and the lid fixed with parafilm to prevent evaporation and convection that would influence the observed dynamics.

## C.2 Generation of Murine Leukemia Virus particles

Dr. James Munro prepared the retrovirus particles used for the experiments described in Chapter 5.3.3. They were generated by co-transfecting HEK293 cells with three plasmids: MLV Gag-GFP, MLV Gag-Pol, and MLV Env. This generates an approximately native and mature MLV virus with GFP in the core. The virus is pinched off from the cell membrane into the media. 24 hours after transfection, the media is collected, filtered to remove cell debris, and the virus is concentrated by ultracentrifugation. XC cells (rat fibroblasts) were used as the target cell line. The cells were made to stably express MCAT-mCherry by Dr. ing Jin. MCAT is the receptor used by MLV to induce endocytosis.

## C.3 EA.hy926 starvation and Transferrin-Alexa488 uptake

The cells for the vesicle experiments in Chapter 5.3.3 were prepared by Dr. Felix-Rivera Molina using the following protocol. EA.hy926 cells were plated and grown for two days in glass-bottom dishes with media plus 10 % fetal bovine serum (FBS) at 37°C. Cells were starved for two hours with media plus 0.1 % bovine serum albumin (BSA) before the addition of 10 µg/ml of Transferrin-Alexa488 (Tf-488) diluted in the same starvation media. The cells were then incubated at 37řC for 1 h. After the Tf-488 uptake incubation, the cells were washed twice with 1 ×PBS, pH 7.4, at room temperature, and washed once with 50 mM 2-(N-morpholino)ethanesulfonic acid (MES), pH 5.0, and 150mM NaCl to remove the membrane bound Tf-488. Cells were washed again with 1 ×PBS (twice). Media with 5 % FBS was used to image the cells.

# D Electronics

The deformable mirror voltages are supplied by a 40-channel high voltage amplifier. Some channels were defective or exhibited strongly non-linear characteristics and had to be replaced. Reverse-engineering of the four-channel subunits of the amplifier allowed replication on stripboard. The amplifier has a three-stage design, consisting of an operational amplifier in non-inverting configuration followed by two bipolar junction transistor amplifiers in common-emitter and emitter-follower mode.

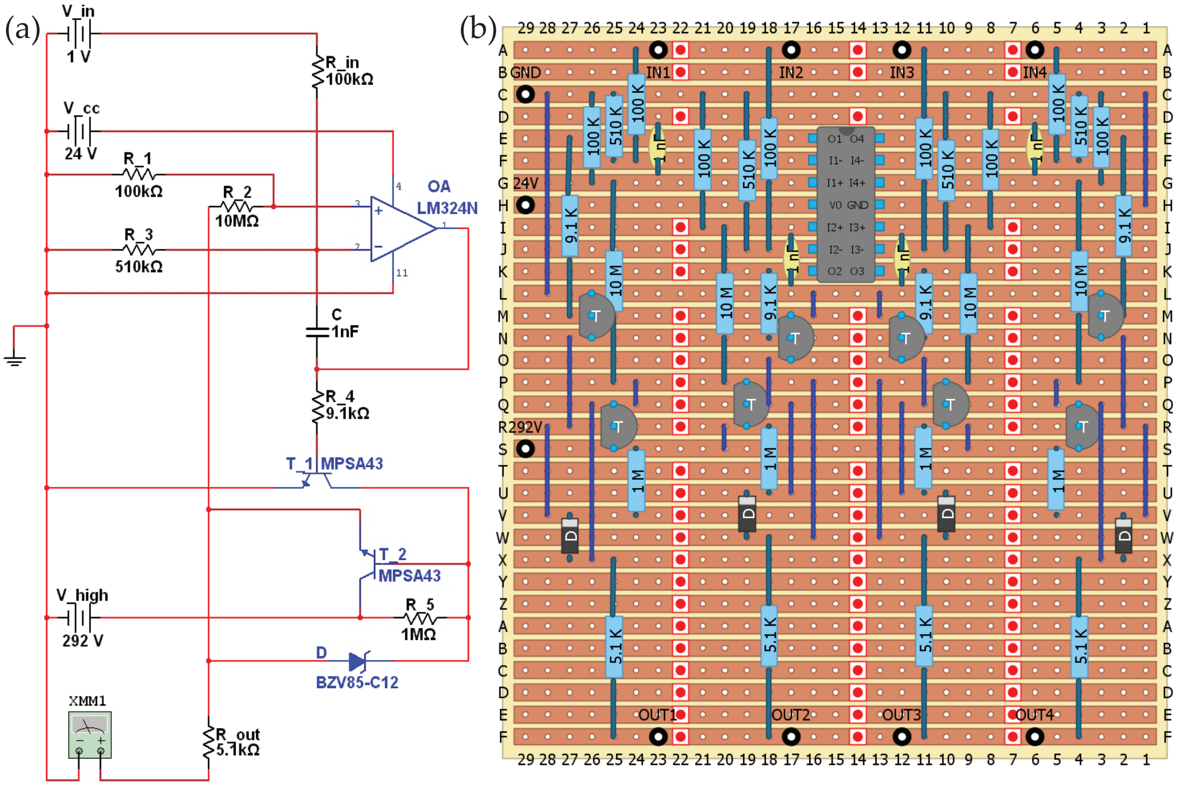
(a)
V_in
1 V
R_in
100kΩ
V_cc
24 V
R_1
100kΩ
R_2
10MΩ
R_3
510kΩ
OA
LM324N
C
1nF
R_4
9.1kΩ
T_1 MPSA43
T_2
MPSA43
V_high
292 V
R_5
1MΩ
D
BZV85-C12
XMM1
R_out
5.1kΩ
(b)
GND
24V
R292V
IN1
IN2
IN3
IN4
OUT1
OUT2
OUT3
OUT4
100 K
510 K
9.1 K
10 M
1 M
5.1 K
1 n
T
D
O1 O4
I1- I4-
I1+ I4+
V0 GND
I2+ I3+
I2- I3-
O2 O3

Figure D.1: Deformable mirror high voltage amplifier circuit. (a) Circuit diagram of single channel as constructed in Multisim for circuit simulation. (b) Stripboard layout of four-channel assembly.

# E Air Vibrations

Any high-precision particle tracking microscope, especially one with sub-millisecond temporal resolution, is naturally susceptible to air vibrations. To demonstrate this effect, Dennis Brain's classic rendition of the catchy Rondo from the Horn Concerto No. 4 in E Flat Minor by W.A. Mozart was played back at a moderate volume, with the speaker pointed at the microscope stage. A 200 nm fluorescent bead fixed to a coverslip was tracked at a frame rate of 3.2 kHz. The obtained trajectory was processed by adding up the components for each axis, baseline-subtracted, normalized, and converted to a wave file (Figure E.1). Listeners familiar with the piece were able to hum along with this recording. The lowpass filter applied by the microscope led to a pleasant underwater ambiance. However, an application of the instrument as a microphone is only conceivable in extremely well funded recording studios.

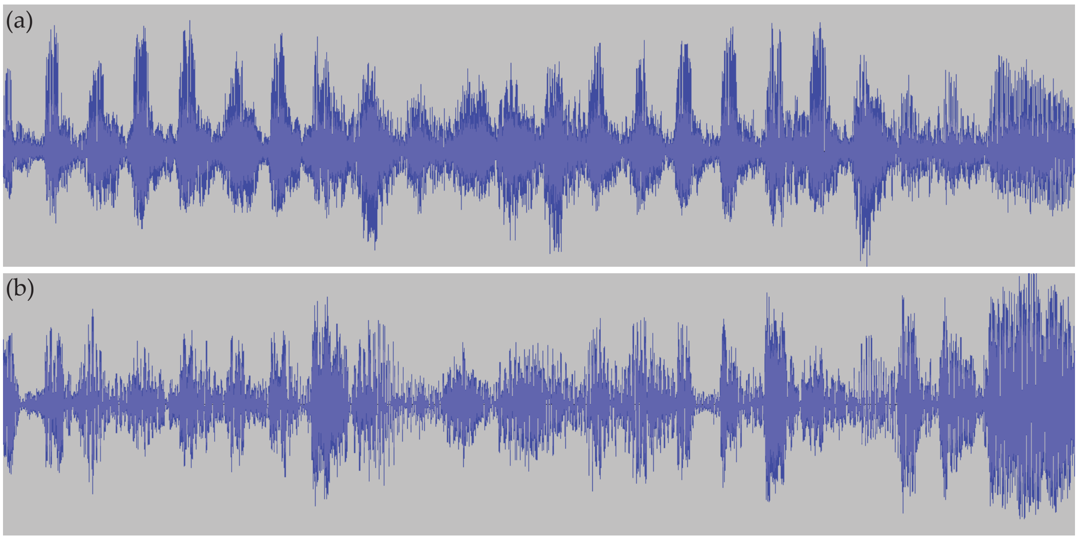

Figure E.1: Air vibration measurement. (a) Original wave file (stereo channels added up). (b) Wave file reconstructed from particle tracking at 3.2 kHz for 4 seconds. Note that the differences between the two waveforms reflect not only the characteristics of the microscope, but also those of the playback equipment.

# Back Matter

# Acknowledgments

> I love deadlines. I love the whooshing noise they make as they go by.
>
> *The Salmon of Doubt*
> Douglas Adams (2002)

A great number of people have contributed to making this work possible and enjoyable, whether by direct involvement, by providing opportunities, by ideas and discussion, or simply by being friends. My gratitude extends toward anyone who has made a scientific or personal impact on me during this ongoing endeavor.

Prof. Joachim Spatz generously agreed to supervise my work and referee my thesis, providing valuable support and guidance along the way.

Prof. Jörg Bewersdorf, in whose lab it all happened, has been an excellent scientific mentor, and his ever-expanding group a great environment for learning about all aspects of microscopy and the business of science.

This is also, in no small part, thanks to the members of the Bewersdorf lab with whom I had the great experience to work with, in particular (and in alphabetical order) Ed Allgeyer, Felix Dietrich, Travis Gould, Tobias Hartwich, Fang Huang, Jane Long, Emil Kromann, Marika Kuschan, Mike Mlodzianoski, Jordan Myers, and George Sirinakis.

Prof. Matthias Weidemüller and Prof. Matthias Bartelmann kindly agreed to be part of my defense comittee.

Prof. Christoph Cremer got me started on the road to microscopy and helped me acquire funding.

Prof. Martin Booth shared his authoritative knowledge on adaptive optics.

Prof. Walter Mothes, Prof. Derek Toomre, James Munro, and Felix Rivera-Molina were a pleasure to collaborate with for the live-cell projects and a key component of the “larger feedback loop”.

Eugene Modzelewski was helpful in figuring out any electronics issues and always had a few resistors to spare.

The Yale cell biology department would not be functional without Leslie Gourlay and Marsha Maresca. Marsha also helped with all issues relating to visa and coordinating two universities.

Yvette Harbers of the University of Heidelberg patiently answered many questions and helped with the administrative side of getting a degree.

Eva Hussain of the German Academic Exchange Service (DAAD) was very helpful with all my fellowship-related inquiries.

My colleagues at Leica—Marcus Dyba, Jonas Fölling, Arnold Giske, Jochen Sieber, Derek Webster—showed me a new perspective on instrument development right before embarking on my PhD quest and were great fun to hang out with. Dietmar Gnass, Volker Seyfried, and Tanjef Szellas made this experience possible.

Marcus Dyba also provided useful information about the pupil planes of Leica objectives.

My parents, Fritz and Rosemarie Juette, support me in every possible way and even reluctantly accept the fact that I am still not returning to Europe.

And finally, my girlfriend Francesca Bottanelli had to put up with all the stress and long nights connected with finishing a PhD. Thank you for being the greatest support imaginable!

# Statement of Authorship

This thesis is my own work. I have only used the sources indicated and have not made unauthorised use of services of a third party. Where the work of others has been quoted or reproduced, the source is always given. I have not presented this thesis or parts thereof to a university as part of an examination or degree.

New Haven, September 20, 2012
Manuel F. Juette

# Erklärung der Urheberschaft

Bei der vorliegenden Dissertation handelt es sich um meine eigenständig erbrachte Leistung. Ich habe nur die angegebenen Quellen und Hilfsmittel benutzt und mich keiner unzulässigen Hilfe Dritter bedient. Insbesondere habe ich wörtlich oder sinngemäß aus anderen Werken übernommene Inhalte als solche kenntlich gemacht. Die Arbeit oder Teile davon habe ich bislang nicht an einer Hochschule des In- oder Auslands als Bestandteil einer Prüfungs- oder Qualifikationsleistung vorgelegt.

New Haven, den 20. September 2012
Manuel F. Juette

# Bibliography

Abbe, E. (1873). “Beiträge zur Theorie des Mikroskops und der mikroskopischen Wahrnehmung.” *Archiv für Mikroskopische Anatomie* **9** (1), pp. 413–468. DOI: `10.1007/BF02956173` (cit. on p. 10).

Albert, O.; Sherman, L.; Mourou, G.; Norris, T. B.; Vdovin, G. (Jan. 2000). “Smart microscope: an adaptive optics learning system for aberration correction in multiphoton confocal microscopy.” *Optics Letters* **25** (1), pp. 52–54. DOI: `10.1364/OL.25.000052` (cit. on p. 46).

Alberts, B.; Johnson, A.; Lewis, J.; Raff, M.; Roberts, K.; Walter, P. (Nov. 2007). *Molecular Biology of the Cell*. 5th ed. Garland Science (cit. on pp. 2, 61).

Altman, R. B.; Terry, D. S.; Zhou, Z.; Zheng, Q.; Geggier, P.; Kolster, R. A.; Zhao, Y.; Javitch, J. A.; Warren, J. D.; Blanchard, S. C. (2012). “Cyanine fluorophore derivatives with enhanced photostability.” *Nature Methods* **9** (1), pp. 68–71. DOI: `10.1038/nmeth.1774` (cit. on p. 70).

Andersson, S. (Nov. 2008). “Localization of a fluorescent source without numerical fitting.” *Optics Express* **16** (23), pp. 18714–18724. DOI: `10.1364/OE.16.018714` (cit. on p. 10).

Appelhans, T.; Richter, C. P.; Wilkens, V.; Hess, S. T.; Piehler, J.; Busch, K. B. (2011). “Nanoscale Organization of Mitochondrial Microcompartments Revealed by Combining Tracking and Localization Microscopy.” *Nano Lett.* **12** (2), pp. 610–616. DOI: `10.1021/nl203343a` (cit. on p. 67).

Arhel, N.; Genovesio, A.; Kim, K.-A.; Miko, S.; Perret, E.; Olivo-Marin, J.-C.; Shorte, S.; Charneau, P. (Oct. 2006). “Quantitative four-dimensional tracking of cytoplasmic and nuclear HIV-1 complexes.” *Nature Methods* **3** (10), pp. 817–824. DOI: `10.1038/nmeth928` (cit. on p. 11).

Babcock, H. W. (Oct. 1953). “The Possibility of Compensating Astronomical Seeing.” *Publications of the Astronomical Society of the Pacific* **65** (), p. 229. DOI: `DOI:10.1086/126606` (cit. on p. 23).

Badieirostami, M.; Lew, M. D.; Thompson, M. A.; Moerner, W. E. (Oct. 2010). "Three-dimensional localization precision of the double-helix point spread function versus astigmatism and biplane." *Applied Physics Letters* **97** (16), p. 161103. doi: `10.1063/1.3499652` (cit. on pp. 12, 14).

Barak, L. S.; Webb, W. W. (Dec. 1982). "Diffusion of Low Density Lipoprotein-Receptor Complex on Human Fibroblasts." *The Journal of Cell Biology* **95** (3), pp. 846–852. doi: `10.1083/jcb.95.3.846` (cit. on p. 17).

Berg, H. C. (June 1971). "How to Track Bacteria." *Review of Scientific Instruments* **42** (6), pp. 868–871. doi: `doi:10.1063/1.1685246` (cit. on p. 18).

Berglund, A.; Mabuchi, H. (Oct. 2005). "Tracking-FCS: Fluorescence correlation spectroscopy of individual particles." *Optics Express* **13** (20), pp. 8069–8082. doi: `10.1364/OPEX.13.008069` (cit. on p. 68).

Betzig, E.; Patterson, G. H.; Sougrat, R.; Lindwasser, O. W.; Olenych, S.; Bonifacino, J. S.; Davidson, M. W.; Lippincott-Schwartz, J.; Hess, H. F. (Sept. 2006). "Imaging Intracellular Fluorescent Proteins at Nanometer Resolution." *Science* **313** (5793), pp. 1642–1645. doi: `10.1126/science.1127344` (cit. on p. 15).

Bewersdorf, J.; Pick, R.; Hell, S. W. (May 1998). "Multifocal multiphoton microscopy." *Optics Letters* **23** (9), pp. 655–657. doi: `10.1364/OL.23.000655` (cit. on p. 67).

Bizzarri, R.; Serresi, M.; Luin, S.; Beltram, F. (2009). "Green fluorescent protein based pH indicators for in vivo use: a review." *Analytical and Bioanalytical Chemistry* **393** (4), pp. 1107–1122. doi: `10.1007/s00216-008-2515-9` (cit. on p. 68).

Blum, M.; Büeler, M.; Gratzel, C.; Aschwanden, M. (2011). "Compact optical design solutions using focus tunable lenses." *Proceedings of the SPIE*. **8167**, doi: `10.1117/12.897608` (cit. on p. 36).

Blume, P. A. (Mar. 2007). *The LabVIEW Style Book*. 1st ed. Prentice Hall (cit. on p. 72).

Booth, M. J. (Dec. 2007). "Adaptive Optics in Microscopy." *Philosophical Transactions of the Royal Society A: Mathematical, Physical and Engineering Sciences* **365** (1861), pp. 2829–2843. doi: `10.1098/rsta.2007.0013` (cit. on p. 23).

Born, M.; Wolf, E. (Oct. 1999). *Principles of Optics: Electromagnetic Theory of Propagation, Interference and Diffraction of Light*. 7th ed. Cambridge University Press (cit. on pp. 8, 28, 47).

Bornfleth, H.; Edelmann, P.; Zink, D.; Cremer, T.; Cremer, C. (Nov. 1999). "Quantitative motion analysis of subchromosomal foci in living cells using four-dimensional microscopy." *Biophysical Journal* **77** (5). PMID: 10545385 PMCID: PMC1300559, pp. 2871–2886 (cit. on p. 11).

Botcherby, E.; Juškaitis, R.; Booth, M.; Wilson, T. (Feb. 2008). “An optical technique for remote focusing in microscopy.” *Optics Communications* **281** (4), pp. 880–887. DOI: `10.1016/j.optcom.2007.10.007` (cit. on pp. 28, 36).

Brandenburg, B.; Zhuang, X. (Mar. 2007). “Virus trafficking – learning from single-virus tracking.” *Nature Reviews Microbiology* **5** (3), pp. 197–208. DOI: `10.1038/nrmicro1615` (cit. on p. 4).

Brennan, T. J.; Rhoadarmer, T. A. (2006). “Performance of a woofer-tweeter deformable mirror control architecture for high-bandwidth high-spatial resolution adaptive optics.” **6306**. SPIE, DOI: `10.1117/12.682482` (cit. on p. 68).

Buffington, A.; Crawford, F. S.; Muller, R. A.; Orth, C. D. (Mar. 1977). “First observatory results with an image-sharpening telescope.” *Journal of the Optical Society of America* **67** (3), pp. 304–305. DOI: `10.1364/JOSA.67.000304` (cit. on p. 23).

Cang, H.; Shan Xu, C.; Yang, H. (May 2008). “Progress in single-molecule tracking spectroscopy.” *Chemical Physics Letters* **457** (4–6), pp. 285–291. DOI: `10.1016/j.cplett.2008.03.098` (cit. on pp. 4, 20).

Cang, H.; Wong, C. M.; Xu, C. S.; Rizvi, A. H.; Yang, H. (June 2006). “Confocal three dimensional tracking of a single nanoparticle with concurrent spectroscopic readouts.” *Applied Physics Letters* **88** (22), DOI: `doi:10.1063/1.2204652` (cit. on p. 19).

Cang, H.; Xu, C. S.; Montiel, D.; Yang, H. (2007). “Guiding a confocal microscope by single fluorescent nanoparticles.” *Optics Letters* **32** (18), pp. 2729–2731. DOI: `10.1364/OL.32.002729` (cit. on pp. 19, 39).

Carter, B. C.; Shubeita, G. T.; Gross, S. P. (Mar. 2005). “Tracking single particles: a user-friendly quantitative evaluation.” *Physical Biology* **2** (1), pp. 60–72. DOI: `10.1088/1478-3967/2/1/008` (cit. on p. 10).

Chao, J.; Ram, S.; Abraham, A. V.; Sally Ward, E.; Ober, R. J. (May 2009). “A resolution measure for three-dimensional microscopy.” *Optics Communications* **282** (9), pp. 1751–1761. DOI: `10.1016/j.optcom.2009.01.062` (cit. on p. 11).

Cheezum, M. K.; Walker, W. F.; Guilford, W. H. (Oct. 2001). “Quantitative Comparison of Algorithms for Tracking Single Fluorescent Particles.” *Biophysical Journal* **81** (4), pp. 2378–2388. DOI: `10.1016/S0006-3495(01)75884-5` (cit. on p. 10).

Cox, S.; Rosten, E.; Monypenny, J.; Jovanovic-Talisman, T.; Burnette, D. T.; Lippincott-Schwartz, J.; Jones, G. E.; Heintzmann, R. (Dec. 2011). “Bayesian localization microscopy reveals nanoscale podosome dynamics.” *Nature Methods* **9** (2), pp. 195–200. DOI: `10.1038/nmeth.1812` (cit. on p. 15).

Croft, W. J. (Sept. 2006). *Under the Microscope: A Brief History of Microscopy*. World Scientific Publishing Company (cit. on p. 1).

Davies, R.; Kasper, M. (2012). "Adaptive Optics for Astronomy." *Annual Review of Astronomy and Astrophysics* **50** (1), null. DOI: `10.1146/annurev-astro-081811-125447` (cit. on p. 23).

Débarre, D.; Vieille, T.; Beaurepaire, E. (2011). "Simple characterisation of a deformable mirror inside a high numerical aperture microscope using phase diversity." *Journal of Microscopy* **244** (2), 136–143. DOI: `10.1111/j.1365-2818.2011.03518.x` (cit. on p. 29).

Dupont, A.; Lamb, D. C. (2011). "Nanoscale three-dimensional single particle tracking." *Nanoscale* **3** (11), p. 4532. DOI: `10.1039/c1nr10989h` (cit. on pp. 4, 18, 39).

Einstein, A. (1905). "Über die von der molekularkinetischen Theorie der Wärme geforderte Bewegung von in ruhenden Flüssigkeiten suspendierten Teilchen." *Annalen der Physik* **322** (8), 549–560. DOI: `10.1002/andp.19053220806` (cit. on p. 21).

Enderlein, J. (2000). "Tracking of fluorescent molecules diffusing within membranes." *Applied Physics B: Lasers and Optics* **71** (5), pp. 773–777. DOI: `10.1007/s003400000409` (cit. on p. 19).

Escuti, M. J.; Jones, W. M. (Aug. 2006). "A polarization-independent liquid crystal spatial light modulator." (), pp. 63320M–63320M. DOI: `10.1117/12.681213` (cit. on p. 67).

Fernández-Suárez, M.; Ting, A. Y. (Nov. 2008). "Fluorescent probes for super-resolution imaging in living cells." *Nature Reviews Molecular Cell Biology* **9** (12), pp. 929–943. DOI: `10.1038/nrm2531` (cit. on p. 67).

Fölling, J.; Bossi, M.; Bock, H.; Medda, R.; Wurm, C. A.; Hein, B.; Jakobs, S.; Eggeling, C.; Hell, S. W. (Sept. 2008). "Fluorescence nanoscopy by ground-state depletion and single-molecule return." *Nature Methods* **5** (11), pp. 943–945. DOI: `10.1038/nmeth.1257` (cit. on p. 15).

Fujiwara, T.; Ritchie, K.; Murakoshi, H.; Jacobson, K.; Kusumi, A. (June 2002). "Phospholipids Undergo Hop Diffusion in Compartmentalized Cell Membrane." *The Journal of Cell Biology* **157** (6), pp. 1071–1082. DOI: `10.1083/jcb.200202050` (cit. on pp. 3–4).

Gelles, J.; Schnapp, B. J.; Sheetz, M. P. (Feb. 1988). "Tracking kinesin-driven movements with nanometre-scale precision." *Nature* **331** (6155), pp. 450–453. DOI: `10.1038/331450a0` (cit. on p. 17).

Gerchberg, R.; Saxton, O. (1972). “A practical algorithm for the determination of the phase from image and diffraction plane pictures.” *Optik* **35** (), pp. 237–246 (cit. on p. 29).

Goss, J. W.; Toomre, D. K. (June 2008). “Both daughter cells traffic and exocytose membrane at the cleavage furrow during mammalian cytokinesis.” *The Journal of Cell Biology* **181** (7), pp. 1047–1054. DOI: `10.1083/jcb.200712137` (cit. on p. 61).

Gould, T. J.; Burke, D.; Bewersdorf, J.; Booth, M. J. (Sept. 2012). “Adaptive optics enables 3D STED microscopy in aberrating specimens.” *Optics Express* **20** (19), pp. 20998–21009. DOI: `10.1364/OE.20.020998` (cit. on p. 27).

Goulian, M.; Simon, S. M. (Oct. 2000). “Tracking Single Proteins within Cells.” *Biophysical Journal* **79** (4), pp. 2188–2198. DOI: `10.1016/S0006-3495(00)76467-8` (cit. on p. 4).

Gustafsson; Agard; Sedat (1999). “I5M: 3D widefield light microscopy with better than 100 nm axial resolution.” *Journal of Microscopy* **195** (1), 10–16. DOI: `10.1046/j.1365-2818.1999.00576.x` (cit. on p. 13).

Ha, T.; Tinnefeld, P. (2012). “Photophysics of Fluorescent Probes for Single-Molecule Biophysics and Super-Resolution Imaging.” *Annual Review of Physical Chemistry* **63** (1), pp. 595–617. DOI: `10.1146/annurev-physchem-032210-103340` (cit. on pp. 69–70).

Hagglund, T. (Jan. 1995). *PID Controllers: Theory, Design, and Tuning*. 2nd ed. ISA: The Instrumentation, Systems, and Automation Society (cit. on p. 44).

Haken, H.; Wolf, H. C. (Mar. 2006). *Molekülphysik und Quantenchemie: Einführung in die experimentellen und theoretischen Grundlagen*. 5th ed. Springer (cit. on p. 69).

Hanser, B. M.; Gustafsson, M. G. L.; Agard, D. A.; Sedat, J. W. (Sept. 2004). “Phase-retrieved pupil functions in wide-field fluorescence microscopy.” *Journal of Microscopy* **216** (1), pp. 32–48. DOI: `10.1111/j.0022-2720.2004.01393.x` (cit. on p. 29).

Hanser, B. M.; Gustafsson, M. G. L.; Agard, D. A.; Sedat, J. W. (May 2003). “Phase retrieval for high-numerical-aperture optical systems.” *Optics Letters* **28** (10). PMID: 12779151, pp. 801–803 (cit. on p. 29).

Haynes, W. M., ed. (June 2012). *CRC Handbook of Chemistry and Physics, 93rd Edition*. 93rd ed. CRC Press (cit. on p. 56).

Hecht, E. (Aug. 2001). *Optics*. 4th ed. Addison Wesley (cit. on p. 10).

Heilemann, M.; Linde, S. van de; Schüttpelz, M.; Kasper, R.; Seefeldt, B.; Mukherjee, A.; Tinnefeld, P.; Sauer, M. (July 2008). “Subdiffraction-Resolution Fluorescence

Imaging with Conventional Fluorescent Probes." *Angewandte Chemie International Edition* **47** (33), pp. 6172–6176. DOI: `10.1002/anie.200802376` (cit. on p. 15).

Hell, S. W. (May 2007). "Far-Field Optical Nanoscopy." *Science* **316** (), pp. 1153–1158 (cit. on p. 2).

Hell, S. W.; Wichmann, J. (June 1994). "Breaking the diffraction resolution limit by stimulated emission: stimulated-emission-depletion fluorescence microscopy." *Optics Letters* **19** (11), pp. 780–782. DOI: `10.1364/OL.19.000780` (cit. on p. 29).

Hell, S.; Stelzer, E. H. K. (Dec. 1992). "Properties of a 4Pi confocal fluorescence microscope." *Journal of the Optical Society of America A* **9** (12), pp. 2159–2166. DOI: `10.1364/JOSAA.9.002159` (cit. on p. 13).

Hess, S. T.; Girirajan, T. P.; Mason, M. D. (Dec. 2006). "Ultra-High Resolution Imaging by Fluorescence Photoactivation Localization Microscopy." *Biophysical Journal* **91** (11), pp. 4258–4272. DOI: `10.1529/biophysj.106.091116` (cit. on p. 15).

Hess, S. T.; Gould, T. J.; Gudheti, M. V.; Maas, S. A.; Mills, K. D.; Zimmerberg, J. (Oct. 2007). "Dynamic Clustered Distribution of Hemagglutinin Resolved at 40 Nm in Living Cell Membranes Discriminates Between Raft Theories." *Proceedings of the National Academy of Sciences* **104** (44), pp. 17370–17375. DOI: `10.1073/pnas.0708066104` (cit. on p. 67).

Högbom, J. A. (June 1974). "Aperture Synthesis with a Non-Regular Distribution of Interferometer Baselines." *Astronomy and Astrophysics Supplement Series* **15** (), p. 417 (cit. on p. 15).

Holtzer, L.; Meckel, T.; Schmidt, T. (Feb. 2007). "Nanometric three-dimensional tracking of individual quantum dots in cells." *Applied Physics Letters* **90** (5), DOI: `doi:10.1063/1.2437066` (cit. on pp. 11, 18).

Hooke, R. (Sept. 1665). *Micrographia. Some Physiological Descriptions of Minute Bodies Made by Magnifying Glasses with Observations and Inquiries Thereupon*. 1st ed. London, UK: \ (cit. on p. 1).

Hopkins, C. R.; Trowbridge, I. S. (Aug. 1983). "Internalization and processing of transferrin and the transferrin receptor in human carcinoma A431 cells." *The Journal of Cell Biology* **97** (2), pp. 508–521. DOI: `10.1083/jcb.97.2.508` (cit. on p. 61).

Howard, J. (Feb. 2001). *Mechanics of Motor Proteins and the Cytoskeleton*. 1st ed. Sinauer Associates (cit. on pp. 53, 61).

Huang, B.; Wang, W.; Bates, M.; Zhuang, X. (Feb. 2008). "Three-Dimensional Super-Resolution Imaging by Stochastic Optical Reconstruction Microscopy." *Science* **319** (5864), pp. 810–813. DOI: `10.1126/science.1153529` (cit. on pp. 11–12).

Huang, F.; Schwartz, S. L.; Byars, J. M.; Lidke, K. A. (May 2011). “Simultaneous multiple-emitter fitting for single molecule super-resolution imaging.” *Biomedical Optics Express* **2** (5), pp. 1377–1393. DOI: `10.1364/BOE.2.001377` (cit. on p. 15).

Huang, Z.-L.; Zhu, H.; Long, F.; Ma, H.; Qin, L.; Liu, Y.; Ding, J.; Zhang, Z.; Luo, Q.; Zeng, S. (Sept. 2011). “Localization-based super-resolution microscopy with an sCMOS camera.” *Optics Express* **19** (20), pp. 19156–19168. DOI: `10.1364/OE.19.019156` (cit. on p. 68).

Huber, M. L.; Perkins, R. A.; Laesecke, A.; Friend, D. G.; Sengers, J. V.; Assael, M. J.; Metaxa, I. N.; Vogel, E.; Mareš, R.; Miyagawa, K. (Apr. 2009). “New International Formulation for the Viscosity of H2O.” *Journal of Physical and Chemical Reference Data* **38** (2), pp. 101–125. DOI: `doi:10.1063/1.3088050` (cit. on p. 2).

Jin, M.; Snider, M. D. (Aug. 1993). “Role of microtubules in transferrin receptor transport from the cell surface to endosomes and the Golgi complex.” *Journal of Biological Chemistry* **268** (24), pp. 18390–18397 (cit. on p. 61).

Jones, S. A.; Shim, S.-H.; He, J.; Zhuang, X. (May 2011). “Fast, three-dimensional super-resolution imaging of live cells.” *Nature Methods* **8** (6), pp. 499–505. DOI: `10.1038/nmeth.1605` (cit. on p. 2).

Juette, M. F. (Apr. 2009). *3D Fluorescence Photoactivation Localization Microscopy and Particle Tracking with Biplane Detection*. University of Heidelberg: Diplom thesis in physics (cit. on pp. 5, 13, 38, 45–46).

Juette, M. F.; Bewersdorf, J. (Oct. 2010). “Three-Dimensional Tracking of Single Fluorescent Particles with Submillisecond Temporal Resolution.” *Nano Lett.* **10** (11), pp. 4657–4663. DOI: `10.1021/nl1028792` (cit. on pp. 5, 41, 51, 54–55).

Juette, M. F.; Gould, T. J.; Lessard, M. D.; Mlodzianoski, M. J.; Nagpure, B. S.; Bennett, B. T.; Hess, S. T.; Bewersdorf, J. (May 2008). “Three-dimensional sub–100 nm resolution fluorescence microscopy of thick samples.” *Nature Methods* **5** (6), pp. 527–529. DOI: `10.1038/nmeth.1211` (cit. on pp. 5, 12–13, 15, 17).

Kao, H.; Verkman, A. (Sept. 1994). “Tracking of single fluorescent particles in three dimensions: use of cylindrical optics to encode particle position.” *Biophysical Journal* **67** (3), pp. 1291–1300. DOI: `10.1016/S0006-3495(94)80601-0` (cit. on pp. 11, 18).

Katayama, Y.; Burkacky, O.; Meyer, M.; Bräuchle, C.; Gratton, E.; Lamb, D. C. (Sept. 2009). “Real-Time Nanomicroscopy via Three-Dimensional Single-Particle Tracking.” *ChemPhysChem* **10** (14), pp. 2458–2464. DOI: `10.1002/cphc.200900436` (cit. on pp. 19–20, 39).

Kirkby, P. A.; Srinivas Nadella, K. M. N.; Silver, R. A. (June 2010). “A compact acousto-optic lens for 2D and 3D femtosecond based 2-photon microscopy.” *Optics Express* **18** (13), pp. 13720–13744. doi: `10.1364/OE.18.013720` (cit. on p. 35).

Kner, P.; Chhun, B. B.; Griffis, E. R.; Winoto, L.; Gustafsson, M. G. L. (2009). “Super-resolution video microscopy of live cells by structured illumination.” *Nature Methods* **6** (5), pp. 339–342. doi: `10.1038/nmeth.1324` (cit. on p. 2).

Kromann, E. B.; Gould, T. J.; Juette, M. F.; Wilhjelm, J. E.; Bewersdorf, J. (June 2012). “Quantitative pupil analysis in stimulated emission depletion microscopy using phase retrieval.” *Optics Letters* **37** (11), pp. 1805–1807. doi: `10.1364/OL.37.001805` (cit. on pp. 29–30).

Lakowicz, J. R. (Sept. 2006). *Principles of Fluorescence Spectroscopy*. 3rd ed. Springer (cit. on pp. 4, 68).

Lange, S.; Katayama, Y.; Schmid, M.; Burkacky, O.; Bräuchle, C.; Lamb, D. C.; Jansen, R.-P. (2008). “Simultaneous Transport of Different Localized mRNA Species Revealed by Live-Cell Imaging.” *Traffic* **9** (8), 1256–1267. doi: `10.1111/j.1600-0854.2008.00763.x` (cit. on p. 4).

Lechleiter, J. D.; Lin, D.-T.; Sieneart, I. (Oct. 2002). “Multi-Photon Laser Scanning Microscopy Using an Acoustic Optical Deflector.” *Biophysical Journal* **83** (4), pp. 2292–2299. doi: `10.1016/S0006-3495(02)73989-1` (cit. on p. 35).

Lehmann, M. J.; Sherer, N. M.; Marks, C. B.; Pypaert, M.; Mothes, W. (July 2005). “Actin- and myosin-driven movement of viruses along filopodia precedes their entry into cells.” *The Journal of Cell Biology* **170** (2), pp. 317–325. doi: `10.1083/jcb.200503059` (cit. on p. 58).

Lessard, G. A.; Goodwin, P. M.; Werner, J. H. (Nov. 2007). “Three-dimensional tracking of individual quantum dots.” *Applied Physics Letters* **91** (22), doi: `doi:10.1063/1.2819074` (cit. on pp. 19, 39).

Levi, V.; Ruan, Q.; Gratton, E. (Apr. 2005). “3-D Particle Tracking in a Two-Photon Microscope: Application to the Study of Molecular Dynamics in Cells.” *Biophysical Journal* **88** (4), pp. 2919–2928. doi: `10.1529/biophysj.104.044230` (cit. on pp. 19, 39).

Levi, V.; Ruan, Q.; Kis-Petikova, K.; Gratton, E. (Oct. 2003). “Scanning FCS, a novel method for three-dimensional particle tracking.” *Biochemical Society Transactions.* **31**, pp. 997–1000 (cit. on p. 68).

Li, C. H.; Bai, L.; Li, D. D.; Xia, S.; Xu, T. (Dec. 2004). “Dynamic tracking and mobility analysis of single GLUT4 storage vesicle in live 3T3-L1 cells.” *Cell Research* **14** (6), pp. 480–486. doi: `10.1038/sj.cr.7290251` (cit. on p. 4).

Linde, S. van de; Krstić, I.; Prisner, T.; Doose, S.; Heilemann, M.; Sauer, M. (2011). “Photoinduced formation of reversible dye radicals and their impact on super-resolution imaging.” *Photochemical & Photobiological Sciences* **10** (4), p. 499. DOI: `10.1039/c0pp00317d` (cit. on pp. 15, 69–70).

Manley, S.; Gillette, J. M.; Patterson, G. H.; Shroff, H.; Hess, H. F.; Betzig, E.; Lippincott-Schwartz, J. (Jan. 2008). “High-density mapping of single-molecule trajectories with photoactivated localization microscopy.” *Nature Methods* **5** (2), pp. 155–157. DOI: `10.1038/nmeth.1176` (cit. on p. 67).

McHale, K.; Berglund, A. J.; Mabuchi, H. (2007). “Quantum Dot Photon Statistics Measured by Three-Dimensional Particle Tracking.” *Nano Lett.* **7** (11), pp. 3535–3539. DOI: `10.1021/nl0723376` (cit. on pp. 20, 39).

Michalet, X. (Oct. 2010). “Mean square displacement analysis of single-particle trajectories with localization error: Brownian motion in an isotropic medium.” *Physical Review E* **82** (4), p. 041914. DOI: `10.1103/PhysRevE.82.041914` (cit. on p. 22).

Mlodzianoski, M. J.; Juette, M. F.; Beane, G. L.; Bewersdorf, J. (May 2009). “Experimental characterization of 3D localization techniques for particle-tracking and super-resolution microscopy.” *Optics Express* **17** (10), pp. 8264–8277. DOI: `10.1364/OE.17.008264` (cit. on pp. 5, 13–14, 18, 39, 49).

Mlodzianoski, M. J.; Schreiner, J. M.; Callahan, S. P.; Smolkov? K.; Dlaskov? A.; ?antorov? J.; Je?ek, P.; Bewersdorf, J. (2011). “Sample drift correction in 3D fluorescence photoactivation localization microscopy.” *Optics Express* **19** (16), pp. 15009–15019. DOI: `10.1364/OE.19.015009` (cit. on pp. 15, 17).

Mothes, W.; Sherer, N. M.; Jin, J.; Zhong, P. (Sept. 2010). “Virus Cell-to-Cell Transmission.” *Journal of Virology* **84** (17), pp. 8360–8368. DOI: `10.1128/JVI.00443-10` (cit. on p. 58).

Murase, K.; Fujiwara, T.; Umemura, Y.; Suzuki, K.; Iino, R.; Yamashita, H.; Saito, M.; Murakoshi, H.; Ritchie, K.; Kusumi, A. (June 2004). “Ultrafine Membrane Compartments for Molecular Diffusion as Revealed by Single Molecule Techniques.” *Biophysical Journal* **86** (6), pp. 4075–4093. DOI: `10.1529/biophysj.103.035717` (cit. on p. 3).

Noll, R. J. (Mar. 1976). “Zernike polynomials and atmospheric turbulence.” *Journal of the Optical Society of America* **66** (3), pp. 207–211. DOI: `10.1364/JOSA.66.000207` (cit. on p. 24).

Ober, R. J.; Ram, S.; Ward, E. S. (Feb. 2004). “Localization Accuracy in Single-Molecule Microscopy.” *Biophysical Journal* **86** (2), pp. 1185–1200. DOI: `10.1016/S0006-3495(04)74193-4` (cit. on p. 11).

Parthasarathy, R. (2012). “Rapid, accurate particle tracking by calculation of radial symmetry centers.” *Nature Methods* (). doi: `10.1038/nmeth.2071` (cit. on p. 10).

Pavani, S. R. P.; Piestun, R. (Dec. 2008). “Three dimensional tracking of fluorescent microparticles using a photon-limited double-helix response system.” *Optics Express* **16** (26), pp. 22048–22057. doi: `10.1364/OE.16.022048` (cit. on p. 11).

Pavani, S. R. P.; Thompson, M. A.; Biteen, J. S.; Lord, S. J.; Liu, N.; Twieg, R. J.; Piestun, R.; Moerner, W. E. (Mar. 2009). “Three-Dimensional, Single-Molecule Fluorescence Imaging Beyond the Diffraction Limit by Using a Double-Helix Point Spread Function.” *Proceedings of the National Academy of Sciences* **106** (9), pp. 2995–2999. doi: `10.1073/pnas.0900245106` (cit. on pp. 11–12).

Pawley, J., ed. (June 2006). *Handbook of Biological Confocal Microscopy*. 3rd ed. Springer (cit. on pp. 4, 35, 39, 50).

Peters, I. M.; Grooth, B. G. de; Schins, J. M.; Figdor, C. G.; Greve, J. (July 1998). “Three dimensional single-particle tracking with nanometer resolution.” *Review of Scientific Instruments* **69** (7), pp. 2762–2766. doi: `doi:10.1063/1.1149012` (cit. on p. 19).

Prabhat, P.; Ram, S.; Ward, E.; Ober, R. (Dec. 2004). “Simultaneous imaging of different focal planes in fluorescence microscopy for the study of cellular dynamics in three dimensions.” *NanoBioscience, IEEE Transactions on* **3** (4), pp. 237–242. doi: `10.1109/TNB.2004.837899` (cit. on pp. 12, 18).

Press, W. H.; Teukolsky, S. A.; Vetterling, W. T.; Flannery, B. P. (Sept. 2007). *Numerical Recipes: The Art of Scientific Computing*. 3rd ed. Cambridge University Press (cit. on p. 46).

Ram, S.; Prabhat, P.; Chao, J.; Sally Ward, E.; Ober, R. J. (Dec. 2008). “High Accuracy 3D Quantum Dot Tracking with Multifocal Plane Microscopy for the Study of Fast Intracellular Dynamics in Live Cells.” *Biophysical Journal* **95** (12), pp. 6025–6043. doi: `10.1529/biophysj.108.140392` (cit. on p. 18).

Richards, B.; Wolf, E. (Dec. 1959). “Electromagnetic Diffraction in Optical Systems. II. Structure of the Image Field in an Aplanatic System.” *Proceedings of the Royal Society of London. Series A. Mathematical and Physical Sciences* **253** (1274), pp. 358–379. doi: `10.1098/rspa.1959.0200` (cit. on pp. 9–10).

Riley, M. E.; Gusinow, M. A. (Oct. 1977). “Laser beam divergence utilizing a lateral shearing interferometer.” *Applied Optics* **16** (10), pp. 2753–2756. doi: `10.1364/AO.16.002753` (cit. on p. 49).

Roorda, A. (June 2011). “Adaptive optics for studying visual function: A comprehensive review.” *Journal of Vision* **11** (5). doi: `10.1167/11.5.6` (cit. on p. 23).

Roy, R.; Hohng, S.; Ha, T. (June 2008). “A practical guide to single-molecule FRET.” *Nature Methods* **5** (6), pp. 507–516. DOI: `10.1038/nmeth.1208` (cit. on p. 68).

Rust, M. J.; Bates, M.; Zhuang, X. (Aug. 2006). “Sub-diffraction-limit imaging by stochastic optical reconstruction microscopy (STORM).” *Nature Methods* **3** (10), pp. 793–796. DOI: `10.1038/nmeth929` (cit. on p. 15).

Salomé, R.; Kremer, Y.; Dieudonné, S.; Léger, J.-F.; Krichevsky, O.; Wyart, C.; Chatenay, D.; Bourdieu, L. (June 2006). “Ultrafast random-access scanning in two-photon microscopy using acousto-optic deflectors.” *Journal of Neuroscience Methods* **154** (1–2), pp. 161–174. DOI: `10.1016/j.jneumeth.2005.12.010` (cit. on p. 35).

Saxton, M. J.; Jacobson, K. (1997). “Single-Particle Tracking: Applications to Membrane Dynamics.” *Annual Review of Biophysics and Biomolecular Structure* **26** (1), pp. 373–399. DOI: `10.1146/annurev.biophys.26.1.373` (cit. on pp. 2, 10, 17, 20).

Saxton, M. (Aug. 1995). “Single-particle tracking: effects of corrals.” *Biophysical Journal* **69** (2), pp. 389–398. DOI: `10.1016/S0006-3495(95)79911-8` (cit. on p. 22).

Schmidt, T.; Schütz, G. J.; Baumgartner, W.; Gruber, H. J.; Schindler, H. (Apr. 1996). “Imaging of Single Molecule Diffusion.” *Proceedings of the National Academy of Sciences* **93** (7), pp. 2926–2929 (cit. on p. 4).

Shack, R. V. (1971). “Production and use of a lenticular Hartmann screen.” *Journal of the Optical Society of America* **61** (), p. 656 (cit. on p. 26).

Shim, S.-H.; Xia, C.; Zhong, G.; Babcock, H. P.; Vaughan, J. C.; Huang, B.; Wang, X.; Xu, C.; Bi, G.-Q.; Zhuang, X. (Aug. 2012). “Super-resolution fluorescence imaging of organelles in live cells with photoswitchable membrane probes.” *Proceedings of the National Academy of Sciences* **109** (35), pp. 13978–13983. DOI: `10.1073/pnas.1201882109` (cit. on p. 2).

Shtengel, G.; Galbraith, J. A.; Galbraith, C. G.; Lippincott-Schwartz, J.; Gillette, J. M.; Manley, S.; Sougrat, R.; Waterman, C. M.; Kanchanawong, P.; Davidson, M. W.; Fetter, R. D.; Hess, H. F. (Mar. 2009). “Interferometric Fluorescent Super-Resolution Microscopy Resolves 3D Cellular Ultrastructure.” *Proceedings of the National Academy of Sciences* **106** (9), pp. 3125–3130. DOI: `10.1073/pnas.0813131106` (cit. on p. 13).

Silverman, R. H.; Nguyen, C.; Weight, C. J.; Klein, E. A. (July 2010). “The human retrovirus XMRV in prostate cancer and chronic fatigue syndrome.” *Nature Reviews Urology* **7** (7), pp. 392–402. DOI: `10.1038/nrurol.2010.77` (cit. on p. 58).

Smith, C. S.; Joseph, N.; Rieger, B.; Lidke, K. A. (Apr. 2010). “Fast, single-molecule localization that achieves theoretically minimum uncertainty.” *Nature Methods* **7** (5), pp. 373–375. DOI: `10.1038/nmeth.1449` (cit. on p. 10).

Southwell, W. H. (1980). “Wave-front estimation from wave-front slope measurements.” *Journal of the Optical Society of America* **70** (8), pp. 998–1006. doi: `10.1364/JOSA.70.000998` (cit. on p. 26).

Speidel, M.; Jonas, A.; Florin, E.-L. (Jan. 2003). “Three-dimensional tracking of fluorescent nanoparticles with subnanometer precision by use of off-focus imaging.” *Optics Letters* **28** (2), pp. 69–71. doi: `10.1364/OL.28.000069` (cit. on p. 11).

Thompson, M. A.; Lew, M. D.; Badieirostami, M.; Moerner, W. E. (2009). “Localizing and Tracking Single Nanoscale Emitters in Three Dimensions with High Spatiotemporal Resolution Using a Double-Helix Point Spread Function.” *Nano Lett.* **10** (1), pp. 211–218. doi: `10.1021/nl903295p` (cit. on pp. 11, 18).

Thompson, R. E.; Larson, D. R.; Webb, W. W. (May 2002). “Precise Nanometer Localization Analysis for Individual Fluorescent Probes.” *Biophysical Journal* **82** (5), pp. 2775–2783. doi: `10.1016/S0006-3495(02)75618-X` (cit. on pp. 10, 40).

Toomre, D. K.; Bewersdorf, J. (2010). “A New Wave of Cellular Imaging.” *Annual Review of Cell and Developmental Biology* **26** (1), pp. 285–314. doi: `10.1146/annurev-cellbio-100109-104048` (cit. on p. 2).

Toprak, E.; Balci, H.; Blehm, B. H.; Selvin, P. R. (2007). “Three-Dimensional Particle Tracking via Bifocal Imaging.” *Nano Lett.* **7** (7), pp. 2043–2045. doi: `10.1021/nl0709120` (cit. on pp. 12, 18).

Vdovin, G. V. (Sept. 1998). “Optimization-based operation of micromachined deformable mirrors.” *Proceedings of SPIE* **3353** (1), pp. 902–909. doi: `doi:10.1117/12.321669` (cit. on pp. 38, 46).

Vdovin, G.; Middelhoek, S.; Sarro, P. M. (May 1997). “Technology and applications of micromachined silicon adaptive mirrors.” *Optical Engineering* **36** (5), pp. 1382–1390. doi: `doi:10.1117/1.601334` (cit. on p. 27).

Vetrone, F.; Naccache, R.; Zamarrón, A.; Juarranz de la Fuente, A.; Sanz-Rodríguez, F.; Martinez Maestro, L.; Martín Rodriguez, E.; Jaque, D.; García Solé, J.; Capobianco, J. A. (June 2010). “Temperature Sensing Using Fluorescent Nanothermometers.” *ACS Nano* **4** (6), pp. 3254–3258. doi: `10.1021/nn100244a` (cit. on p. 68).

Wells, N. P.; Lessard, G. A.; Goodwin, P. M.; Phipps, M. E.; Cutler, P. J.; Lidke, D. S.; Wilson, B. S.; Werner, J. H. (2010). “Time-Resolved Three-Dimensional Molecular Tracking in Live Cells.” *Nano Lett.* **10** (11), pp. 4732–4737. doi: `10.1021/nl103247v` (cit. on p. 68).

Westphal, V.; Rizzoli, S. O.; Lauterbach, M. A.; Kamin, D.; Jahn, R.; Hell, S. W. (Apr. 2008). “Video-Rate Far-Field Optical Nanoscopy Dissects Synaptic Vesicle

Movement." *Science* **320** (5873), pp. 246–249. DOI: `10.1126/science.1154228` (cit. on p. 2).

Wright, A. J.; Burns, D.; Patterson, B. A.; Poland, S. P.; Valentine, G. J.; Girkin, J. M. (May 2005). "Exploration of the optimisation algorithms used in the implementation of adaptive optics in confocal and multiphoton microscopy." *Microscopy Research and Technique* **67** (1), pp. 36–44. DOI: `10.1002/jemt.20178` (cit. on p. 46).

Yildiz, A.; Forkey, J. N.; McKinney, S. A.; Ha, T.; Goldman, Y. E.; Selvin, P. R. (June 2003). "Myosin V Walks Hand-Over-Hand: Single Fluorophore Imaging with 1.5-Nm Localization." *Science* **300** (5628), pp. 2061–2065. DOI: `10.1126/science.1084398` (cit. on pp. 4, 17).

Zernike, v. F. (May 1934). "Beugungstheorie des Schneidenverfahrens und seiner verbesserten Form, der Phasenkontrastmethode." *Physica* **1** (7–12), pp. 689–704. DOI: `10.1016/S0031-8914(34)80259-5` (cit. on p. 24).

Zhu, L.; Zhang, W.; Elnatan, D.; Huang, B. (2012). "Faster STORM using compressed sensing." *Nature Methods* (). DOI: `10.1038/nmeth.1978` (cit. on p. 15).

Zhu, L.; Sun, P.-C.; Bartsch, D.-U.; Freeman, W. R.; Fainman, Y. (Oct. 1999). "Wavefront generation of Zernike polynomial modes with a micromachined membrane deformable mirror." *Applied Optics* **38** (28), pp. 6019–6026. DOI: `10.1364/AO.38.006019` (cit. on pp. 27, 46).

Zhu, L.; Sun, P.-C.; Fainman, Y. (1999). "Aberration-Free Dynamic Focusing with a Multichannel Micromachined Membrane Deformable Mirror." *Applied Optics* **38** (25), pp. 5350–5354. DOI: `10.1364/AO.38.005350` (cit. on pp. 27, 36).

Züchner, T.; Failla, A. V.; Meixner, A. J. (2011). "Light Microscopy with Doughnut Modes: A Concept to Detect, Characterize, and Manipulate Individual Nanoobjects." *Angewandte Chemie International Edition* **50** (23), 5274–5293. DOI: `10.1002/anie.201005845` (cit. on p. 27).